HARVARD
Kenneth C. Griffin

GRADUATE SCHOOL
OF ARTS AND SCIENCES

THESIS ACCEPTANCE CERTIFICATE

The undersigned, appointed by the

Department of Physics

have examined a dissertation entitled

Laser cooling, optical trapping and Zeeman-Sisyphus deceleration of heavy polyatomic molecules for probing physics beyond the Standard Model

presented by Hiromitsu Sawaoka

candidate for the degree of Doctor of Philosophy and hereby certify that it is worthy of acceptance.

Signature John Doyle

Typed name: Prof. John Doyle

Signature

Typed name: Prof. Markus Greiner

Signature

Typed name: Prof. Susanne Yelin

Date: May 14, 2025

Laser cooling, optical trapping and Zeeman-Sisyphus deceleration of heavy polyatomic molecules for probing physics beyond the Standard Model

A DISSERTATION PRESENTED
BY
HIROMITSU SAWAOKA
TO
THE DEPARTMENT OF PHYSICS

IN PARTIAL FULFILLMENT OF THE REQUIREMENTS
FOR THE DEGREE OF
DOCTOR OF PHILOSOPHY
IN THE SUBJECT OF
PHYSICS

HARVARD UNIVERSITY
CAMBRIDGE, MASSACHUSETTS
MAY 2025

Thesis advisor: Professor John M. Doyle		Hiromitsu Sawaoka

Laser cooling, optical trapping and Zeeman-Sisyphus deceleration of heavy polyatomic molecules for probing physics beyond the Standard Model

ABSTRACT

Ultracold polyatomic molecules containing heavy nuclei, such as SrOH and YbOH, are sensitive to T- symmetry violating and P-symmetry violating physics beyond the Standard Model through the electron's electric dipole moment. Furthermore, SrOH is sensitive to ultralight Dark Matter through measuring time variations of fundamental constants. However, in order to make full use of these molecules, they need to be cooled to ultracold temperatures and held in optical traps. We have realized a magneto-optical trap (MOT) of SrOH and used this as the essential element to achieve optical trapping in the microKelvin temperature regime. We observed MOT lifetimes approaching 200 ms with temperatures $\sim$ 1 mK and observed damped oscillations in the MOT. We further cooled the SrOH molecules to $\sim$ 40 μ K using Λ-enhanced gray molasses, and compressed the cloud to about 100 μm size using the conveyor belt MOT technique. Using this ultracold dense cloud of SrOH, we loaded an optical dipole trap (ODT), with a molecular lifetime of 1.2(1) seconds. In separate experiments with YbOH, which is heavier than SrOH, we demonstrated a novel deceleration method (Zeeman-Sisyphus deceleration) that can slow YbOH to under 20 m/s with only a few photons scattered utilizing high magnetic fields up to 2.5 T. By driving spin-flip transitions at the maxima and minima of the magnetic fields, slowing was achieved, which is a critical first step toward loading of a MOT for this species. We addressed the challenges associated with driving spin-flip transitions in molecules that have molecular perturbations among the electronic excited states and developed an understanding of the physics of such systems that is applicable to a wide range of molecules.

Contents

Listing of figures

Listing of tables

Citations to Previous Work

Portions of this thesis or results described herein have previously been published in the references below.

[1] B. L. Augenbraun, A. Frenett, H. Sawaoka, C. Hallas, N. B. Vilas, A. Nasir, Z. D. Lasner, and J. M. Doyle. Zeeman-sisyphus deceleration of molecular beams. *Physical Review Letters*, 127:263002, 2021.

[2] Z. D. Lasner, A. Frenett, H. Sawaoka, L. Anderegg, B. Augenbraun, H. Lampson, M. Li, A. Lunstad, J. Mango, A. Nasir, T. Ono, T. Sakamoto, and J. M. Doyle. Magneto-optical trapping of a heavy polyatomic molecule for precision measurement. *Physical Review Letters*, 134:083401, 2025.

[3] H. Sawaoka, A. Frenett, A. Nasir, T. Ono, B. L. Augenbraun, T. C. Steimle, and J. M. Doyle. Zeeman-sisyphus deceleration for heavy molecules with perturbed excited-state structure. *Physical Review A*, 107:022810, 2023.

To my family.

Acknowledgments

First and foremost, I would like to thank my advisor, John Doyle, for his incredible support over the seven years of my PhD. He provided invaluable guidance in many areas—from shaping scientific goals to teaching me how to build various systems in the lab, such as superconducting magnets. Beyond that, he was a role model in how to communicate science effectively and manage a research group with many diverse stakeholders. His generosity—with excellent coffee, pastries, cheese, and liquor—boosted both morale and productivity over the years.

I also thank my committee members, Markus Greiner and Susanne Yelin, for their unwavering support throughout the program. Markus showed enthusiastic interest in my research, engaging in hour-long conversations during annual check-ins. Susanne provided valuable insight not only into scientific topics but also on navigating academia—such as advice for postdoc interviews—which proved extremely helpful.

I am deeply grateful to those I worked closely with in the lab. Zack Lasner mentored me for most of my time in the group. He taught me the fundamentals of research and was always patient with my wild-sounding ideas—some of which turned out to be essential. He also supported me through a difficult project transition and helped me adjust to working in a larger team environment. Ben Augenbraun was another early mentor who introduced me to both experimental techniques and the theoretical aspects of molecular laser cooling. Though I was too naïve at the time to grasp it all, he laid a foundation that Zack later helped reinforce. From Ben, I also learned how to be a productive graduate student. Alex Frenett and I joined the lab at the same time and accomplished many scientific goals together. I thank him for always being open to listening to my ideas and for including me in our cohort's activities, which helped me feel more connected to the department. Abdullah Nasir quickly picked things up and regularly challenged me to justify my ideas—often leading to better ones. His meticulous approach kept our experiments running safely and smoothly; without him, I likely would have broken far more equipment than I actually did.

After transitioning to the SrOH project, I had the pleasure of working with many more amazing people. Loïc Anderegg taught me how to build and operate nearly every piece of lab equipment and guided me through the intricacies of molecular laser cooling. I also appreciated our regular tennis matches. Annika Lunstad brought a perfect balance of creativity and precision to our experiment. Her optical setups—the most elegant in our lab—were truly impressive. Mingda Li brought energy and enthusiasm to the lab and often surprised me with creative ideas. His determination, especially as we rushed to complete experiments before my graduation, was inspiring. Jack Mango, the most recent graduate student to join the group, has been incredibly fast at picking up new skills. I learned a lot from his expertise in electronics. Takashi Sakamoto, visiting from the University of Tokyo, was a quick learner and productive collaborator, during our work on the buffer gas beam source. I also deeply appreciated his friendship outside of the lab.

I am also grateful to the undergraduate students I worked with—Tasuku Ono, Cal Miller, Zhijing Niu, Hana Lampson, and Rachael Fields—for their excellent work and the energy they brought to the lab.

Next, I would like to thank the rest of the Doyle group, who supported me both scientifically and personally. Yicheng Bao was always kind and generous with his time, teaching me countless technical details and engaging in thoughtful discussions—even late at night. I also appreciated his friendship and our many food outings over the years. Christian Hallas supported me through many ups and downs, both in science and in life. He was always there to listen when I faced challenges in my experiments. And of course, our intense tennis matches were a great source of fun. Nathaniel Vilas, my cohort-mate, has always been a role model to me—both as a scientist and as a friend. I'm thrilled that our paths will continue together at Berkeley!

Many other members of the Doyle group contributed to the wonderful experience I had at Harvard: Louis Baum, Sean Burchesky, Xing Wu, Lawrence Cheuk, Debayan Mitra, Scarlett Yu, Paige Robichaud, Grace Li, Jiaqi You, Giseok Lee, Matteo Fulghieri, Shungo Fukaya, Avikar Periwal, Junheng Tao, Sepehr Ebadi, Arian Jadbabaie, Ayami Hiramoto, and many visiting and undergraduate students. Thank you all for the support over the years.

I would also like to thank everyone who made this research possible. Erica Mantone and Erica Colwell handled lab administration with professionalism and patience. Lisa Cacciabaudo, Hannah Belcher, and Jacob Barandes made sure I stayed on track in the graduate program. Adam Ackerman and Silke Exner kept everything running smoothly on the financial side.

I am thankful to Stan Cotreau, Steve Sansone, Andy Dimambro, and Alejandro Lopez for their invaluable guidance in the machine shop, and to Jim MacArthur for his help in the electronics shop. Many thanks also to Joel Day for managing the building infrastructure, Joe Sears for handling all our electrical connections, and Stephen Concannon, Sean Concannon, and Robert Kenney for helping build many critical components of the lab.

I would also like to thank Amar Vutha, my undergraduate advisor and later a collaborator on my graduate research. His insightful teaching sparked my interest in AMO physics and precision measurements, and he taught me how to think deeply and clearly about physics. As one of the founding members of his lab, I had the privilege of learning from him firsthand in both experimental and theoretical contexts. His mentorship was instrumental in my decision to pursue this field. I am also grateful to the Vutha group—especially Mohit Verma—whose discussions and friendship have continued throughout my graduate years.

To all my friends outside the lab who helped me stay grounded during grad school—thank you. In particular, I want to thank Kenneth Wang, whom I first met as a G-zero mentor and who played a major role in my decision to come to Harvard. His kindness helped me through many stressful moments. I also enjoyed countless tennis and chess matches with him. Other friends, including Yuiki Takahashi, Marcin Kalinowski, and Kentaro Komori, made life outside the lab fun and fulfilling. I also thank the communities that welcomed me during these years: the Boston Shogi Club, the Boston Japanese Researchers Forum, and the Donnelly Field pickup frisbee group.

I also want to thank my friends from college and high school, and my high school teachers—especially Mr. Emura—for inspiring my early interest in physics.

I am deeply grateful to my family, who have always loved and supported me: my parents, my brother, my grandparents, and my extended family around the world.

Last but not least, I want to thank Tomoyo, who has brought so much joy and laughter into my life. Thank you for all the love and support you've given me.

0

Introduction

We discuss how ultracold heavy polyatomic molecules can be used for probes to physics beyond the Standard Model, with two examples. First we discuss probing the electron's permeanent electric dipole moment with molecules like SrOH and YbOH. Second we discuss dark matter detection through precision measurement of the proton-to-electron mass ratio, using SrOH. At the end of this chapter, we discuss how such platforms of ultracold molecules can be achieved.

0.1 How to read this thesis

Some of the work described in this thesis (first half of Chapter 2 and all of Chapter 4) has already appeared in other theses, especially in those of Alexander Frenett and Benjamin Augenbraun, who were other graduate students that the author worked together with for a large protion of graduate studies. In such chapters we will focus more on the author's perspectives that were not covered in previous theses. Reading previous theses is recommended to get further understanding. Alexander Frenett and Benjamin Augenbraun both do a great job describing the motivations covered in the Introduction and molecular structure covered in Chapter 1.

Contents of the later half of Cahpter 2 and the entire Chapter 3 do not appear in any previuous theses, so we have tried to include as much information as possible in these chapters.

For more background, reading theses of Zack Lasner (Yale) and Arian Jadbabaie (Caltech), just to name a few, are highly recommended. General moelcular laser cooling information can be found in previous theses in the Doyle group, such as Loïc Anderegg, Yicheng Bao and Nathaniel Vilas, just to name a few.

0.2 Electron's electric dipole moment searches with heavy polyatomic molecules

Although the Standard Model of particle physics has never disagreed with experimental tests, there are still major mysteries surrounding this theory. For example, one of the most significant challenges facing fundamental physics is to explain why the universe is made out of matter and contains no free anti-matter despite an apparent symmetry between these entities. Our universe is dominated by matter and the Standard Model (SM) has no explanation for this simple observational fact[22,27,52]. One well-motivated way to explain this asymmetry is to include new, massive particles in the model which lead to new interactions. One way of experimentally verifying such new particles is directly producing them at particle colliders. Unfortunately, no new particles have been discovered at existing facilities, and the predicted masses in many theories are far beyond the range of conceivable next-generation colliders[8,45,13]. Another way of verifying these "new particles" is through very precise measurements of existing fundamental particles, such as the electron [12,31,47,26,28]. The interactions between the "new particles" and the electron would cause the electron to gain a very small electric dipole moment (EDM)[39,38]. Specifically, EDMs of fundamental particles, such as that of the electron, are sensitive to time-symmetry violating and parity-symmetry violating effects.

An electric dipole moment $\vec{d}$ is a property of a particle defined by the interaction Hamiltonian $H_d = -\vec{d} \cdot \vec{E}$, where $\vec{E}$ is an electric field. The energy shift caused by this Hamiltonian is called a Stark shift. Let us see why this Hamiltonian, for fundamental particles such as the electron, violates time symmetry and violates parity symmetry (separately, not as a product of parity and time).

Since an electron is a spin-$\frac{1}{2}$ particle and has only one quantization axis (this is why the fundamental particle part is important), the dipole moment vector $\vec{d}$ is aligned or anti-aligned with the spin vector. That is,

$$\vec{d} = d\,\frac{\vec{S}}{|\vec{S}|} \tag{1}$$

Therefore, the Hamiltonian becomes:

$$H_{d_e} = -d\,\frac{\vec{S}}{|\vec{S}|} \cdot \vec{E} \tag{2}$$

Now, by reversing time, only $\vec{S}$ reverses sign and $\vec{E}$ does not. On the other hand, by reversing parity, only $\vec{E}$ reverses sign and $\vec{S}$ does not. $\vec{S}$ is an angular momentum so it is an axial vector. Thus it does not change sign under parity inversion. $\vec{E}$ can be visualized as formed by two charges separated in space, so reversing the coordinates of the charges will flip the direction of $\vec{E}$.

Now that we have argued that the electron's EDM (eEDM) is an interesting property to measure, let us discuss how to measure it. The Stark shift caused by the electron's EDM (eEDM) can be measured through spin precession measurements. The eEDM of magnitude d_e will shift the Larmor precession frequency by an amount $\Delta\omega = 2d_e\mathcal{E}_{eff}$, where $\mathcal{E}_{eff}$ is the effective electric field experienced by the electron[58]. In this section we work in the units where $\hbar = 1$. The shot-noise-limited uncertainty of a measurement in $\Delta\omega$ is given by

$$\delta\omega = \frac{1/\tau_c}{\sqrt{N}} \tag{3}$$

where τ_c is the coherence time and N is the number of molecules detected throughout the measurement. Therefore, the uncertainty in d_e can be written as

$$\delta d_e = \frac{1/\tau_c}{2\mathcal{E}_{eff}\sqrt{N}} \tag{4}$$

Therefore, larger τ_c, $\mathcal{E}_{eff}$, and N will all improve the statistical sensitivity. The advantage of using polar molecules with a high-Z atom is that they tend to have large internal electric fields that contribute to $\mathcal{E}_{eff}$. In fact, it is known to a good approximation that $\mathcal{E}_{eff}$ scales as $\mathcal{E}_{eff} \propto Z^3$ [30,25,48]. These internal fields are much larger than those of atoms, and they can be oriented easily to the lab fields.

Another property that would be useful for such measurements is robustness against systematic effects. Here we will describe two ways to improve on this front. First, by trapping molecules in a small volume, one can obtain better control over the external lab fields. In addition, by varying the interrogation time in the traps, one can subtract out any constant offset phases in the precession by taking differences between different interrogation times[50,21]. Second, having a switch to reverse the molecule's internal field without flipping any external fields can lead to cancellation of systematic effects[4,10]. Note that this internal field switch is separate from switching the lab field itself. On top of the lab-field switch, it would be even more desirable to be able to switch the molecule polarization direction without switching the lab field, since reversing the lab field itself can add sources of systematic effects, such as field offsets from leftover charges.

One simple example of systematic error rejection is the following. Assume an external stray B-field that adds a Zeeman shift on top of the Stark shift. By flipping the polarization of the molecule, only the Stark shift gets reversed and the Zeeman shift does not. By comparing the two measurements, one can subtract out the non-flipping Zeeman shift.

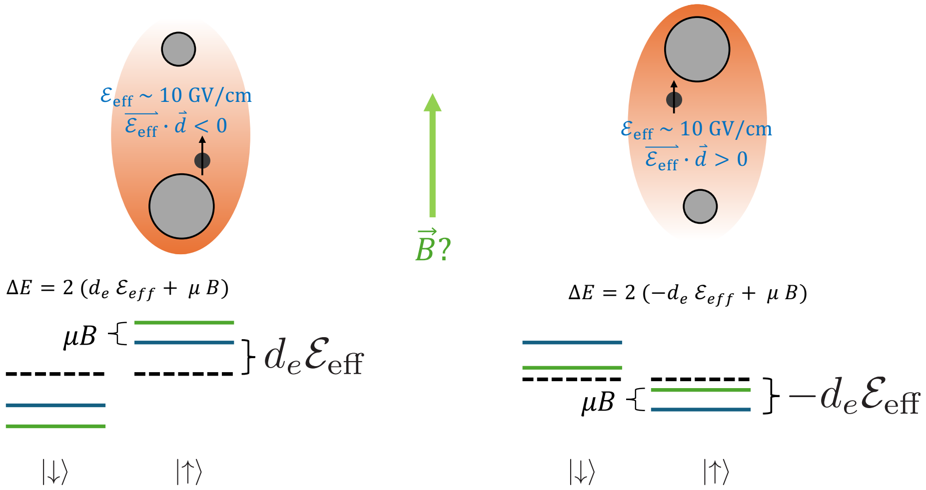

Figure 1: Example of canceling out the first-order Zeeman shift by flipping the molecule orientation.

Then, how can one obtain such a switch of the molecule orientation? The key is to find a level structure with closely lying opposite parity states, or parity doublets. Parity doublets, which are sufficiently closely spaced in energy (compared to other states with opposite parity), can be fully mixed by applying a moderate electric field without significantly affecting other nearby states. These pairs of states have opposite signs of polarizability. One can select the desired sign by optically preparing the molecule in a specific state.

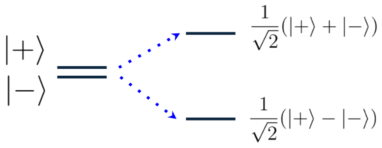

Figure 2: Visualization of parity doublets mixing in the presence of moderate external electric field, resulting in two states with opposite polarizations.

One advantage of linear triatomic molecules is the availability of nearby parity doublets in the ground electronic state (which has a relatively long lifetime). A bending mode in a linear triatomic molecule can be described as a linear combination of two rotations in opposite directions around the internuclear axis. These counter-rotating motions have opposite parity, and as a result, the bending modes give rise to parity doublets, also known as ℓ-doublets[40].

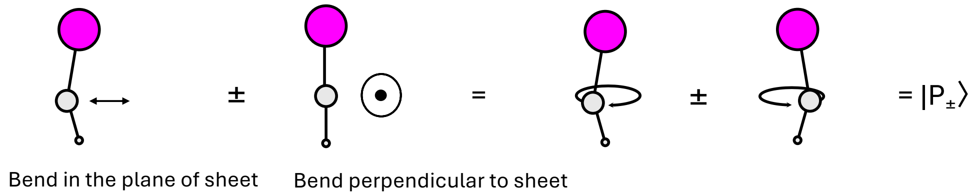

Figure 3: Visualization of ℓ-doublets in the bending modes of linear triatomic molecules.

There are two state-of-the-art experiments setting limits on the eEDM. One is the ACME collaboration using a cold molecular beam of ThO molecules[4,10], and the other is the JILA eEDM experiment using trapped molecular ions[50,21].. Both experiments use molecular species with high Z. In the ACME experiment, a large N is achieved by using neutral species in a cold beam. Furthermore, by conducting the measurement in a state with closely-lying parity doublets arising from an electronic structure, they can switch between polarizing the molecules to and against the electric field. However, in the ACME experiment, measurements were done on a molecular beam, which limited the coherence time to a few milliseconds, corresponding to the beam transit time through an apparatus of a reasonable size[40].

In the JILA trapped molecular ions (HfF^+, and ThF^+ for the next generation[46]) experiments, the long coherence time, over 700 ms[50], is achieved by trapping the molecules. However, charged species will have a smaller limit on the number that can be trapped at once compared to neutral species, due to the Coulomb interactions between them.

Ultracold heavy polyatomic molecules, such as SrOH and YbOH, have the potential to be a good platform for eEDM searches, because they have all the favorable properties discussed above[40]. First, they are molecules with heavy nuclei, so they have a large effective electric field $\mathcal{E}_{\text{eff}}$ experienced by the electron orbiting the molecule. They have a high polarizability required to access $\mathcal{E}_{\text{eff}}$, arising from the bending mode parity doublets. Such parity doublets allow switches of the $\mathcal{E}_{\text{eff}}$ relative to the external lab field. By laser cooling and trapping these neutral species, large τ_c and N can be achieved. Approximately 10^3 trapped YbOH molecules or 10^4 trapped SrOH molecules provide sensitivity competitive with current eEDM limits, assuming the following reasonable parameters: The science state lifetime of 750 ms[57], decoherence of 0.1/s, dead time between measurements of 10 ms, integration time of $24 \times 7 = 168$ hours, and detection contrast of 1. This also serves as a proving ground for molecules with higher intrinsic sensitivity (e.g., RaOH[62]) or symmetric- and asymmetric-top molecules that have parity doublets with longer lifetimes (e.g., $SrNH_2$, $SrOCH_3$[29]), owing to the moment of inertia along the internuclear axis in their vibrational ground states.

0.3 Dark Matter detection with SrOH

There are extremely diverse models of Dark Matter. In certain models of Dark Matter, there are motivations to search for ultralight Bosonic Dark Matter, which spans the mass range of $10^{-22} - 1$ eV[7,53,32,17,9,54,20,24]. Scalar dark matter particles with masses less than 1 eV would be cold and possess large Compton wavelengths. These characteristics allow them to form a Bose-Einstein condensate (BEC) or a superfluid state. As a consequence, such a field would behave as an oscillating background field. When this oscillating field couples to ordinary matter, it can lead to oscillations in fundamental physical properties or constants.

Among one of those constants is the proton-to-electron mass ratio $\mu = m_p/m_e$[41]. Vibrations in molecules depend on this ”constant” μ, which in first order can be written as:

$$\omega = \sqrt{\frac{k}{m}} \propto \sqrt{\frac{m_e}{m_p}} \tag{5}$$

The physical intuition behind this equation is that the spring constant k is a property of the electronic bonding of the molecules, so it has dependence on m_e. The reduced mass m is dominated by the nuclei masses in the molecule, so it is related to the proton mass m_p.

For measuring drifts or oscillations of μ, one can either look out in space (long look-back time) or measure precisely on ultracold molecules (high statistical sensitivity and reduced systematics).

Since vibrational potentials in molecules are not perfect harmonic oscillators (they have anharmonicity), there are also higher-order dependences such as

$$\omega \propto c^{(1)} \sqrt{\frac{m_e}{m_p}} + c^{(2)} \frac{m_e}{m_p} + \ldots \tag{6}$$

Therefore, by measuring energy differences between states that have different anharmonicities, one can be sensitive to oscillations in μ.

In SrOH, it turns out that there is a coincidental degeneracy between two different types of vibration modes. One is the (200) state, which has two quanta of stretching modes, and the other is the (03^10) state, which has three quanta in the bending mode[41].

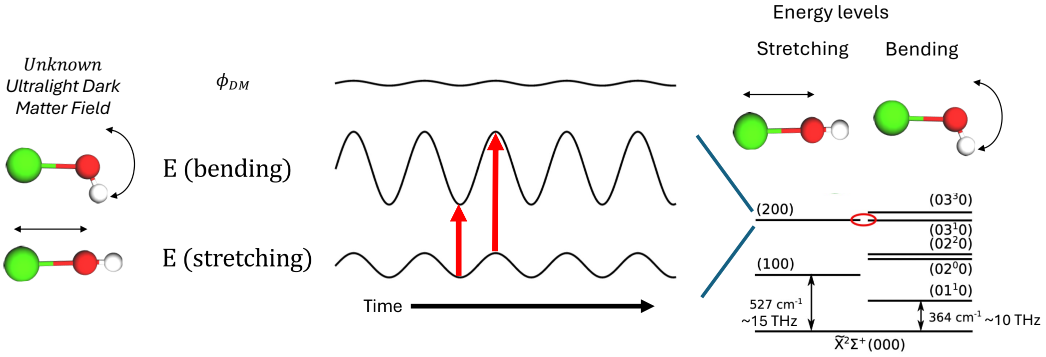

Figure 4: Ultralight Dark Matter detection scheme in SrOH. Modified from ref.[41]

Using these nearly degenerate (about tens of GHz) states, the fractional sensitivity to sense variation in energy differences can be relaxed, thus making SrOH a good candidate for detecting ultralight Dark

Matter. Approximately 10^3 trapped SrOH molecules provide sensitivity competitive with current limits of ultralight Dark Matter in the mass range of 10^{-22} to 10^{-14} eV[41]. A ~week of averaging with 10^3 trapped SrOH molecules would be sensitive to variations in μ by $\delta\mu/\mu \sim 10^{-15}$. This μ variation can be converted to the dilaton coupling to the electron mass d_{m_e} through the Lagrangian[7]

$$\mathcal{L}_\varphi = -\kappa\varphi d_{m_e} m_e \bar{e} e$$

. Projected sensitivity of d_{m_e} and comparison to best limits to date (α variation measurements in atomic clock comparisons) are shown in Fig. 5

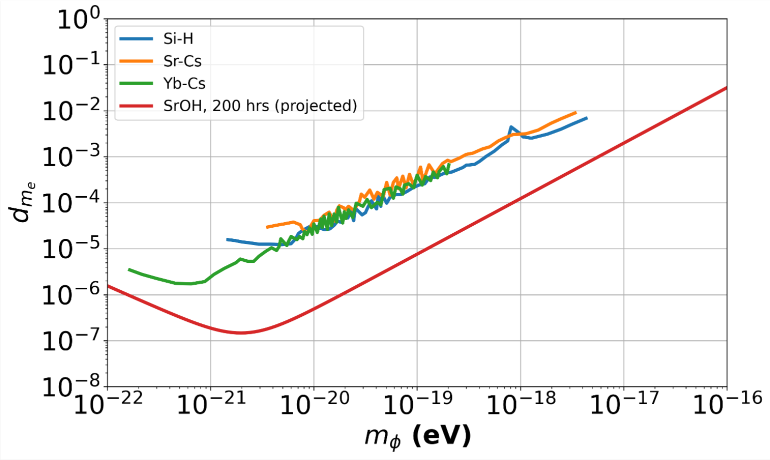

Figure 5: Ultralight Dark Matter sensitivity projection of measurements on $1,000$ SrOH molecules with 200 hours of averaging. Clock comparison data from Ref.[37]. Figure compiled by Mingda Li.

0.4 Approaches to ultracold heavy polyatomic molecules

Unlike atoms, molecules tend to have poor branching ratios because they can decay into various vibrational states. As a result, many lasers are required to repump the population back into the cooling cycle. However, decays into other rotational states can often be effectively suppressed by exploiting angular momentum and parity selection rules.

It is possible to select molecules that exhibit more favorable branching ratios for laser cooling. To date, species such as SrF[11], CaF[5,59], YO[23], CaOH[56], BaF[61], and SrOH[43] have all been successfully laser-cooled and trapped in magneto-optical traps (MOTs). However, even these molecules typically require from a few to up to $\sim$ 10 repump frequencies to maintain the optical cycling necessary for cooling. For efficient direct laser cooling, the goal is to suppress vibrational leakage to the level of about 10^{-4}, enabling a photon budget on the order of 10^4 scattered photons per molecule.

In this thesis, we demonstrate two ways to push forward from here. One is to bite the bullet and repump all vibrational states required to obtain a good photon budget. Another way is to develop a method to remove energy from molecules with few photon scatters. The former approach was taken with SrOH, and described in Chapters 2 and 3 of this thesis. The latter approach was taken for YbOH, which is described in Chapter 4 of this thesis.

0.5 THIS THESIS

In this thesis, we will describe laser cooling and optical trapping of SrOH, and Zeeman-Sisyphus deceleration of YbOH. In Chapter 1, we will begin with a brief overview of molecular energy structure to understand the different energy and angular momentum levels involved in optical cycling of such molecules. In Chapter 2, we will describe the methods required to laser cool SrOH, from radiative slowing to achieving a MOT with lifetimes approaching 200 ms. In Chapter 3, we describe how to take this MOT to an even colder and denser sample of molecules, and loading an optical dipole trap from such a sample. Finally, in Chapter 4, we describe a novel deceleration method for heavy polyatomic molecules, and discuss the subtleties involved when we applied this method to deceleration of YbOH.

1

Molecular Structure

To understand the energy structure of linear polyatomic molecules such as SrOH or YbOH, it is helpful to first review the structure of atoms, then review the structure of diatomic molecules, and finally build towards linear triatomic species. The purpose of this thesis is to give a broad introduction. Reading Benjamin Augenbraun's thesis is highly recommended for more details.

1.1 ATOMS

First, let us review the structure of atoms. This forms the foundation for understanding angular momentum structure. Depending on the symmetries of the system, some types of angular momenta can be good quantum numbers and can represent different energy states.

Three very important quantum numbers here are $\mathbf{S}$, $\mathbf{L}$, and $\mathbf{J}$. These are the electron spin quantum number ($\mathbf{S}$), orbital angular momentum ($\mathbf{L}$), and total angular momentum ($\mathbf{J}$), respectively. $\mathbf{S}$ and $\mathbf{L}$ add up to form $\mathbf{J}$. The mechanism of $\mathbf{S}$ and $\mathbf{L}$ adding up is called spin-orbit coupling. Note that these are all angular momentum vectors, so they add in a ”vector” way. They can either align or anti-align along the quantization axis.

For example, the energy level (simplified up to fine structure) of Rubidium atoms is shown in Fig. 1.1.

This will be useful to keep in mind as we move on to diatomic molecules, where there is another additional source of angular momentum.

Although $\mathbf{S}$ and $\mathbf{L}$ originate from different physical phenomena, they are both quantized with the same unit $\hbar$. Therefore, we are allowed to simply add the number of quanta of different types of angular momentum. Angular frequencies and magnetic *g*-factors differ between types of angular momentum, so quantities such as rotational energies and magnetic moments require respective scalar factors to be multiplied before adding the angular momenta. This also holds for angular momentum that arises from rotations of the nuclei in molecules, which we typically take for granted can be added to angular momentum arising physically from the electronic side.

1.2 DIATOMIC MOLECULES

Moving from atoms to diatomic molecules, there are a few new concepts that must be addressed to understand the energy structure. We will list them first and then explain them in further detail through-

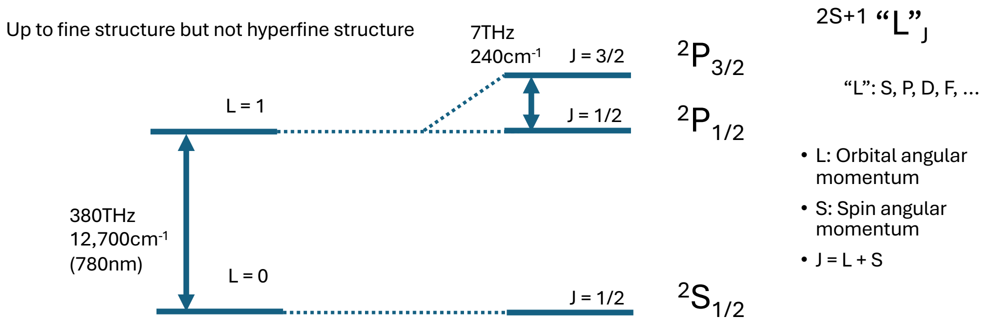

Figure 1.1: Example of an atom structure. Energy scales are for Rb atoms.

out this chapter.

- Vibrations in stretch modes do not add any additional angular momentum. Instead, they replicate the same angular momentum structure, typically separated by tens of terahertz (THz).
- Rotations (visualized as head-to-tail motion) do add angular momentum, which is commonly denoted as $\mathbf{R}$.
- The intermediate angular momentum excluding rotation is given by:

  $$\mathbf{J}_a = \mathbf{L} + \mathbf{S}$$

  where $\mathbf{L}$ is the electronic orbital angular momentum and $\mathbf{S}$ is the electronic spin.
- The total angular momentum, including rotation, is:

  $$\mathbf{J} = \mathbf{L} + \mathbf{S} + \mathbf{R}$$

- In linear molecules, the projections of angular momentum vectors onto the internuclear axis are good quantum numbers:
  - Λ: projection of $\mathbf{L}$
  - Σ: projection of $\mathbf{S}$
  - Ω: projection of $\mathbf{J}_a$

1.2.1 From spherical symmetry to cylindrical symmetry

Since the internuclear axis reduces the symmetry of the molecule from a spherically symmetric atom, the projections of angular momentum vectors onto the internuclear axis are good quantum numbers:

Λ is the projection of $\mathbf{L}$, Σ is the projection of $\mathbf{S}$, and Ω is the projection of $\mathbf{J}$. The angular momentum itself is not guaranteed to be a good quantum number.

Thus, the labels of the electronic states used in atoms should be mapped onto projections:

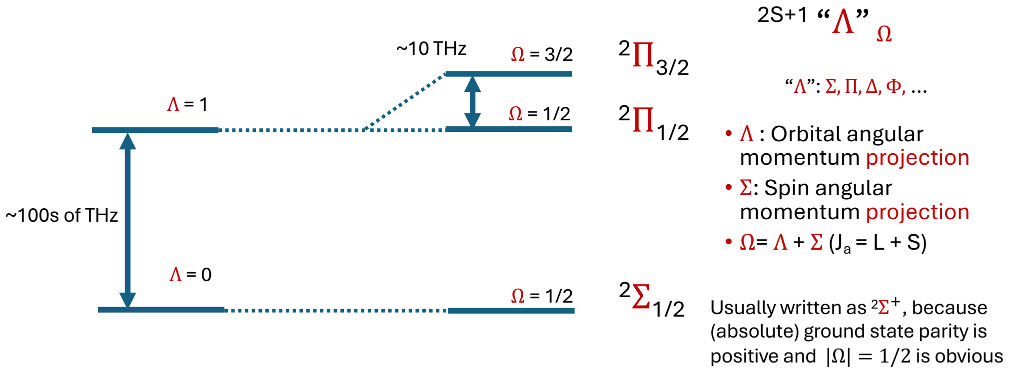

Figure 1.2: Mapping atom structure to projection labels.

1.2.2 BORN-OPPENHEIMER APPROXIMATION

The Born-Oppenheimer approximation states that, to a good approximation, the motion of the nuclei is decoupled from the electronic behavior[14]. For details, see Refs.[35,15].

1.2.3 Vibrational States

Vibrations in molecules arise from the motion of the nuclei. Therefore, by the Born-Oppenheimer approximation, to first order, we do not need to worry about vibrational states coupling into the angular momentum structure. One example of a breakdown of this approximation is the Renner-Teller coupling[18], which will be explained later in Chapter 2 when discussing the $\tilde{A}^2\Pi(020)$ state structures. However, we will not worry about those states for now. In states where the Born-Oppenheimer approximation holds well, vibrational states form the next hierarchy after electronic structure. The energy scales of these vibrations are on the order of 10 THz. Each vibrational quantum gives rise to a vibrational manifold, which does not add angular momentum; thus, within each vibrational manifold, there are exact copies of the angular momentum structure.

1.2.4 Rotational States

Another major difference from atoms is the rotational structure of molecules. In diatomic molecules, the head-to-tail rotation gives rise to rotational angular momentum with $\sim$ tens of GHz frequency (or energy). This angular momentum is usually denoted $\mathbf{R}$, and its projection along the internuclear axis is denoted K_R.

Depending on the molecular state, the hierarchy of angular momentum components changes. These different hierarchies are categorized into five types called Hund's cases. In this thesis, we cover Hund's case (a) and (b), which are relevant to the states we work with.

In diatomic molecules, we do not consider rigid-body rotation around the intermolecular axis because the moment of inertia along that axis is zero. Exciting a rotation around this axis would require infinite energy, even to reach the minimally quantized rotation that carries angular momentum $\hbar$, and thus is not experimentally meaningful.

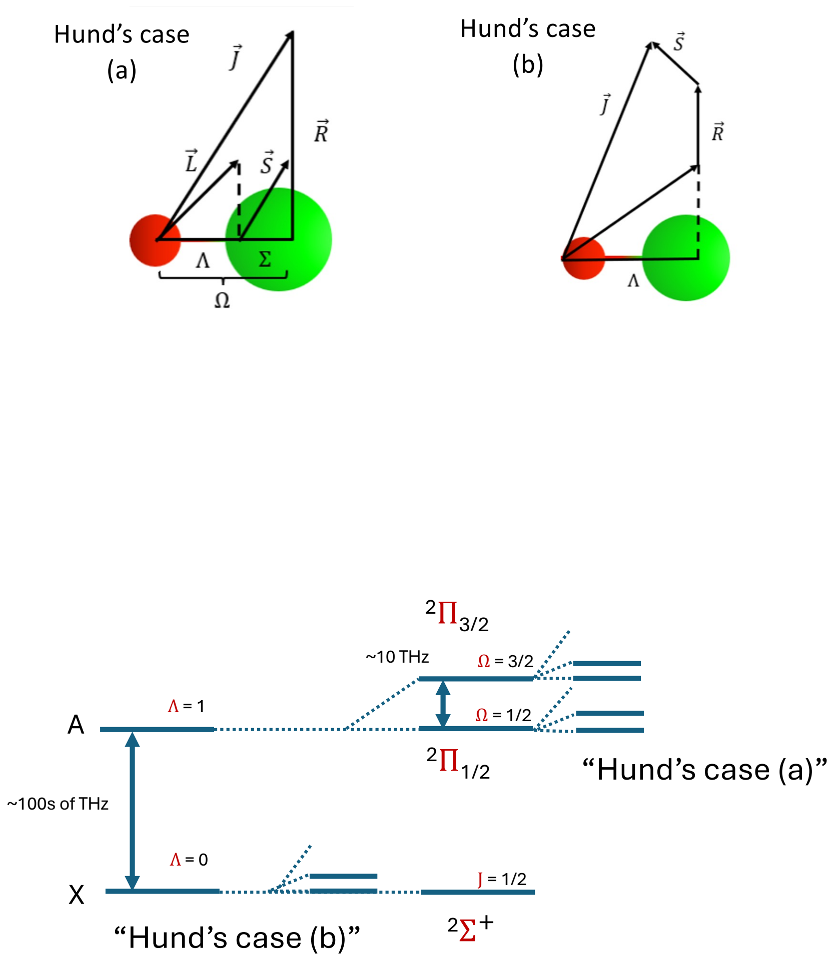

Figure 1.3: Top: How angular momenta add in different Hund's cases. **Bottom:** Illustration of how to add rotational energy ladders in the hierarchy: either after the spin-orbit coupling (case (a)) or before the spin couples to the orbital angular momentum (case (b)). The Σ ground state is Hund's case (b), and the Π excited state is Hund's case (a).

1.2.5 HUND'S CASE

The intuitive picture of Hund's cases is the following: when adding the rotational angular momentum projection to the other angular momentum projections, where should it be added?

In Hund's case (a), K_R is added after adding Λ and Σ, meaning it is added last in the hierarchy. Therefore, Ω remains a good quantum number, and the total rotational quantum number excluding nuclear spin, $\mathbf{J}$, and its projection $P = \Omega + K_R$ are also good quantum numbers. This P quantum number is sometimes referred to as the "total projection quantum number."

In Hund's case (b), $\mathbf{R}$ is added to $\mathbf{L}$ first, resulting in the rotation quantum number excluding spin, $\mathbf{N} = \mathbf{L} + \mathbf{R}$. Therefore, Ω is no longer a good quantum number in this case. The electron spin angular momentum $\mathbf{S}$ is then added to $\mathbf{N}$ to form $\mathbf{J} = \mathbf{N} + \mathbf{S}$. Note that in more general (polyatomic) molecules, the definition of $\mathbf{N}$ includes additional components, which will be explained later.

1.2.6 Λ-TYPE DOUBLING

Λ-doubling is a small energy splitting that occurs in molecules with nonzero electronic orbital angular momentum projected onto the internuclear axis. The electronic wavefunction has two degenerate components corresponding to $+\Lambda$ and $-\Lambda$. These would be exactly degenerate in the absence of additional interactions. However, rotational and vibronic interactions lift this degeneracy slightly, resulting in a splitting of each rotational level into two closely spaced sublevels of opposite parity. This effect is known as Λ-doubling. The splitting increases with rotational quantum number J, and is often labeled using parity labels such as $+$ and $-$. In many spectroscopy papers, the e and f labels are used to describe symmetries; these do not correspond one-to-one with $+$ and $-$ parity, as they represent a combination of parity and total angular momentum[19].

1.2.7 HYPERFINE STRUCTURE

For completeness, we introduce the nuclear spin $\mathbf{I}$. Adding this to $\mathbf{J}$ gives the total angular momentum $\mathbf{F}$. In our experiments, hyperfine structure was on the order of 1 MHz and was unresolvable.

1.3 LINEAR TRIATOMIC MOLECULES

1.3.1 MORE TYPES OF VIBRATION

In linear triatomic molecules, there are three distinct vibrational modes: antisymmetric stretch, bend, and symmetric stretch, denoted by vibrational quantum numbers (v_1, v_2, v_3), respectively.

1.3.2 THE BENDING MODE

The v_2 mode is doubly degenerate, as the bending can occur in two perpendicular planes. Linear superpositions of these bending motions result in a kinked triatomic molecule rotating either clockwise or counterclockwise about its symmetry axis, giving rise to angular momentum $\mathbf{G}$ and projection ℓ (though it is technically a vibrational state). For example, in the $v_2 = 1$ mode, there are two states with $\ell = \pm 1$, denoted $|v_2^{\pm 1}\rangle$. Coriolis interactions lift the degeneracy between the even and odd parity states $|v_2^{+1}\rangle \pm |v_2^{-1}\rangle$, resulting in a parity doublet of size ~ 10 MHz[40] (see Fig. 2 and Fig. 3).

Note that ℓ can only take values $|\ell| = v_2 - 2n$, where $n = 0, 1, 2, \ldots$. This arises from properties of 2-D harmonic oscillators[49].

In linear triatomic molecules, the definition of $\mathbf{N}$ includes $\mathbf{G}$, so $\mathbf{N} = \mathbf{L} + \mathbf{R} + \mathbf{G}$.

1.4 SELECTION RULES AND OPTICAL CYCLING

Since many of the previous theses in the Doyle group cover details of the selection rules, this thesis will focus on the essential concepts.

For vibrational modes, there are no strict selection rules. Some decays are still more favored than others (higher branching ratios). This is largely due to better overlap between ground and excited vibrational wavefunctions.

The Franck-Condon factor $q_{v',v''}$ quantifies how well the vibrational (nuclear) wavefunctions are overlapped:

$$q_{v',v''} = \left| \int \psi^*_{v'}(R)\, \psi_{v''}(R)\, dR \right|^2$$

where $\psi^*_{v'}(R)$ and $\psi_{v''}(R)$ are the vibrational wavefunctions in the excited and ground electronic states, respectively.

Decays with higher Franck-Condon factors have higher probabilities. The decay probability also scales with ω^3, where ω is the angular frequency of the transition.

Molecules such as SrOH and YbOH were chosen because their branching ratios are more controllable than most other molecules—decays to higher vibrational states are highly suppressed due to the high Franck-Condon factor between the $\tilde{A}^2\Pi_{1/2}(000)$ excited state and the $\tilde{X}^2\Sigma^+(000)$ ground state, which is about 90%[40,42].

For rotational selection rules (E1 decays), $\Delta\mathbf{J} \leq 1$ must be satisfied, and the parity must flip. Between the $\tilde{A}^2\Pi$ and $\tilde{X}^2\Sigma^+$ states, a closed cycle can be established by exciting from the $\mathbf{N} = 1^-$, $\mathbf{J} = 1/2, 3/2$ states to the $\tilde{A}^2\Pi, \mathbf{J} = 1/2^+$ state (see Fig. 1.4)[55]. The $\tilde{A}^2\Pi, \mathbf{J} = 1/2^+$ state will always decay to the $\mathbf{N} = 1^-, \mathbf{J} = 1/2, 3/2$ states, since the next highest $\mathbf{J}$ state with negative parity is the $\mathbf{N} = 3^-, \mathbf{J} = 5/2$ state. Note that the $\mathbf{N} = 2^+, J = 3/2, 5/2$ state has positive parity. Also note that the $\mathbf{N} = 1^-, \mathbf{J} = 1/2, 3/2$ states in the ground $\tilde{X}^2\Sigma^+$ manifold have more sublevels than the $\tilde{A}^2\Pi, \mathbf{J} = 1/2^+$ state. Transitions with more ground than excited sublevels are called type-II transitions and require additional care when implementing laser cooling.

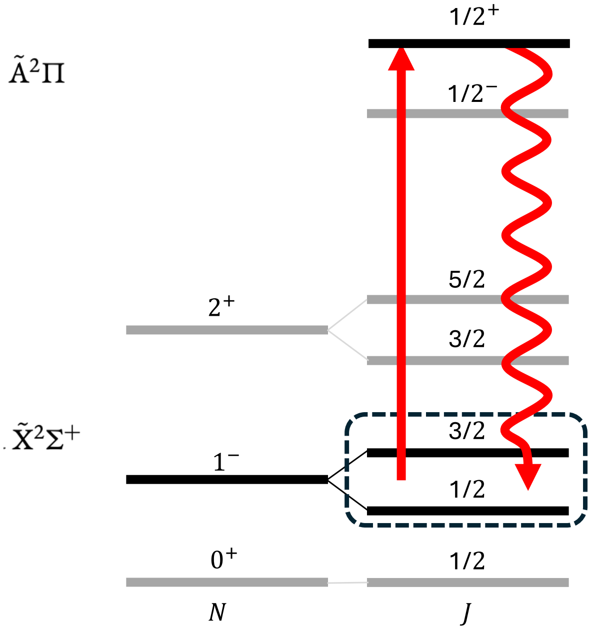

Figure 1.4: Diagram of rotational selection rules

2

Magneto-optical Trapping of SrOH

In this section, we describe the procedures to laser cool SrOH using 12 (initially 10) different laser frequencies. We begin by detailing how the molecules are produced in a cryogenic buffer gas beam (CBGB). Then, we discuss radiative slowing and magneto-optical trapping of SrOH. This thesis focuses on technical details that were not immediately obvious at the outset. For further information, see Alexander Frenett's thesis. Finally, we discuss in-MOT spectroscopy used to identify additional repumping states that improve the MOT.

2.1 PRODUCTION

2.1.1 BUFFER GAS BEAM SOURCE AND CELL DESIGN

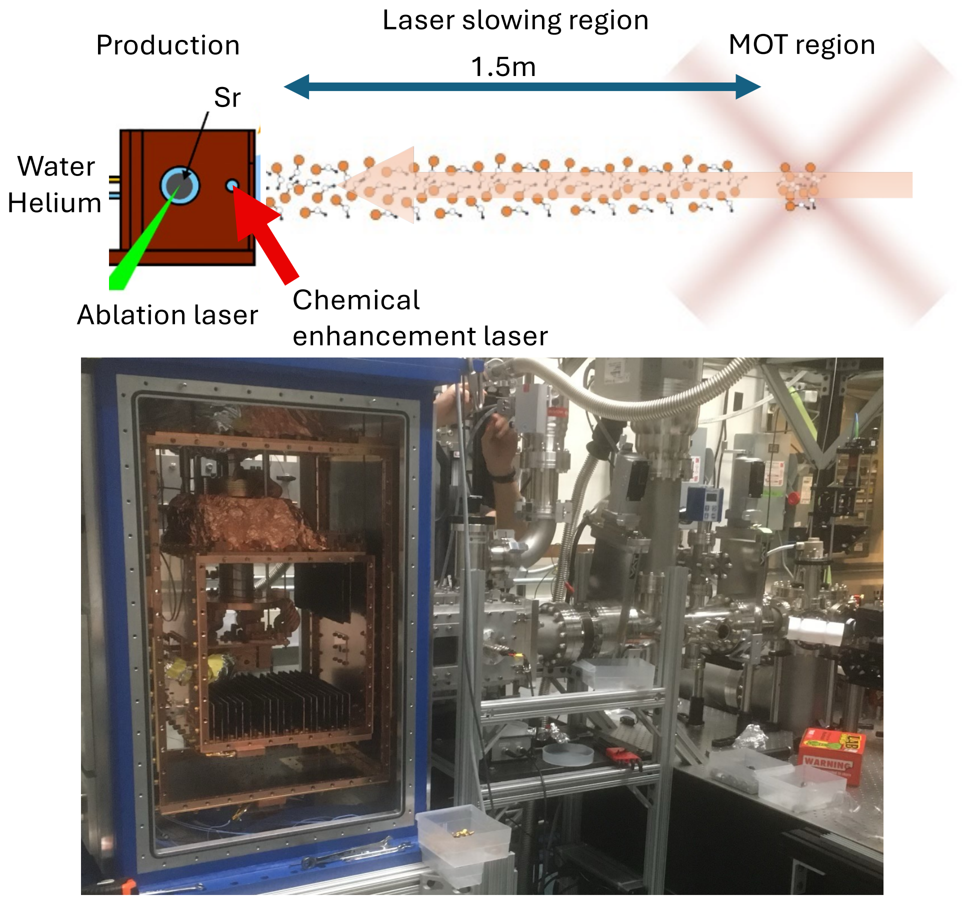

Figure 2.1: Overview of the buffer gas beam source and beamline for the SrOH experiment.

We start with a 2 K source of molecules produced in a buffer gas cell. We constructed a beam box, described in detail in Appendix A. In this 2 K cell, SrOH molecules are produced and extracted into the slowing beamline.

Production begins by ablating a Sr metal target with a pulsed Nd:YAG laser at 532 nm. This laser is typically run at $\sim$ 20 mJ per pulse. Room-temperature water vapor is flowed in to react with the ablated Sr and produce SrOH. The water vapor is fed through heated fill lines (described in Appendix A), which are usually kept at $\sim$ 285 K.

To enhance the chemical reaction, the strontium atomic transition is driven to the metastable $^3P_1$ state. The chemical enhancement laser at 688 nm is operated with $\sim$ 1 W of power and a beam diameter of $\sim$ 1 mm.

This facilitates the reaction

$$\mathrm{Sr} + \mathrm{H_2O} \rightarrow \mathrm{SrOH} + (\text{other products}),$$

by making the reaction exothermic, which improves SrOH production efficiency[36,16]. The helium in the buffer gas cell thermalizes with the cold cell walls, cools the SrOH molecules, and entrains them into a molecular beam with a forward velocity of approximately $\sim$ 100 m/s. For this experiment, we use the isotopologue of SrOH without nuclear spin on the Sr atom, nameley ^{88}SrOH.

2.2 RADIATIVE SLOWING

2.2.1 REPUMPING VIBRATIONAL STATES

As explained in the Introduction and Molecular Structure chapters, although the $\tilde{A}^2\Pi_{1/2}$ (000) excited state decays back $\sim$ 90 percent of the time to the $\tilde{X}^2\Sigma^+$ (000) ground state, SrOH has non-negligible branching ratios to several vibrationally excited states (referred to as "vibration states") within the electronic ground manifold. To scatter order 10^4 photons,[*] we initially combined 10 different laser frequencies, each addressing a different vibrational state.

The laser cooling scheme was based on spectroscopy results identifying which vibrational states

---

[*] this would allow a deceleration from 100 m/s to 10 m/s with less than 1/e loss to unaddressed states.

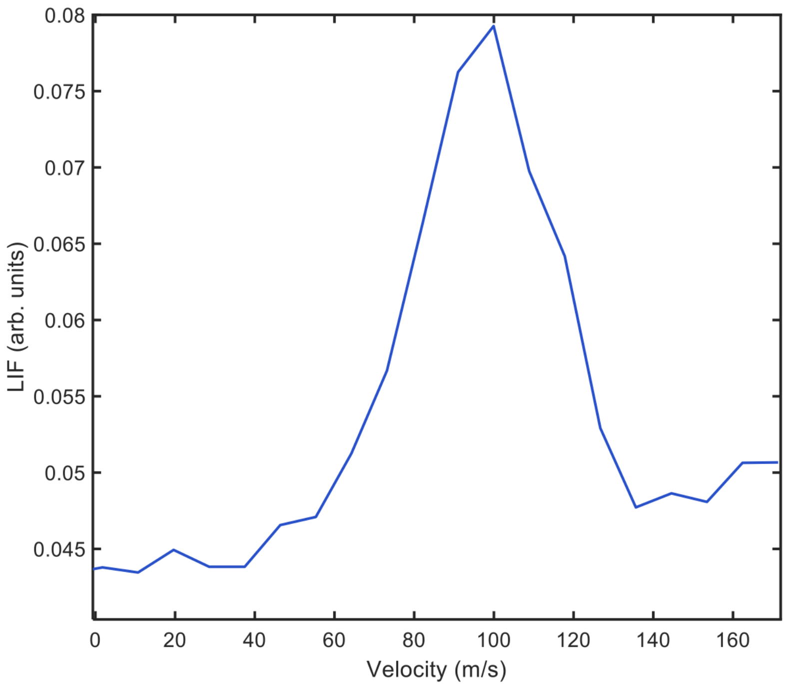

Figure 2.2: Measured forward velocity of SrOH from the buffer gas source.

become populated as photons are scattered from SrOH[42]. The main transition is at 688 nm, driving the X(000) state to the A(000) state. No other repumping transitions go through the A(000) state in order to maintain a high scattering rate on the main line. This is because, as more ground states are coupled to a given excited state, the effective scattering rate decreases proportionally due to stimulated emmision into less poulated ground states.

For each repumping laser, we measured the rate at which it pumps molecules out of its corresponding vibrational state. Generally, this was done by first populating the vibrational state of interest (by turning on only repumps for more frequently populated states) and then turning on the repump laser of interest for a variable duration. We then measured how much population was pumped back into the ground state as a function of time. Although the repump transition strength can be roughly estimated from the change in vibrational quantum number, it is important to know the exact pumping rate to determine which repump transition limits the overall repumping rate.

The following model explains how to determine whether a repump transition is bottlenecking the overall scattering rate. Let $\bar{f}_i$ denote the branching ratio to the i-th vibrational state. For an optical cycle involving multiple excited states, $\bar{f}_i$ can be taken as the weighted average of the branching ratios among the excited states, based on how often each is visited. These averages can be obtained by constructing a Markov chain model using the measured branching ratios. Let Γ_i denote the repumping rate out of state i. One might naively expect that $\Gamma_i = \Gamma_{\text{in}}$, where Γ_{in} is the rate at which molecules are pumped into state i, is sufficient. However, this is not the case.

The scattering rate for the full optical cycle is given by the harmonic mean of the scattering rates:

$$\Gamma_{\text{cycle}} = \frac{1}{\sum_i \bar{f}_i / \Gamma_i}. \tag{2.1}$$

This is analogous to calculating an average velocity. If a particle travels distances x_i at speeds v_i, then the average velocity is:

$$v_{\text{avg}} = \frac{x_{\text{total}}}{\sum_i x_i / v_i}. \tag{2.2}$$

In this analogy, $\bar{f}_i$ represents how long a molecule typically spends in a particular vibrational state, and $\sum_i \bar{f}_i / \Gamma_i$ represents the average time spent per photon scatter.

To illustrate the dependence of Γ_{cycle} on repumping rates, we consider a simple case. Let $i = 0$ represent the ground state X(000), and $i > 0$ represent excited vibrational states. The main scattering rate is $\Gamma_0 \approx 2$ MHz, set by the rate at which we polarization switch to destabilize dark states. When analyzing a partial optical cycle, we renormalize the $\bar{f}_i$ values to sum to 1.

In this setup, transitions with large f_i / Γ_i will bottleneck the cycle. For the cycle to not be limited by these repumped states:

$$f_i / \Gamma_i \ll f_0 / \Gamma_0. \tag{2.3}$$

This implies:

$$\Gamma_i \gg \left(\frac{f_i}{f_0} \right) \Gamma_0 = \frac{\Gamma_{\text{in}}}{f_0} \simeq \Gamma_{\text{in}}. \tag{2.4}$$

Thus, $\Gamma_i = \Gamma_{\text{in}}$ is not sufficient for maintaining a high Γ_{cycle}. If m repumping transitions each have rate $\Gamma_i = \Gamma_{\text{in}}$ and the others satisfy Eq. 2.4, then Γ_{cycle} will drop by a factor of m. If n repumped states all have limiting repumping rates of $\Gamma_i = n\Gamma_{\text{in}}$, then Γ_{cycle} will decrease by a factor of 2. A practical requirement for efficient repumping is:

$$\Gamma_{\text{out}} / \Gamma_{\text{in}} \gtrsim n.$$

This rate equation model does not capture dynamic processes like slowing and trapping that occur on timescales of ∼1–10 ms. Therefore, an additional condition is needed: $\Gamma_i \gtrsim 1$ kHz, regardless of

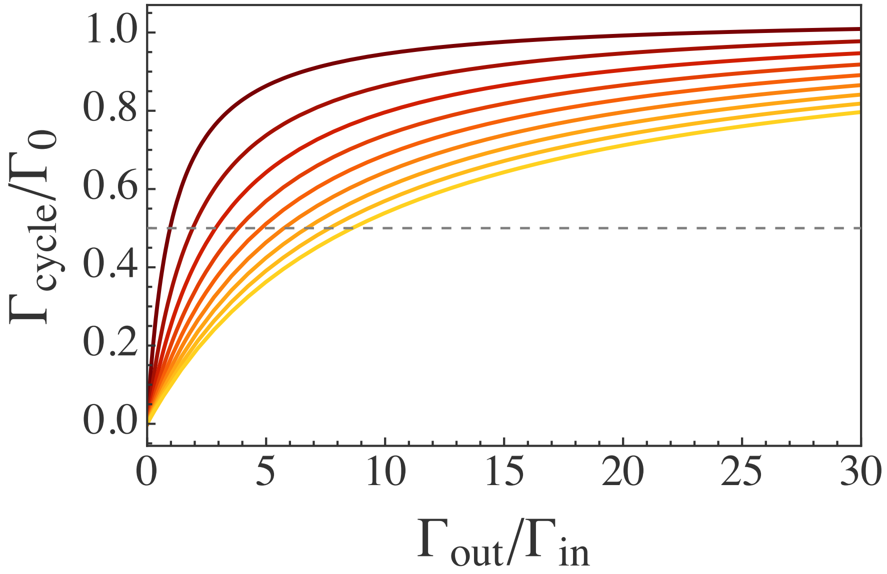

Figure 2.3: The scattering rate of the optical cycle, Γ_{cycle}, relative to the main transition scattering rate, Γ_0, as a function of the characteristic repumping strength $\Gamma_{\text{out}}/\Gamma_{\text{in}}$ for different repumping schemes involving 2–10 lasers (top to bottom). As the number of repumped states increases, the required repumping strength increases. The $\Gamma_{\text{cycle}}/\Gamma_0 = 0.5$ line (dashed) occurs when $\Gamma_{\text{out}}/\Gamma_{\text{in}}$ equals the number of repumped states. Adapted from Ref.[43].

the value of $\Gamma_{\text{out}}/\Gamma_{\text{in}}$. For instance, if a molecule remains in a dark state for ~10 ms, it will likely be lost from the trap, even if that state is populated only after ~100 ms. Consequently, for repumping transitions that occur late in the optical cycle (i.e., $(\Gamma_{\text{in}})^{-1} \gtrsim 10$ ms), the actual required Γ_i may exceed the estimates based on this simple model.

2.2.2 Building daisy-chained SFG systems

To build a robust system with 10 different laser frequencies, some of which exceed 1 W in power, we use high-power SFG systems. We combine two high-power IR lasers on a PPLN crystal to create sum-frequency light for our repump transition lines. Our X-B transitions mostly lie around 630 nm, and this wavelength can be conveniently generated by combining a Yb fiber amplifier at approximately 1064 nm and an Er fiber amplifier at around 1550 nm. The X-A transitions lie around 690 nm, which are made by combining a Yb fiber amplifier at around 1064 nm and a Tm fiber amplifier at approximately 1900 nm. For the Yb+Tm amplifiers, we ordered modules directly from Pecilasers that included combining optics pre-aligned in the laser head module, except for the chemical enhancement laser at 688 nm. For this laser, we combined dumped 1900 nm light from the main line module with separate 1064 nm light. This setup required ordering specific optics for 1900 nm light, and alignment using thermal IR cards. For the Yb+Er fiber amplifier system, we purchased the amplifiers and PPLN crystals from Pecilasers and performed the alignment ourselves. This allowed us to split some fiber amplifier power across multiple SFG systems and to ”daisy chain” some of them, as explained below.

For SFG systems requiring over $\sim$ 1 W of power, we used a ”simple” setup: carefully overlapping two IR beams in a PPLN crystal to convert the light into a visible wavelength. It is important to ensure that not only the pointing but also the focus of the two IR beams is overlapped. The focal point should be at the center of the PPLN crystal, which is mounted on a translation stage for fine position adjustments. The temperature of the PPLN crystal can be tuned to optimize conversion efficiency, which generally follows a sinc function of temperature. Under well-optimized conditions, we achieve up to about 0.08/W efficiency (8 W of visible light output from 10 W $\times$ 10 W IR input). Note that the output power is proportional to the product of the input IR powers.

For lower-power SFG systems, we implemented cost- and space-saving strategies. One simple strategy is to split one of the IR beams into two different SFG systems. In this method, two separate amplifiers are still needed for the other IR wavelength. Another strategy is to seed one of the IR amplifiers with multiple frequency seeds, so that it outputs several different frequencies. This beam is then overlapped with the second IR beam and passed through multiple PPLN crystals in series, each with its own optimized temperature setting for a specific target frequency. Examples of such systems are shown in Fig. 2.4.

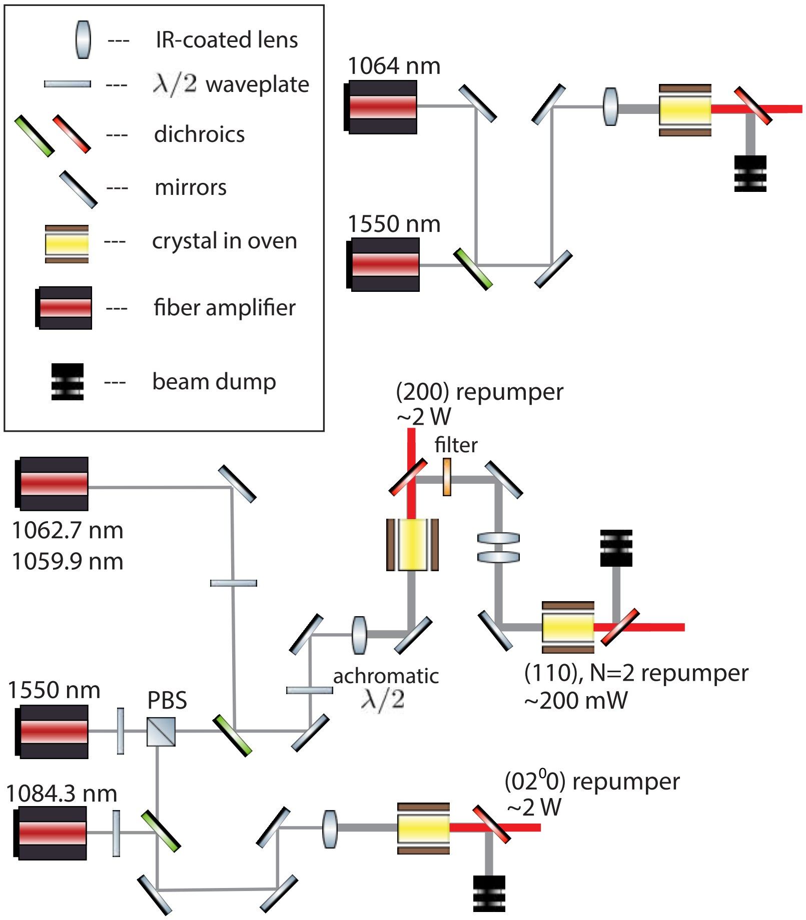

Figure 2.4: Schematic of a sum-frequency generation laser system (top-right) and an example optical path for producing three repumping laser wavelengths via daisy-chained crystals (bottom). Retrieved from Ref.[43].

2.2.3 How to avoid burning SFG crystal oven cases

When aligning high-power IR light into SFG crystals, it is important to ensure the IR beams are not misaligned with other components (such as the crystal casing), as the focused high-power beams can easily cause damage.

The first rule is to verify that visible light is coming out of the SFG crystal at low power before increasing the IR beam intensity. Turning up IR power without visible output is extremely dangerous, as it suggests misalignment. We have damaged multiple SFG crystals by ignoring this principle.

Another important point is to treat any SFG alignment as ”incomplete” if any modifications were made on the same optical breadboard—even if no upstream components were touched, if the stability/make of the breadboard is unknown. In one case, we used a very old breadboard where tightening a screw downstream introduced enough stress to misalign previously aligned optics. This led us to mistakenly ramp up the IR power without rechecking alignment, resulting in a burned plastic housing and a destroyed SFG crystal. We subsequently replaced the breadboard with a sturdier one.

In addition to strictly following the safety protocol of checking for visible light output at low power before increasing IR power, we took further precaution by constructing metal covers to replace the plastic housings. These covers, machined by Xometry, were made of black anodized aluminum (6061-T6) to withstand accidental exposure to high-intensity light.

2.2.4 Combining the slowing lasers

Each of the repump lasers is sent through optical fibers to the main MOT table. For laser frequencies that require less than 1 W, a standard Thorlabs PM fiber is used to deliver the light. However, for higher powers, regular PM fibers are limited by stimulated Brillouin scattering (SBS). SBS occurs because the incoming light nonlinearly interacts with phonons inside the fiber core, resulting in backscattering at a down-converted frequency. To avoid significant SBS, photonic crystal fibers (PCFs), which have much higher SBS limits than regular silica-core fibers, are used. We ordered PCFs with high-power connector ends from Alphanov. The fiber is LMA-PM-15, and the connector at both ends is SMA-6, 8° +/- 1° (including an end-cap $< 100\,\mu$m and handling up to 6 W loss). We can transmit up to about 3 W of 630 nm light through a 10 m PCF of this type. The SBS power limit scales inversely with fiber length, so a 5 m PCF can carry twice that power.

It is important to have the high-power connector on the input side because, for example, if you are coupling 5 W of power into the fiber with 70% efficiency, you are dumping 30% of that power—1.5 W—into the connector. The output side is less critical, so we ordered a 2 W connector there to reduce cost. When coupling into these PCFs, handle the bare fiber tip with extreme care. It has no plastic protection and is surrounded by air to manage high power, making it very easy to break.

Using PCFs and regular silica PM fibers, all laser frequencies are brought to the MOT table and combined. In general, longer wavelengths are combined upstream and shorter wavelengths downstream along the beam path. However, many laser frequencies are so close that it is impossible to achieve high combining efficiency with only dichroic beamsplitters.

One useful trick is to combine two nearby frequencies using a polarizing beam splitter (PBS). As explained later, the polarization of the slowing beam is rapidly flipped during slowing using a Pockels cell. Thus, either horizontal or vertical polarization can be selected for each laser frequency. This trick is limited to two polarizations, so to combine more than two nearby frequencies, we use Bragg grating notch filters (commonly called Optigrates in our lab). These reflect a very narrow frequency band (a few hundred GHz) when aligned at the correct Bragg angle, and pass all other frequencies.

Using Optigrates, one can combine closely spaced frequencies with high efficiency. In theory, any number of nearby frequencies can be combined, though Optigrates are more expensive than standard dichroic mirrors. Even with Optigrates, combining very closely spaced wavelengths ($\lesssim 100$ GHz) can be challenging due to the strict angular alignment required, which often necessitates a micrometer-controlled rotation stage. We used both the PBS and Optigrate techniques to combine all required frequencies.

2.2.5 WHITE LIGHT BROADENING

When slowing molecules with laser light, it is important to ensure they remain resonant with the counter-propagating laser beam despite Doppler shifts as they decelerate. In our initial implementation of SrOH slowing, we used a method called white-light slowing. This technique broadens the frequency of each slowing and repump laser sufficiently so that molecules always see a resonant sideband.

Each laser is passed through a resonantly driven electro-optic modulator (EOM) crystal operating around 4 MHz. The EOM is highly overdriven, producing approximately 100 sidebands that span a range of $300 - 400$ MHz. Throughout the slowing process, molecules are resonant with one of the sidebands spaced roughly 4 MHz apart, since the natural linewidth is about 7 MHz.

As discussed in the molecular structure section, most transitions in SrOH have spin-rotation (SR) splitting of $\sim$ 110 MHz. With a broadening of $\sim$ 300 MHz, both SR sidebands can be addressed, ensuring resonance as the Doppler shift decreases from $\sim$ 150 MHz to 0 MHz during slowing.

For high-power lasers, we keep the frequency broadening minimal to maximize power per sideband. Later, we transitioned from white-light slowing to chirped slowing, which is explained in a subsequent section.

2.2.6 INITIAL SLOWING TO 50 M/S AND TO 25 M/S

To initially verify that slowing was working, we first tested slowing to 50 m/s, as it was a relatively easy signal to confirm that we could slow the molecules at all. Since the required velocity change is relatively small, there is more tolerance in the center frequencies of the slowing lasers. Velocity detection was performed by directing the (100) repump laser beam at 45 degrees into the detection chamber and also exciting the main transition. We optimized for the highest number of detected molecules at 50 m/s. Then, we scanned the frequency of each repump laser individually to determine the frequency range that yields the optimal number of slowed molecules.

Having identified acceptable frequency ranges for slowing to 50 m/s, we proceeded to slow molecules to 25 m/s. We repeated the frequency scans again to determine the optimal frequency range for each laser. The number of molecules that could be slowed to 25 m/s was significantly lower than for 50 m/s, but still sufficient to confirm effective slowing. The results of slowing to 25 m/s are shown in Figure 2.5.

To enable capture in a MOT with reasonable parameters, it is generally necessary to slow molecules to about 10 m/s (of course, it highly depends on the molecular species, laser cooling scheme, and MOT parameters). For example, inside the MOT region, if each photon kick slows a molecule by 5 mm/s at a 1 MHz effective scattering rate over a 1 cm distance, a total slowing of 10 m/s is achievable. However, CaF and CaOH experiments in our group have had difficulty ensuring that slowing to 10 m/s works effectively, primarily due to the low detectable signal in that velocity class. Therefore, we chose to proceed directly to MOT trapping once we confirmed that slowing to 25 m/s was successful.

2.2.7 Adjustments in frequencies required to slow to MOT capture velocity

When moving on to slowing to 0 m/s (or the MOT capture velocity), the following naïve idea led to inefficient slowing. Say the optimal frequency of a certain repump (or the center of the acceptable range for optimal slowing) to 50 m/s is f_{50}, and the optimal slowing frequency for the same laser for slowing to 25 m/s is $f_{25} = f_{50} + f_x$. Then, one may naïvely think that the optimal frequency to slow and stop the molecules to 0 m/s is $f_0 + 2f_x$. However, this logic only holds in an ideal world where the initial velocity distribution is a delta function and all measurements are perfect. In reality, due to imperfections in the measurements, back-of-the-envelope calculations suggested that some of these

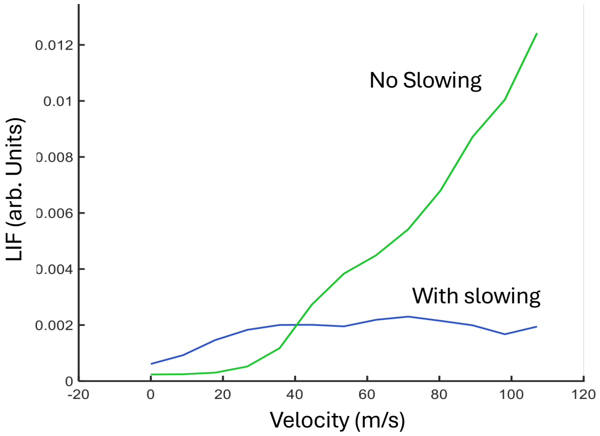

Figure 2.5: Results of slowing to 25 m/s. We observe increased accumulation of molecules in the lower velocity classes in the slowed case compared to the no-slowing case.

extrapolated frequencies were either too blue-detuned to address the fast molecules at the beginning of the slowing, or too red-detuned to slow the molecules to a slow enough velocity.

Although at this point of the experiment we were not completely trapping the molecules (this was with a $d = 1$ cm diameter MOT beams), adjusting slwoing laser frequencies based on the calculations done in this section allowed us to further optimize other elements of slowing with better signal-to-noise ratio to begin with.

In fact, as explained in the paragraph about the main line EOM broadening below, we were at risk of tuning the main line ((000)) laser and the $(010); N = 2$ repump laser in a frequency range with very few slowed molecules (see Fig. 2.8 and Fig. 2.7) if we had not been aware of this calculation and had not overbroadened one of the white-light EOMs as a safeguard. Evidence for this was taken after we had a complete MOT (as opposed to nearly trapped molecules by MOT-like forces) and each slowing laser frequency scanned as a function of MOT number.

We put together a spreadsheet that theoretically calculates the ideal center frequency for each slowing laser, based on spectroscopy of each repump transition and the measured broadening of each

Table 2.1: Comparison of extrapolated and adjusted laser frequencies. The first six columns are in MHz (only the last four digits shown). Wavelength is in nm. The last three columns are in m/s. See main text for details.

Laser	(1) Freq.	(2) Lower res.	(3) Upper res.	(4) EOM width	(5) Broad. low freq.	(6) Broad. high freq.	(7) Wavelength	(8) Addr. high v	(9) Addr. low v	(10) v span
Extrapolated frequencies (retrieved from laboratory notes on 2023/11/16)										
main	8147	8078	8187	455	7919.5	8374.5	688	109	-129	238
(100)	1650	1751	1860	388	1456	1844	631	186	10	176
(200)	8800	8738	8847	348	8626	8974	630	71	-80	151
(010);N=2	9050	8875	8875	469	8815.5	9284.5	675	40	-276	317
(110);N=1	0550	550	660	320	390	710	624	100	-31	131
(010);N=1	4350	4245	4348	312	4194	4506	624	32	-99	130
(02^{0}0)	7050	7073	7183	462	6819	7281	638	162	-63	225
(02^{2}0)	8950	8945	8945	334	8783	9117	697	113	-120	233
(300)	0550	548	655	317	391.5	708.5	711	111	-38	149
Adjusted frequencies (retrieved from laboratory notes on 2023/11/29)										
main	8145	8078	8187	455	7917.5	8372.5	688	110	-128	238
(100)	1700	1751	1860	388	1506	1894	631	155	-21	176
(200)	8750	8738	8847	348	8576	8924	630	102	-49	151
(010);N=2	8950	8875	8875	469	8715.5	9184.5	675	108	-209	317
(110);N=1	0550	550	660	320	390	710	624	100	-31	131
(010);N=1	4300	4245	4348	312	4144	4456	624	63	-67	130
(02^{0}0)	7050	7073	7183	462	6819	7281	638	162	-63	225
(02^{2}0)	8950	8945	8945	334	8783	9117	697	113	-120	233
(300)	0550	548	655	317	391.5	708.5	711	111	-38	149

white-light EOM. Table 2.1 shows how the calculation was done. The first column shows the set frequencies of each laser. Only the last four digits of each laser frequency (in MHz) are shown for simplicity. For example, a laser frequency of 435968102 MHz is shown as 8102. The next two columns (2 and 3) show the two spin-rotation (SR) transition frequencies, measured during fine spectroscopy. When there is only one SR component to repump (e.g., the $N = 2$ states), the same frequency appears in both columns. The frequency shift due to switching AOMs (typically 80 MHz) is taken into account. Column 4 lists the white-light broadening range (in MHz), measured experimentally using a transfer cavity. Columns 5 and 6 show the calculated frequency range covered by the white-light broadened laser. Column 8 shows the maximum velocity addressed by the laser, derived from the comparison of columns 2 and 5. Similarly, column 9 shows the minimum velocity addressed, derived from columns 3 and 6. A negative value here implies that the laser can even address molecules moving in the same direction, confirming that the "0 m/s velocity class" is addressed. The wavelength data in column 7 was used to convert detunings to velocities. Finally, column 10 shows the span of addressable velocities for each EOM broadening.

From this table, we see that some of the frequencies are on the edge of being able to address all desired velocity classes. The (100) repump appears to barely address the slowest velocity classes near the end of the slowing process. In contrast, the (200), (010); $N = 2$, and (010); $N = 1$ repumps seem to miss molecules in the $\sim$ 100 m/s velocity class at the beginning of the slowing.

As shown in Fig. 2.6, we saw immediate increase in slowed molecule signal as we modified the frequencies according to this calcuation. We first updated the (100) repump frequency, which appeared most important among the frequencies that were calculated to be suboptimal. After this showed improvement, we updated other frequencies that were suboptimal according to our model. After other improvements, explained later, we were able to achieve a MOT to perform good frequency scans on. The MOT number scans as functions of the repump frequencies of the (100), (010); $N = 1$ and (010); $N = 2$ lasers are shown in Fig. 2.8. These scans were done after fully optimizing the MOT, after increasing the MOT beam diameters from $d = 1$ cm to $d = 2$ cm, which have a higher capture velocity than the initial MOT (i.e., it allows for more headroom in tuning the repump frequencies to the lower frequency side). We see that indeed the laser frequencies we calculated to be suboptimal lie on the edge of sharp cutoffs in the resulting MOT number. In particular, we were operating around a critical cutoff for the (100) repump laser frequency, which explains the improvement by fixing only the (100) repump frequency in Fig. 2.6. We also performed a scan of the main line slowing laser (after obtaining a separate main line laser for the MOT), in the $d = 2$ cm MOT. As the calculations suggested, the safeguard broadedning of the main line from 300 MHz to 450 MHz was necessary for efficient slowing, as the laser cooling frequency lies on the very edge of the range of effective slowing frequencies even after broading the EOM to 450 MHz, as shown in Fig. 2.7.

The main line (and the lasers sharing the same EOM: (010); $N = 2$ and (02^20)) was initially broadened to $\sim$ 450 MHz to cover both extrapolated and calculated frequency ranges. This is why it seems to address molecules on the very slow side (rather than centered in the calculated optimal

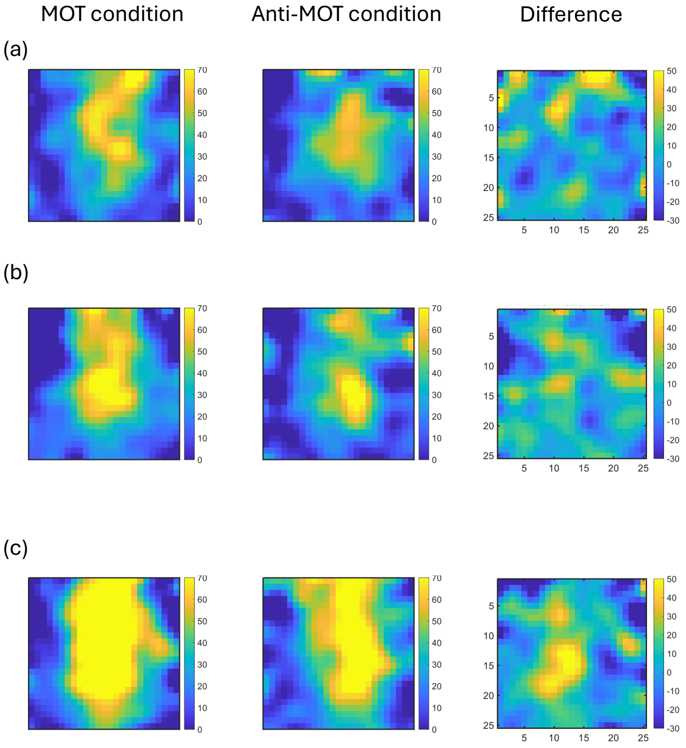

Same data as right above, plotted on a non-saturated color scale

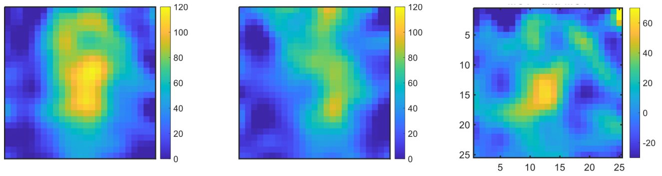

Figure 2.6: Slowed molecular signal ("MOT-like forces") before and after fixing the repump laser frequencies. From left to right is the "MOT condition" (light polarization switching in phase with the B-field), "anti-MOT condition" (light polarization switching out of phase with the B-field), and the difference . **(a)**: Using frequencies extrapolated from optimal frequencies slowing to 25 m/s and to 50 m/s. **(b)**: Just changing the (100) repump laser to the frequency based on calculations. All other lasers were the same as (a). **(c)**: All lasers switched to calculated optimal frequencies. All three datasets were taken consecutively (in the order of (a)→(b)→(c)), without changing the ablation spot (thus minimizing ablation fluctuations). Each dataset was averaged over approximately five minutes. The first three rows use the same color scale for comparison. The last row is the same data as the third row, but plotted using a more reasonable color scale.

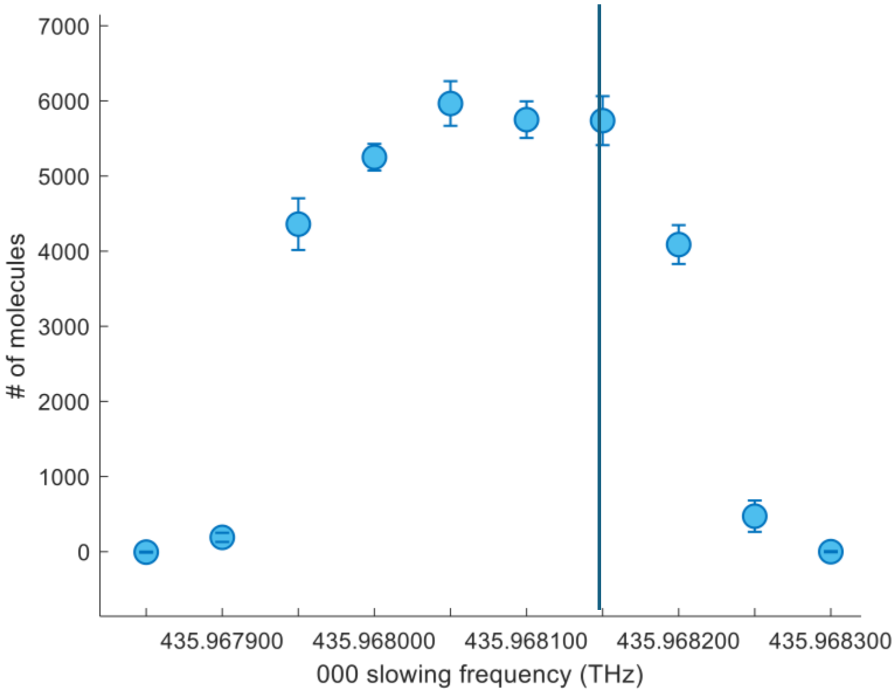

Figure 2.7: Frequency scans of the mian line laser in the d=2cm MOT. This data was taken after the MOT diameter was expanded from $d = 1$ cm to $d = 2$ cm (see Section 2.3.8). All other laser frequencies were kept at optimal while scanning the main line laser. The vertical line denotes the main line frequency. This data was taken with the main line white-light EOM broadening kept at 450 MHz, guided by the calculations, instead of the initially planned 300 MHz (see main text). Without this safeguard, the plateau region where the laser cooling is effective would have effectively shrunk by $\sim\ 150$ MHz, or ~ 75 MHz on each side, which would have made the laser slowing much more inefficient.

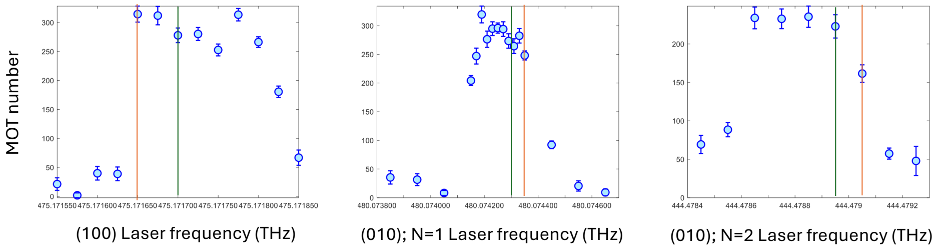

Figure 2.8: Frequency scans of repump lasers in the MOT. This data was taken after the MOT diameter was expanded from $d = 1$ cm to $d = 2$ cm (see Section 2.3.8). All other laser frequencies were kept at optimal while scanning each laser. The orange vertical line denotes the extrapolated frequency, and the green line denotes the frequency modified guided by calculations. We see that the calculation is effective in pointing out the repump frequencies that are around a cutoff for the resulting MOT number. This data was taken with the $(010); N = 2$ white-light EOM broadening kept at 450 MHz, instead of the initially planned 300 MHz (see main text). Without this safeguard, the orange line would have effectively shifted $(450 - 300)/2 = 75$ MHz even more to the right.

frequency range) in Table 2.1. Although unintentional, this initial investment ultimately played a key role in keeping the $(010); N = 2$ repump frequency in the effective range. As shown in Fig. 2.8, the $(010); N = 2$ laser was already set to too high a frequency, placing it midway on a slope of the MOT number decrease. If we had not broadened this frequency along with the main line frequency to 450 MHz instead of 300 MHz, the lowest frequency it could have hit was $(450 - 300)/2 = 75$ MHz higher, which would have shifted it entirely above the slope to a frequency range that does not address any effective slowing.

2.3 MAGNETO-OPTICAL TRAPPING

2.3.1 INTRODUCTION TO RF MOTS

A crucial step towards directly laser-cooled molecules is trapping them in a MOT. We first review why we use an RF MOT and how it works. When cycling photons on molecules, we use type-II transitions, i.e., transitions that have more magnetic sublevels in the ground state than in the excited state, because it is required to have larger angular momentum in the ground state to maintain rotational closure[55]. Thus, with a single polarization light in a constant magnetic field, magnetic dark states are unavoidable.

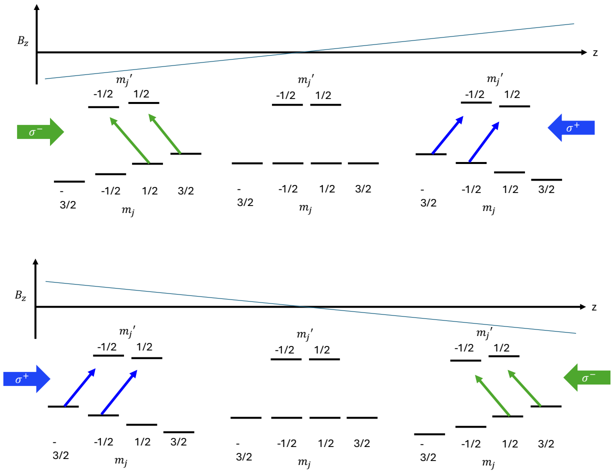

Figure 2.9: Diagram showing the mechanism of magnetic dark states being remixed in an RF MOT, in the case of a J'$= 1/2 \leftarrow$J"$= 3/2$ transition.

One way to remix these magnetic dark states is to switch both the light polarization and the magnetic field direction in the time domain[5]. The remixing frequency should be on the order of or larger than the single-photon scattering rate so that it does not limit the scattering rate. Figure 2.9 depicts the mechanism of the dark state remixing. In this method, every molecule that is bright to the light experiences a net force towards the center of the MOT, thus trapping occurs. Since the MOT beams are red-detuned, there is also Doppler cooling at the center of the MOT, where the B-field is low and the Zeeman shifts are minimized. In the SrOH MOT, we use a detuning of about $1\Gamma \approx 7$ MHz (see Fig. 2.10).

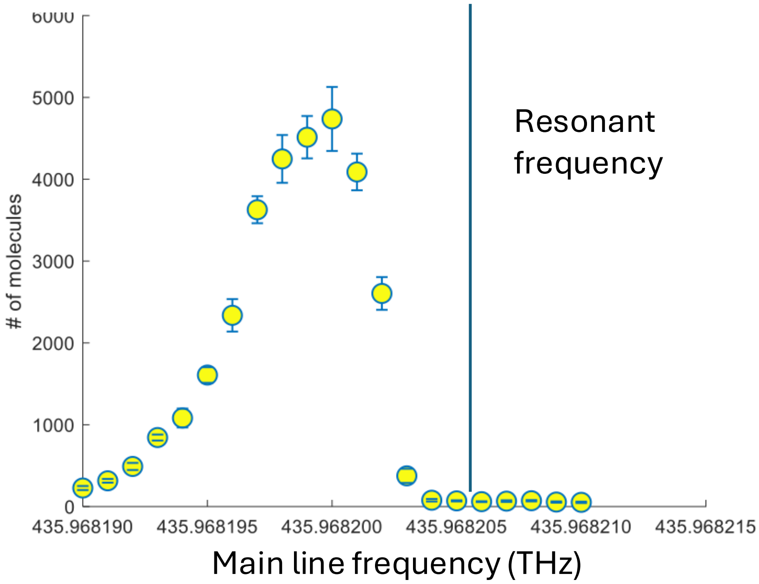

Figure 2.10: MOT number as a fucntion of the main line laser frequency.

2.3.2 Optical setup

Our main line laser (initially we split off from the slowing main line laser, and later we purchased a separate laser for just the MOT) goes through an optics breadboard that handles frequency, intensity, and polarization switching. The overview of this board is shown in Fig. 2.11.

First, the beam is sent through a double-pass AOD, whose frequency and driving power are controlled by a voltage-controlled oscillator (VCO) (Mini-Circuits ZOS150) and a voltage-variable attenuator (VVA) (Mini-Circuits ZX73-2500-S+), respectively. These frequency and power controls were not only useful for initial scans of the MOT parameters, but also played an important role when shifting frequencies and powers for sub-Doppler cooling, explained in the next chapter.

Next, the beam goes through a Pockels cell, driven by a square wave at 1.4 MHz. We purchased Model 350-210-01-RP KD*P EOM and Model 25D Driver from Conoptics. Note that no polarization cleanup elements (such as PBSs) can be placed after the Pockels cell, since the light must switch

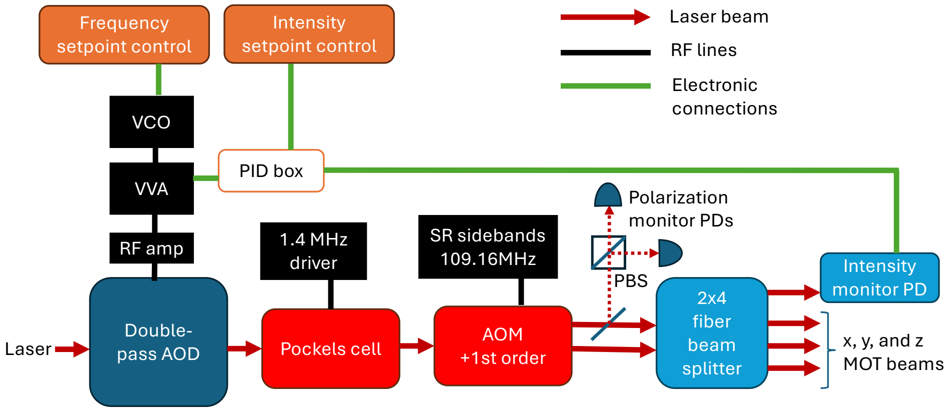

Figure 2.11: AOD board setup.

between two opposite polarizations.

Then the beams are fiber-coupled to an AOM to split into 110 MHz sidebands. Each SR sideband is then passed through a half-wave plate (HWP) to produce opposite polarizations. A pickoff is added in one of the arms to monitor polarization. The picked-off light is passed through a PBS, and the vertical and horizontal polarization components are monitored on a photodiode. See the later section for how the phase of the light polarization switching was synchronized with the magnetic field switching.

The light then goes into a 2x4 fiber beam splitter (later replaced by a 4x4 splitter, explained in the sub-Doppler cooling section - this was a custom-made order from Evanescent Optics Inc.), where the two inputs accept each of the SR components and equally split them into four outputs. Three outputs are used for the x, y, and z MOT beams, and the fourth output is sent to a photodiode to monitor power. The power monitor signal is fed back into the VVA controlling the AOD, stabilizing MOT beam power and allowing precise external control.

(Here are the specifications of the 4x4 splitter: 4x4 splice-less PM coupler array, wavelength 687.5nm, ratio tolerance per individual coupler +/- 4%, excess loss per input <0.3dB (excluding connectors), output PER <-19dB, Corning PM63-U25D fiber, pigtail lengths 5m, pigtails sleeved with 3mm OD sleeving, FC/APC connectors on all ports (keyed to slow axis), housed in aluminum enclosure 4" x 3.5" x 0.5")

Immediately after the three outputs of the 2x4 splitter, the light passes through quarter-wave plates (QWPs) to convert linear to circular polarization. When the linear polarization is switched, the resulting circular polarization switches as well.

2.3.3 How to build the coils

We ordered coil plates to be made by Remtec. The coils are gold-plated copper printed on a ceramic base. The coils are designed such that, when driven in an anti-Helmholtz configuration separated by 1", the magnetic-field gradient is 4 G/cm per 1 A of current.

Next, the coils are mounted to the top flange of the MOT chamber. The top flange, manufactured by Ancorp, which has the same dimensions as CF800XCF275X6CF133T-MCF, but is made of titanium and the mini-CF ports are machined onto the face of the 8" flange instead of welding on separate flanges. The MOT chamber is a stainless steel chamber, blackened internally with MH2200 spray paint. Four 3/8" vacuum feedthroughs descend from the top flange to mechanically and thermally attach the top coil. Two of the external rods are water-cooled. The bottom coil is attached to the top coil using custom-made 101 copper rods (1.00" long, 3/8" diameter) with vent holes.

We also used a four-pin electrical feedthrough EFT0543052 from Lesker for the driving current. All connections were made using lug connectors and push-in sockets, avoiding the need for soldering inside the vacuum.

We then blackened the chamber using UHV-compatible spray paint MH2200. The painting was done using a Thorlabs airbrush and a high-pressure nitrogen bottle. The CF flange knife-edge was protected by a copper gasket, and areas not to be painted were masked with Kapton tape.

After blackening, the coils, flange, and mounts were baked at 100°C overnight in a vacuum oven.

2.3.4 How to drive the coils

The coils were driven by a resonant LC circuit (tank circuit) to enable efficient power transfer from the RF amplifiers. We generated sine waves using a Rigol function generator, amplified by ENI 550L 50W ”big blue” RF amplifiers. The RF current entered the tank circuit box, where impedance matching was performed in two steps: first, matching the real part of the impedance using a transformer with a 1:4 winding ratio; and second, matching the imaginary part using a tunable capacitor in series with a MOT coil. We used a capacitor (Comet CVUN-1500AC/3-JHJA-Z) tunable between 150 pF and 1500 pF, suitable for matching an inductance of 30 μH at 1.4 MHz. Each coil has an individually tunable circuit, which is important because the LC resonance shifts due to mutual inductance. The current at each input is monitored by a current probe (Tektronix CT2 - AC Current Probe), which converts the measured current into a voltage signal at a rate of 1 V/A.

2.3.5 How to set the phase between the coils and the switching light polarization

We now have a way to switch both MOT light polarization and magnetic field gradient at RF frequencies. We also monitor both the light polarization (before conversion to circular) and the coil current.

For proper RF MOT operation, these must be synchronized. That is, when the MOT beam is in a particular polarization, the B-field gradient must point in the same direction and not flip before the polarization changes. Therefore, it is important to match the delays from the MOT chamber to the scope for both signals.

The first step is to use BNC cables of equal length between each monitor point and the scope. Initially, we tried to align the phases by simply watching the scope, but overlooked an additional delay.

As mentioned earlier, polarization is measured just before the 2x4 splitter. However, the light travels through 25 m of fiber before reaching the MOT chamber. Due to the fiber material, the effective distance is closer to 30 m. This introduces a 100 ns delay. Since the MOT switches at 1.4 MHz (cycle period 700 ns), a 175 ns mismatch would be a quarter-cycle out of phase—enough to disrupt the MOT.

To compensate, we matched the phase using the polarization just before the QWP at the MOT chamber. We then reconnected the original polarization monitor and recorded the apparent phase difference. Whenever we perform phase matching, we refer to this calibrated offset. Once we had a MOT with reasonable signal, we performed a phase scan, shown in Fig. 2.12. It shows the MOT signal approaching zero with phases $\sim$ 45 degrees away from optimal.

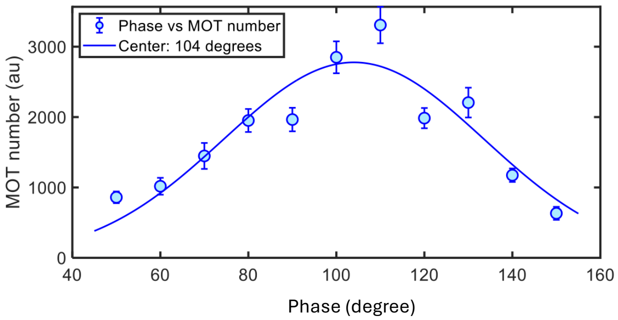

Figure 2.12: Scan of the phase between the RF current in the MOT coils and the polarization of the MOT beams.

2.3.6 IMAGING SYSTEM

The imaging system consists of four lenses. Starting closest to the molecules, the first lens is an in-vacuum achromatic lens with a focal length of $f = 50$ mm and diameter $\varnothing = 1$”. This lens is mounted on the MOT coil boards in a PEEK plastic holder, positioned 50 mm from the center of the coils where the MOT forms. This lens collimates the fluorescence from the MOT for the rest of the imaging system outside the vacuum. The next lens is a $f = 75$ mm achromatic lens of diameter $\varnothing = 2$”, which focuses the fluorescence. Near the focus, a Uniblitz mechanical shutter is installed to block or pass the fluorescence onto the camera. We then allow the light to expand again. The next lens is a

$f = 150$ mm achromatic lens of diameter $\varnothing = 2$" placed 225 mm (75 + 150 mm) from the $f = 75$ mm lens. This $f = 150$ mm lens collimates the light again, which is then focused by a $f = 80$ mm lens of diameter $\varnothing = 2$" onto the EMCCD camera. The total magnification of the system is:

$$\frac{75\text{ mm}\cdot 80\text{ mm}}{50\text{ mm}\cdot 150\text{ mm}} = 0.8 \tag{2.5}$$

An alternative way to understand this system is that a 2× telescope formed by the $f = 75$ mm and $f = 150$ mm lenses is inserted in the Fourier plane of the $f = 50$ mm objective lens and $f = 80$ mm ocular lens. The $f = 50$ mm and $f = 80$ mm lenses form a microscope with magnification 1.6, and the 2× telescope expands the collimated light, resulting in a focused image that is reduced by a factor of two due to conservation of étendue. Thus, the overall magnification is 0.8.

The reason we designed the imaging system to have a relatively small magnification (in fact, under 1) relates to the size and pixel resolution of the EMCCD camera. The active area of the EMCCD camera is 8 mm × 8 mm with 500 × 500 pixels, so each pixel is 16 μm in size. With an overall magnification of 0.8, the imaging region becomes 10 mm × 10 mm, and each pixel images 20 μm × 20 μm in the object plane. This 10 mm field of view is ideal for continuously imaging the molecules during time-of-flight measurements, while still providing the resolution necessary to image conveyor belt MOTs and optical traps with features on the order of tens of μm.

2.3.7 INITIAL TRAPPING

In this subsection, we describe our initial MOT signal and its characterization. Detailed information can be found in the thesis of Alexander Frenett. It turned out that most of the molecules in our initial MOT were short-lived (under 10 ms), and we were not able to increase the apparent lifetime above $\sim$ 20 ms until we expanded the MOT beam size from a diameter of $d = 1$ cm to $d = 2$ cm. The reason for this limited lifetime is explained in the "Understanding the loading rate" section.

Using spectroscopy results from 2020[42], we identified a repumping scheme capable of cycling more than 10,000 photons on SrOH using 10 different lasers. Note that this spectroscopy was done in a separate setup, where we directly observed light-induced fluorescence from a molecular beam on a spectrometer.

With this scheme, we observed the first signatures of MOT formation. However, improvements were needed in the repump laser powers. Many repumps were power-starved, and the MOT fluorescence signal was linearly proportional to the repump power. Most issues were resolved by redistributing power among the SFG systems as needed. Notably, the $\tilde{X}^2\Sigma^+(02^20)$–$\tilde{A}^2\Pi_{1/2}(100)$ repump pathway was replaced with the $\tilde{X}^2\Sigma^+(02^20)$–$\tilde{A}^2\Pi_{1/2}(02^00)$ pathway, which provided a higher scattering rate at the same power. A power scan is shown in Fig. 2.13, where MOT fluorescence is plotted as a function of the repump laser power for each of the $\tilde{X}^2\Sigma^+(02^20)$ repump pathways. With these changes, we implemented the laser cooling scheme illustrated in Fig. 2.14.

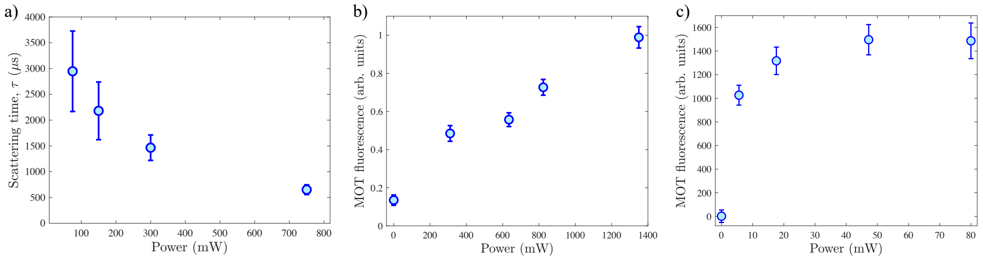

Figure 2.13: Single-photon scattering time and MOT signal as a function of $\tilde{X}^2\Sigma^+(02^20)$ repumping laser power. Subfigures (a) and (b) show power scans for the $\tilde{X}^2\Sigma^+(02^20)$-$\tilde{A}^2\Pi_{1/2}(100)$ transition, and subfigure (c) was taken for $\tilde{X}^2\Sigma^+(02^20)$-$A\mu^2\Pi_{1/2}(020)$. The repumper through $\tilde{A}^2\Pi_{1/2}(100)$ in subfigure (a) only achieves a repumping time of 500 μs at 750 mW. Limitations are also evident in (b), where even 1.35 W (the highest power available) does not saturate the MOT fluorescence. After switching to $\tilde{X}^2\Sigma^+(02^20)$ through $A\mu^2\Pi_{1/2}(020)$, MOT fluorescence was saturated with just 40 mW. Retrieved from Ref.[43].

2.3.8 INCREASING THE MOT BEAM DIAMETER

Increasing the MOT beam diameters from $d = 1$ cm to $d = 2$ cm was critical for capturing more molecules and holding them for longer durations. The improvement allowed for increased deceler-

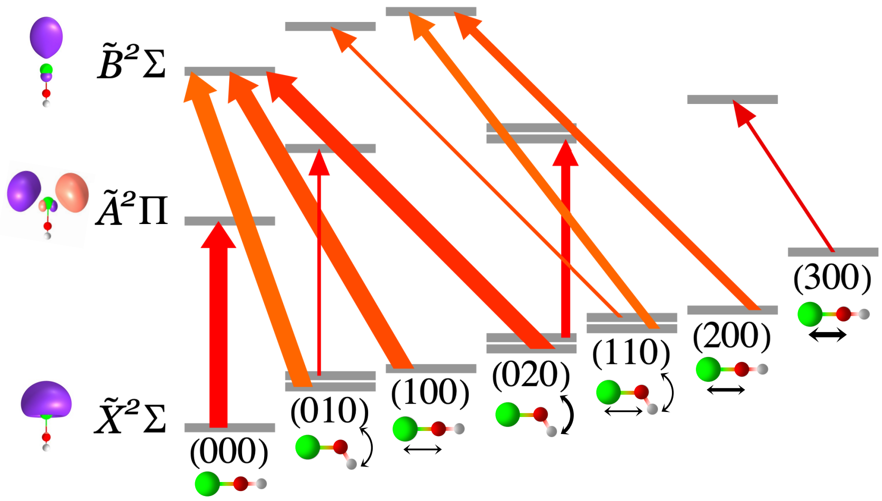

Figure 2.14: Laser cooling scheme. Vertical position depicts total vibronic energy, up to a fixed overall offset in the A and B energies. Separations between $N = 1$ and $N = 2$ states within (010) and (110), and between $\ell = 0$ and $|\ell| = 2$ manifolds of (020), are amplified for clarity. Thin, medium, and thick lines denote slowing lasers with < 10 mW, < 100 mW, and < 1 W, respectively. Illustrations on the left depict the valence orbitals in each electronic state. Retrieved from Ref.[43].

ation distance within the MOT, resulting in higher capture velocities. To first order, to match the capture velocity of the CaOH MOT, which used $d = 1$ cm beams[56], the SrOH MOT—being about twice as massive—would require $d = 2$ cm. Fig. 2.15 compares images of the MOT for the two beam diameters.

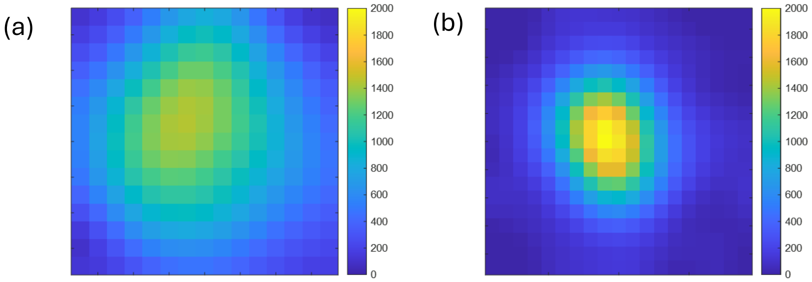

Figure 2.15: Images of the MOT with beam diameter (a) $d = 1$ cm, and (b) $d = 2$ cm.

When the diameter was $d = 1$ cm, most of the MOT signal originated from molecules fluorescing for only a few milliseconds, suggesting they were "nearly-trapped"—i.e., they left the MOT before completing a full oscillation. Increasing the MOT beam diameters converted these nearly-trapped molecules into fully trapped ones. See Section 2.4 for further details.

2.3.9 CHARACTERIZATION OF THE SROH MOT

With the improvements above, we observed a MOT with lifetimes up to approximately 100 ms., as shown in Fig. 2.16. The main limitation arises from decays to vibrational levels that are not repumped. This is consistent with Figure 2.16 (a), where the MOT lifetime increases as beam power is reduced. The MOT temperature was measured to be $\sim$1 mK and the MOT size $\sim$1 mm—typical values for a molecular MOT. We also observed oscillations in the MOT when molecules were displaced using the slowing beams. The displacement was achieved by applying the slowing lasers for a fixed duration. Initially, we applied them for 0.5–0.7 ms, which worked for MOTs with relatively high-power beams (over 4 mW per beam). However, for MOTs with lower beam power (and therefore weaker restoring forces), the kick imparted too high an initial velocity to the molecules, allowing them to escape the MOT before oscillating back. Therefore, we divided the kick into two steps of 0.3 ms, with a 3 ms wait in between (the MOT remained on throughout). The intent was to reset the velocity accumulated during the first kick by allowing the MOT forces to decelerate the molecules, while still achieving a measurable displacement from the MOT center.

2.3.10 CHIRPED SLOWING

One technique that improved the MOT number by a factor of 2–3 is chirped slowing (see Fig. 2.18). The general idea is that instead of white-light broadening the slowing light, we chirp the frequency of a slowing laser over time so that it remains resonant with molecules experiencing different Doppler shifts at different moments. In our case, we chirped the (100) repump laser. The initial motivation for chirping this laser was because it was technically easier to implement than chirping the main line

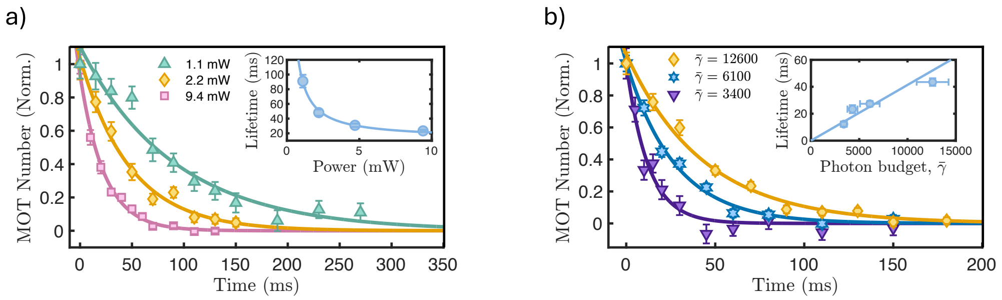

Figure 2.16: Lifetime measurements. Fluorescence over time and extracted lifetimes. Errorbars denote 1σ uncertainty. Insets show fitted lifetimes. (a): Dependence on power per MOT beam (b): Dependence on photon budget. Retrieved from Ref.[43].

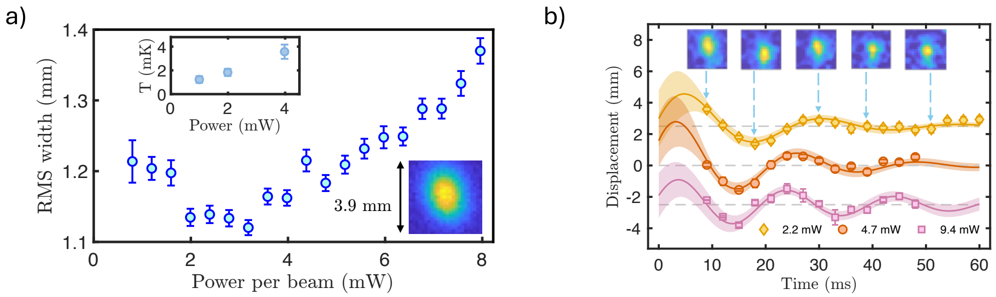

Figure 2.17: (a) Molecule cloud size and temperature. Geometric mean RMS cloud size σ_0 and temperature T as a function of power in each MOT beam. Minimum size: 1.12(1) mm; minimum temperature: 1.2(3) mK at 1.1 mW per beam. (b) Trapped molecule oscillations. Top: Images at 2.2 mW per beam at several delays post-displacement. Bottom: MOT cloud position vs. time after displacement by slowing laser, at various MOT beam powers (offset for clarity). Retrieved from Ref.[43].

slowing laser, which was also used for the MOT beams at the time. However, we later discovered that the (100) laser was power-starved (see Fig. 2.20), and chirping it allowed us to deliver more power per frequency band over the natural linewidth. The two SR sidebands were addressed separately with a 110 MHz AOM.

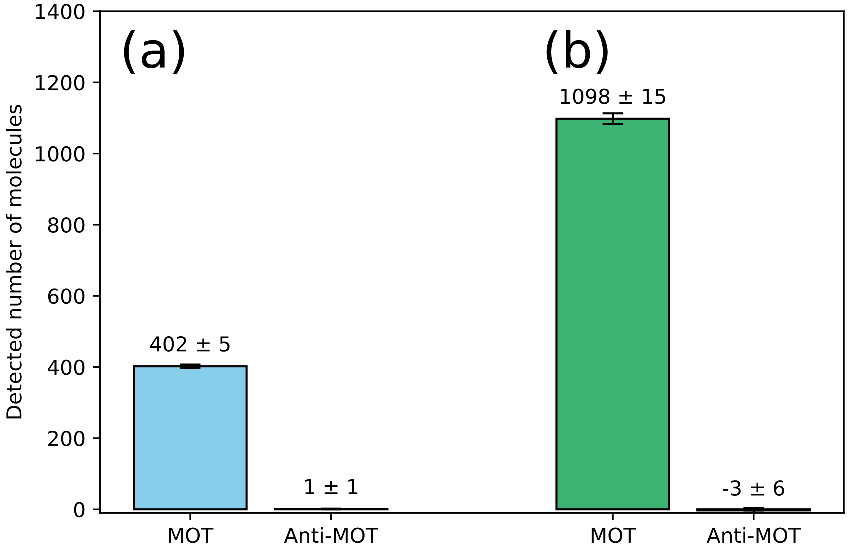

Figure 2.18: Comparison of the best number measurement (a) before implementing chirped slowing and (b) after implementing chirped slowing. The anti-MOT condition is also shown in each measurement. The MOT numbers plotted here are not corrected for the finite imaging time or the extended loading factor (see Section 2.4). Both datasets had the same imaging time of 50 ms. Both were taken within a week of each other, as chirped slowing was the only significant change implemented during this period. Data in (b) was used to calculate our peak MOT number of $2000(600)$ in Ref.[43]. Note the MOT beam diameters were already boradeded to $d = 2$ cm before this data was taken.

The setup for chirped slowing is shown in Figure 2.19, where a sample-and-hold chip (LF398) is used to hold the feedback voltage and add chirp voltage through an op-amp. We chirped the laser frequency by applying a voltage ramp to the current controller of the 1064 nm seed of the (100) repump laser.

On the laser locking software, an ”ignore jump” feature was added to improve laser stability. This feature made the locking software ignore frequency jumps outside a certain range and not attempt to

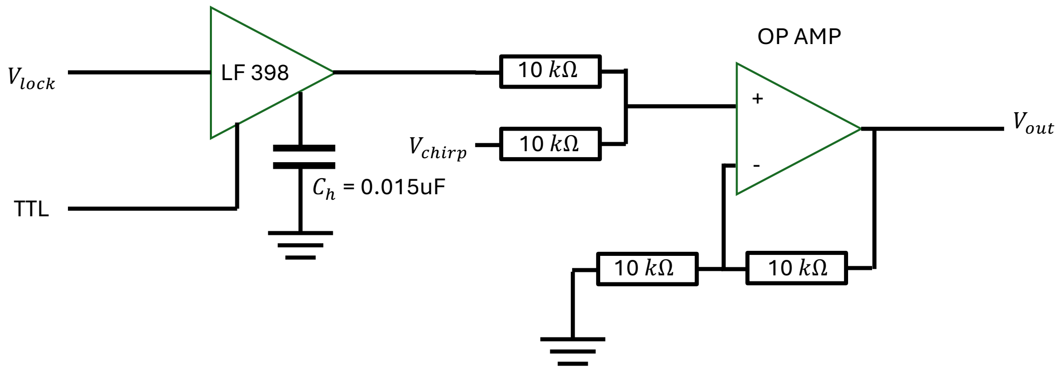

Figure 2.19: Circuit diagram for the chirped slowing voltage adder.

lock the laser during those excursions.

Since we jump more than 100 MHz during the chirp, it is essential to avoid adding feedback voltage during this time. This is achieved with the sample-and-hold chip in the feedback circuit. It is also important to "trick" the locking software into not outputting unnecessary feedback during slowing (even though it is not applied), to prevent overshoot when the chirp ends.

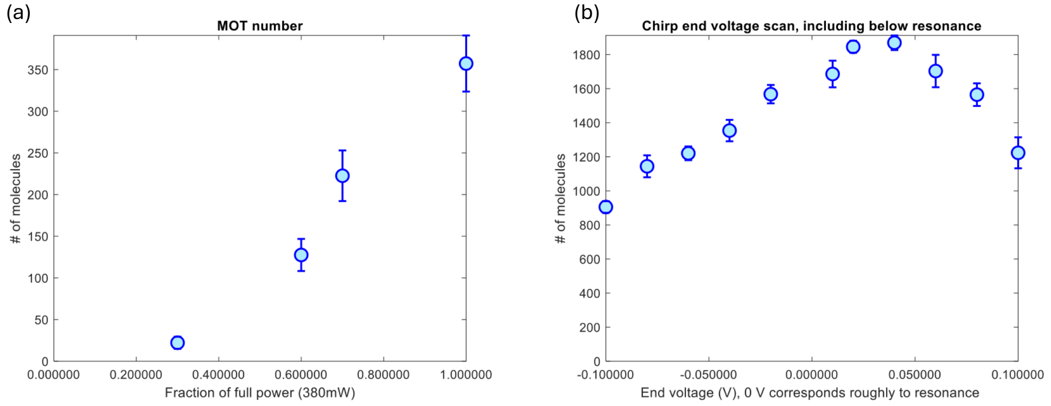

Full power here was before fiber coupling the chirped light path with a PCF.

Higher voltage corresponds to lower frequency, addressing higher velocities.
0.1V corresponds to ~10MHz.

Figure 2.20: Chirped slowing dependence on power and end frequency.

We also scanned the power and end frequency of the (100) chirped slowing laser, as shown in Fig. 2.20. As shown in the power scan, the (100) laser followed a linear trend up to the maximum powers we tested. Initially, we expected ∼400 mW to be sufficient, given that the white-light slowing used $\sim$ 2 W, broadened over about 40Γ. However, to our surprise, the chirped laser remained power-starved. We replaced a regular PM fiber with a PCF in the chirp path, allowing us to transmit 1.4 W in total. This configuration was used for the final MOT number measurement in Ref.[43].

From the end-frequency scan, we found that the optimal frequency occurred a few MHz below resonance. The MOT number decreased in both directions from this point. The decrease in MOT number with lower chirp end frequency is consistent with molecules not being slowed enough to be captured. Conversely, the MOT number also decreased slightly as the chirp end frequency increased, suggesting that having a cutoff velocity may help improve MOT loading.

2.4 Understanding the loading rate

We have observed, consistent with observations reported in[59], that the magneto-optical trap (MOT) of SrOH is loaded from the cryogenic buffer gas beam (CBGB) over an extended time of ∼30 ms, with both chirped-frequency and white-light slowing.

This timescale is not problematic for well-optimized MOTs with relatively long lifetimes, since additional experimental procedures can be conducted after the MOT fully loads. However, for MOTs with short lifetimes or MOT-like forces that decelerate but do not fully capture molecules (nearly-captured molecules), this delay leads to a misinterpretation: the observed fluorescence decay may not reflect the actual MOT lifetime.

Here we present a simple model that explains the fluorescence signal evolution for MOTs loaded from CBGBs. The model captures both long- and short-lived MOT behavior in a single equation. It shows that the fluorescence transition smoothly shifts between limits, although the decay at later times is dominated by different physical timescales in each case. We also propose a diagnostic to distinguish between true long-lifetime MOTs and cases where MOT-like forces produce a seemingly long decay that is actually dominated by the molecular beam.

2.4.1 OBSERVATION OF LATE-ARRIVING MOLECULES

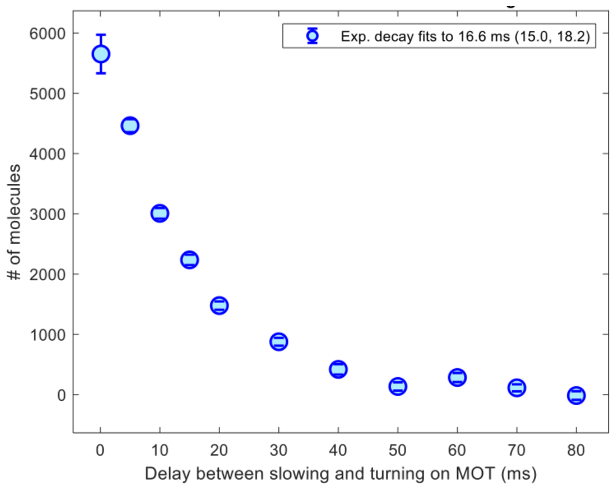

Figure 2.21: Turning on the SrOH MOT after waiting various times after the slowing ends. The signal is a good representation of the number of molecules in the molecular beam that are under the capture velocity of the MOT. This also fits well to an exponential decay, with $\tau = 16.6(8)$ ms. We later discuss an alternative method to determine the decay time.

As shown in Fig. 2.21, the SrOH arrival time after slowing fits well to an exponential decay. We confirmed this using two different methods. First, we simply imaged the molecular beam after the slowing ends, which represents the total number of molecules arriving at each time after slowing ends. Second, we turned on the MOT after various wait times after the slowing ends, which is a better representation of molecules that are under the capture velocity of the MOT. In both experiments, the population arrival after turning off the slowing fits well to exponential decays. Cutting off the molecules exiting the beam box with an ultrahigh vacuum (UHV) shutter after a certain time also helps this decay fit better to an exponential.

2.4.2 Construction of the model

For simplicity, let us model the number of molecules arriving after slowing ends as an exponential decay, which is a good approximation as shown in Section 2.4.1. For an arbitrary distribution of arrival, the model can be generalized using the exact same steps shown below.

Then we can write the number in the beam $N_{beam}(t)$ as

$$N_{beam}(t) = N_0 e^{-t/\tau_b} \tag{2.6}$$

where $t = 0$ denotes the end of the slowing. Unless otherwise noted, we will also assume the MOT loading happens at $t = 0$. A more general case is discussed later. τ_b denotes the decay time for the molecular beam.

We can now show that the number of molecules in a MOT is the convolution of two exponentials, which results in a difference of two exponentials.

Assume a constant loading rate of molecules from the molecular beam to the MOT, which we denote r. The number of molecules newly loaded into the MOT per unit time at a certain time $\dot{N}_{load}(t)$ is

$$\dot{N}_{load}(t) = rN_{beam}(t) = rN_0 e^{-t/\tau_b} \tag{2.7}$$

If the MOT lifetime is τ_M, then the number of molecules (per unit time) that were loaded at time $t = t_1$ which survives at time $t(> t_1)$ can be described as

$$\begin{aligned} \dot{N}_{survive}(t_1) &= \dot{N}_{load}(t_1) e^{-(t-t_1)/\tau_M} \\ &= rN_0 e^{-t_1/\tau_b} e^{-(t-t_1)/\tau_M} \end{aligned} \tag{2.8}$$

Therefore, the total MOT number at time t is

$$\begin{aligned} N_{MOT}(t) &= \int_0^t \dot{N}_{survive}(t_1)\, dt_1 \\ &= \int_0^t rN_0 e^{-t_1/\tau_b} e^{-(t-t_1)/\tau_M}\, dt_1 \end{aligned} \tag{2.9}$$

which describes a convolution of two exponential functions with decay times τ_b and τ_M, respectively.

Solving this integral,

$$\begin{aligned} N_{MOT}(t) &= rN_0 e^{-t/\tau_M} \int_0^t e^{-t_1(1/\tau_M - 1/\tau_b)}\, dt_1 \\ &= \frac{rN_0}{1/\tau_M - 1/\tau_b} e^{-t/\tau_M}\left[e^{-t(1/\tau_M - 1/\tau_b)} - 1\right] \\ &= \frac{rN_0}{1/\tau_M - 1/\tau_b}\left(e^{-t/\tau_b} - e^{-t/\tau_M}\right) \end{aligned} \tag{2.10}$$

Note this quantity is always positive because $(1/\tau_M - 1/\tau_b)$ and $(e^{-t/\tau_b} - e^{-t/\tau_M})$ have the same sign, regardless of τ_M or τ_b being larger.

Another point to note is that the two exponential decays have the same amplitudes in this model. This is because we are assuming there are zero molecules loaded at time $t = 0$, i.e., $N_{MOT}(t = 0) = 0$. In general, there can be different amplitudes for each exponential decay if the MOT already has some molecules loaded at $t = 0$.

If $\tau_M = \tau_b$, it is obvious from Equation 2.9 that the result is

$$N_{MOT}(t) = rN_0 t e^{-t/\tau_M} \tag{2.11}$$

The general shape of $N_{MOT}(t)$ is shown in Fig. 2.22. Different values of τ_M are plotted for $\tau_b = 10$

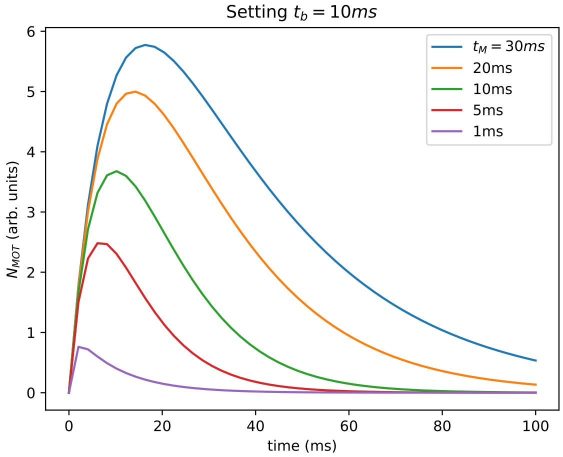

Figure 2.22: Plotting $N_{MOT}(t)$ described in Equation 2.10. Plotted for different τ_M, while fixing $\tau_b = 10$ ms. The behavior is similar for both $\tau_M > \tau_b$ and $\tau_M < \tau_b$.

ms. We see that the shape of the transitions smoothly changes from a rise time of τ_b and decay time of τ_M in the $\tau_M > \tau_b$ case, to a rise time of τ_M and decay time of τ_b in the $\tau_M < \tau_b$ case. As discussed in Section 2.4.3, this makes it hard to distinguish the MOT lifetime from the beam decay time when the MOT lifetime is smaller than the beam decay time.

The simple physical explanation of the shape of this graph is the following: In the case of $\tau_M > \tau_b$, a significant fraction of the molecules that were loaded at $t = 0$ survive after the beam decay time. Therefore, within the timescale of τ_b, the MOT signal keeps increasing as more molecules are loaded in and the MOT is not losing as many molecules. After the beam dies out, the MOT signal just decays with the MOT lifetime τ_M.

In the case of $\tau_b > \tau_M$, the MOT signal size is mostly proportional to the beam signal size, since the molecules held in the MOT are the ones just loaded within a short time compared to the beam decay time. Therefore, at later times, it simply decays on the same timescale as the beam decay time τ_b. At the beginning, the MOT signal rises with a timescale on the order of the MOT lifetime because the molecules keep accumulating for that amount of time before reaching a steady decay.

In the SrOH MOT experiment, the MOT beams are also turned on during slowing, so the MOT signal at $t = 0$ starts out at some finite value. Therefore, we can fit our MOT signal to a general form of a difference of two exponentials.

$$N_{MOT}(t) = ae^{-t/\tau_b} - be^{-t/\tau_M} \tag{2.12}$$

In our case, we can easily confirm τ_M is the longer timescale because the MOT lifetime fitted after 40 ms depends on the MOT beam intensities and the number of photons cycled on the molecules. If the lifetime were dominated by τ_b, which is the case described in Section 2.4.3, the later lifetime would not depend on such MOT parameters.

Since the molecular beam keeps passing by the detection region for $\sim \tau_b$ amount of time, the fluorescence detected at early times partially includes fluorescence from molecules that are not or are nearly trapped in the MOT. Although such molecules get imaged for shorter amounts of time compared to fully trapped molecules, resulting in a smaller contribution to the overall fluorescence, this background fluorescence may distort our fits to the model and prevent accurate calibration of the peak number of molecules trapped in the MOT.

In order to avoid this background from the molecular beam, we have conducted the following test that always images the molecules after times sufficiently later than $t = \tau_b$.

We image the MOT with an EMCCD camera for a duration of 50 ms starting at $t_{image} = 45$ ms after the slowing ends. The signal here is dominated by the molecules that are fully trapped in the MOT. Then, we vary the time we turn on the MOT laser beams T_{MOT} between $t = 0$ ms and $t = t_{image} = 45$ ms. Using this information, we can back out τ_b in a background-free way. We also denote $T_{collect} = t_{image} - T_{MOT}$.

Then, following Equation (2.13), the number of molecules (per unit time) that were loaded at time $t = t_1 (> T_{MOT})$ and which survive at time t_{image} can be described as

$$\dot{N}_{survive}(t_1) = rN_0 e^{-t_1/\tau_b} e^{-(t_{image}-t_1)/\tau_M} \tag{2.13}$$

Therefore, the total MOT number at time t_{image} is, following Equation (2.9) with different integration bounds:

$$\begin{aligned} N_{MOT}(T_{MOT}) &= \int_{T_{MOT}}^{t_{image}} \dot{N}_{survive}(t_1)\, dt_1 \\ &= \int_{T_{MOT}}^{t_{image}} rN_0 e^{-t_1/\tau_b} e^{-(t_{image}-t_1)/\tau_M}\, dt_1 \end{aligned} \tag{2.14}$$

Solving this integral gives

$$\begin{aligned} N_{MOT}(T_{MOT}) =& \frac{rN_0}{1/\tau_M - 1/\tau_b} \times \\ & \left(e^{-t_{image}/\tau_b} - e^{-T_{MOT}/\tau_M + T_{MOT}/\tau_b - t_{image}/\tau_M}\right) \\ =& \frac{rN_0}{1/\tau_M - 1/\tau_b} \times \\ & e^{-t_{image}/\tau_b}\left(e^{T_{collect}(1/\tau_b - 1/\tau_M)} - 1\right) \end{aligned} \tag{2.15}$$

Since we image with an EMCCD for these tests, there will always be a constant offset C for the fluorescence photons registered after $t = t_{image}$. Therefore, the general fluorescence as a function of $T_{collect}$ can be written as:

$$N_{MOT}(T_{collect}) = A(e^{T_{collect}(1/\tau_b - 1/\tau_M)} - 1) + C \tag{2.16}$$

where A is a constant that absorbs all the amplitude information, and C is a constant offset.

Using this method, we determined the τ_b and τ_M of our MOT. The results are shown in Fig. 2.23.

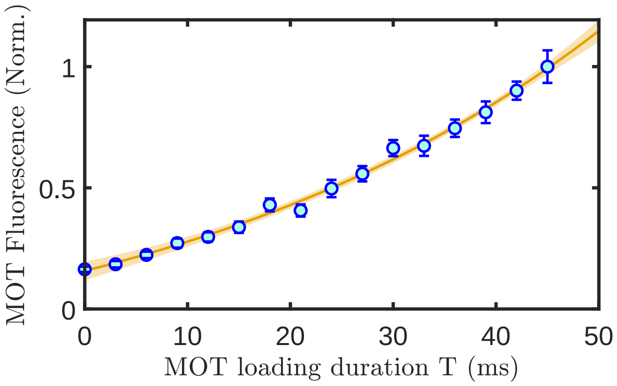

Figure 2.23: MOT fluorescence as a function of loading duration. The fluorescence was collected starting at $T_{collect} = 45$ ms. The fit to Eq. 2.16 is shown in yellow. Errorbars denote 1σ uncertainty of data, while fill regions show 95% confidence interval on the fits. The loading decay time extracted from the fit is $\tau_b = 17.7(1.1)$ ms. The MOT lifetime was separately measured to be $\tau_M = 29.1(1.7)$ ms for this MOT configuration. Retrieved from Ref.[43]

In the case of short MOT lifetimes compared to the beam decay time, i.e., $\tau_M < \tau_b$, the MOT signal will appear as it rises with a short time constant τ_M and then decays with the beam decay time τ_b. In this regime, it is very easy to confuse the MOT lifetime with the beam lifetime, as explained in Section 2.4.2. When the fluorescence signal at late times is fitted to a decay, the fit will always yield a decay time equal to the beam decay time.

A simple diagnostic to check if this is the case is the following: examine the rise time of the fluorescence at early times and compare it to the beam decay time. As described by the numeric model, in the $\tau_M < \tau_b$ limit, the rise time is dominated by τ_M, while in the $\tau_b < \tau_M$ limit, it is dominated by τ_b.

2.4.3 USING THE MODEL TO EXPLAIN LIFETIME MYSTERIES

When newly developing a MOT loaded by a CBGB, it is possible to fall into the pitfall of confusing MOT lifetimes with a fluorescence decay that is characterized by the beam decay time. This often

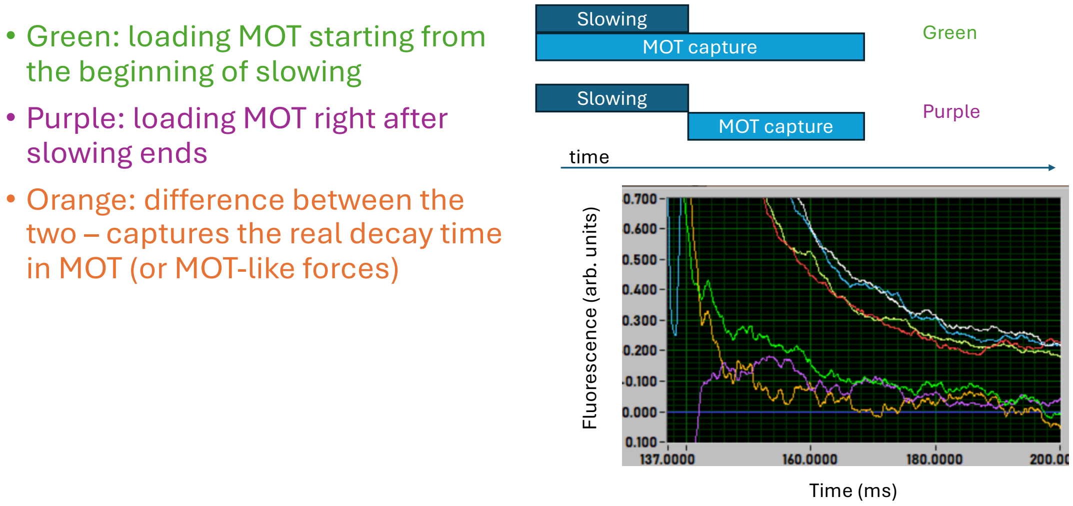

- Green: loading MOT starting from the beginning of slowing
- Purple: loading MOT right after slowing ends
- Orange: difference between the two – captures the real decay time in MOT (or MOT-like forces)

Figure 2.24: Fluorescence signal with 1 cm diameter MOT beams. The data was taken with a photomultiplier tube (PMT). The trace corresponding to turning on the MOT beam after the slowing ends has a short rise time, whereas the trace with the MOT beam always turned on does not have that signature. We confirm there is a short-lived fluorescence signal from MOT-like forces on top of the extended loading signal by taking the difference of MOT beams turned on before and after the slowing ends.

leads to confusion about the "MOT lifetime" seemingly not depending on factors it should, such as MOT beam intensities and number of photons cycled on the molecules.

Especially when the MOT is not fully optimized so that it does not have high enough MOT capture velocities, it is possible that the molecules can fluoresce for a few ms while they are efficiently decelerated by MOT-like forces as they pass through the MOT region, but not effectively trapped. Initially with the SrOH MOT, we used MOT beam diameters of 1 cm, which did not provide enough deceleration distance within the MOT to effectively capture the molecules. This effect will resemble a short MOT lifetime in the extended loading model, which manifests as a very short rise time at the beginning of the fluorescence signal. Typically, this short rise is not seen or is seen with a very small amplitude, because we typically turn on the MOT beams before the white-light slowing ends, so the short rise has already taken place before $t = 0$. A typical fluorescence trace under this condition is shown in Fig. 2.24. We see in the case of MOT beams turned on before slowing ends, the fluorescence trace looks like a single exponential decay. This is a typical characteristic of short-lived fluorescence loaded from an extended beam. By turning on the beams after the slowing ends, we see the rising feature of the fluorescence, whose timescale is mostly characterized by the timescale over which the MOT-like forces hold onto the molecules. The difference of the two traces is also plotted, whose decay time indicates the timescale that the MOT-like forces hold onto the molecules.When newly developing a MOT loaded by a CBGB, it is possible to fall into the pitfall of confusing MOT lifetimes with a fluorescence decay that is characterized by the beam decay time. This often leads to confusion about the ”MOT lifetime” seemingly not depending on factors it should, such as MOT beam intensities and number of photons cycled on the molecules.

2.5 Spectroscopy in the MOT

Now that we have a MOT with decent lifetimes, we further improved it by adding two more repump lasers to the existing repump scheme with ten lasers.

2.5.1 Additional repump states in SrOH

The two additional states to repump are the (12^00) and (12^20) states. The branching ratios to these sets of states were measured to be $\sim 3 \times 10^{-5}$ on average throughout our optical cycling scheme[42]. Although we established an optical cycle with ten lasers that can cycle $\sim 10^4$ photons, plugging these leaks at the $\sim 10^{-5}$ level has the potential to improve the photon budget by an order of unity. It turned out in the end that it improved the photon budget by a factor of 1.5, which improved the final MOT number by a factor of ~ 4.

We pumped these additional ground states through states in the $\tilde{A}^2\Pi(020)$ manifold, as shown in Fig. 2.25. Another option was to go through the states in the $\tilde{B}^2\Sigma^+(020)$ manifold. However, recovery through the $\tilde{B}^2\Sigma^+$state was not as efficient, possibly indicating dissociation of the molecule.

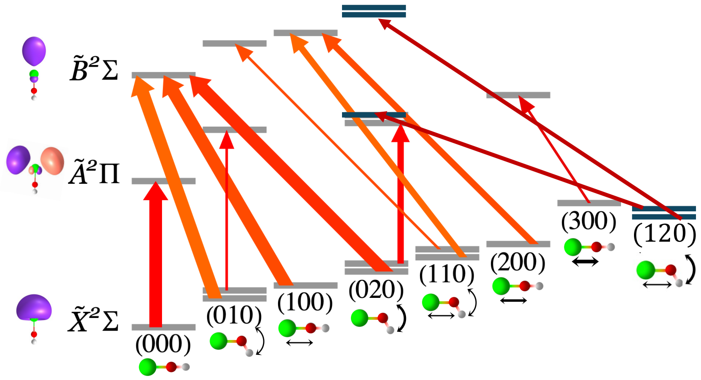

Figure 2.25: Overview of additional (120) repump states and repump pathways

2.5.2 A(020) STRUCTURE

We would like to use the (02^00) state in the $\tilde{A}^2\Pi_{1/2}$manifold, and the (02^20) state in the $\tilde{A}^2\Pi_{3/2}$manifold, because those are the vibrational states that can have $J = 1/2$ states. From now on we will call these states ”$\tilde{A}^2\Pi_{1/2}(02^00)$” and ”$\tilde{A}^2\Pi_{3/2}(02^20)$”, respectively.

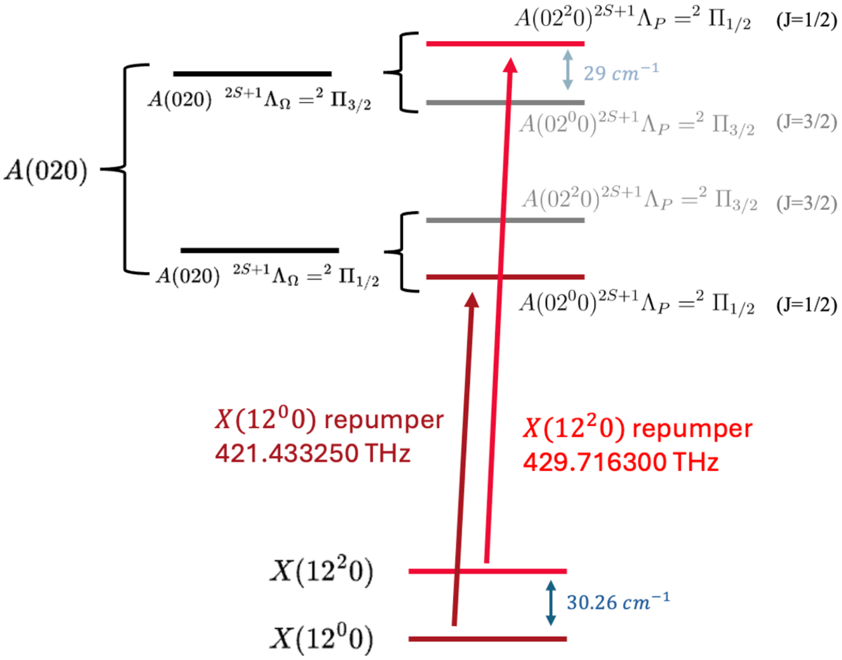

Figure 2.26: Detailed structure of the $\tilde{A}^2\Pi$(020) states and the repump pathways.

2.5.3 DEPLETION AND REVIVAL SCANS

To find excited states, all we need to do is drive a transition whose ground state is in the existing optical cycle, and look for depletion of the MOT. This method is used to identify excited states with high SNR, because all we are looking for is whether the MOT disappears.

To find ground states, we need to first pump into those states through optical pumping. For example, to pump into $X(12^20)$, we first cycled on the diagonal ”$\tilde{A}^2\Pi_{1/2}(02^20)$” $\leftarrow X(02^20)$ line, so

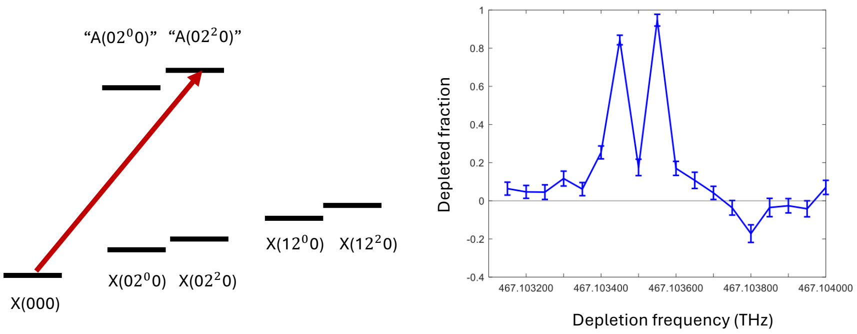

Figure 2.27: Depletion scan of the ”$\tilde{A}^2\Pi_{3/2}(02^00)$” ← $\tilde{X}^2\Sigma^+(000)$ transition. Spin-rotation splitting of 110 MHz is observed.

that eventually the molecules get pumped into $X(12^20)$. This diagonal line was easy to find because we separately knew the energies of ”$\tilde{A}^2\Pi_{1/2}(02^20)$” and $X(02^20)$. However, one unfortunate thing is that since we found this line exactly where it should be, we did not do any scans around it, missing the parity-doublet structure in the ”$\tilde{A}^2\Pi_{1/2}(02^20)$” state, which became a mystery later.

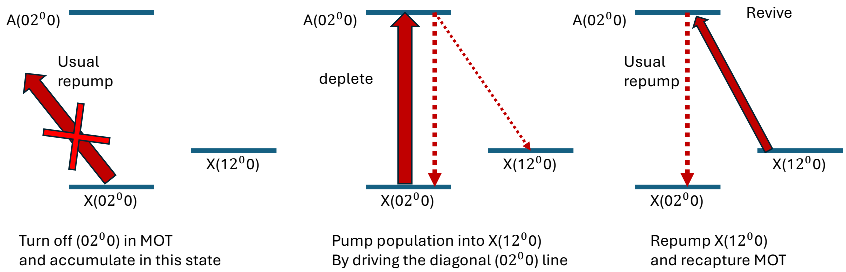

Figure 2.28: Illustration of a depletion-revival scheme.

Once pumped into the desired ground state, we can apply a probe laser beam to repump the molecules back into the optical cycle, and then recapture the MOT. Since the molecules are initially trapped and cooled before performing the optical cycling, we have enough time to perform this optical pumping before it is too late to recapture the MOT when the molecules fly out of the MOT region.

The broad lineshape arises because the molecules are well cooled by the MOT, thus they remain

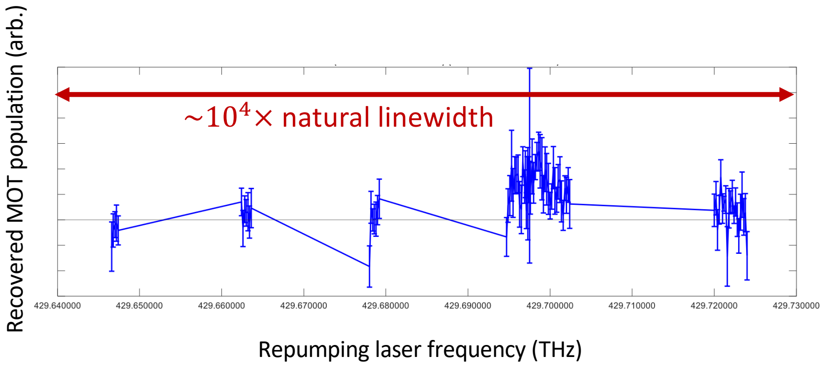

Figure 2.29: An example of a revival scan. The peak turns out to be a transition that is rotationally lossy (driving $X(12^20)$ to the lower $\tilde{A}^2\Pi_{1/2}(02^20)$ manifold, whose lowest *J* is 3/2), therefore only partial revival is observed.

in the probe laser beam region for a relatively long time (a few to tens of ms). Once the molecules get repumped (by one photon scatter) during this time, they are back in the photon cycle. Therefore, even when the probe laser is off-resonant by many GHz, as long as the Rabi frequency is on the order of a kHz, it can get repumped and recaptured by the MOT.

2.5.4 Driving the repump transitions

Fig. 2.30 shows the fine frequency scans for each new repump laser when they were added in the slowing path.

2.5.5 Confirming parity splitting in the excited state

By performing finer scans on the "$\tilde{A}^2\Pi_{3/2}(02^20)$" $\leftarrow \tilde{X}^2\Sigma^+(12^20)$ transition, we observed a double-peak structure of about 250 MHz (see Fig. 2.31).

First, we confirmed whether these two lines were both repumping the same population (see Fig. 2.32). To confirm this, we drove each of the peaks with separate lasers. When only the higher frequency peak was driven, we saw MOT number increase in the expected frequency range. We then scanned

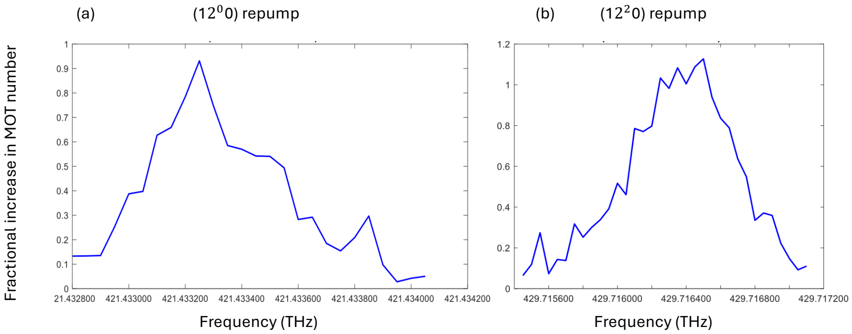

Figure 2.30: Repumping each (120) ground state in the slowing and MOT sequence. The fractional increase in MOT number is plotted, which means a fractional increase of 1 doubled the MOT number. (a) "$\tilde{\mathrm{A}}^2\Pi_{1/2}(02^00)$" $\leftarrow \tilde{\mathrm{X}}^2\Sigma^+(12^00)$ transition. (b) "$\tilde{\mathrm{A}}^2\Pi_{3/2}(02^20)$" $\leftarrow \tilde{\mathrm{X}}^2\Sigma^+(12^20)$ transition.

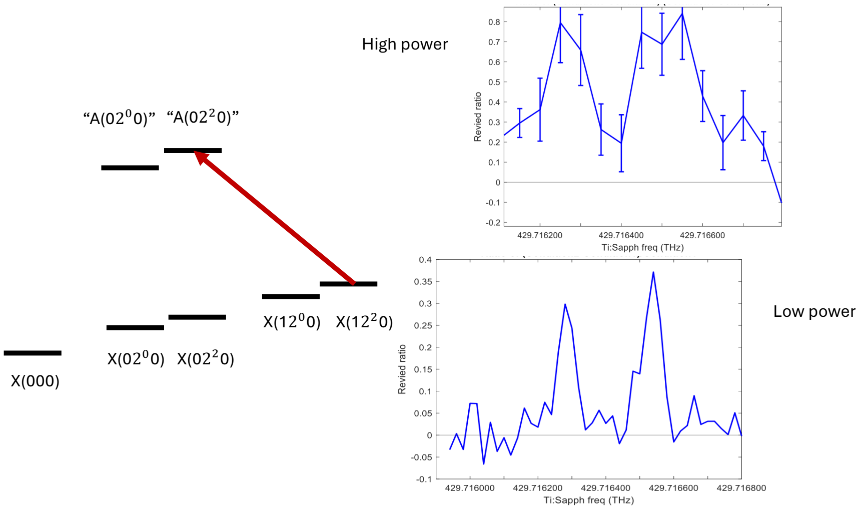

Figure 2.31: Confirming the double-peak structure in "$\tilde{\mathrm{A}}^2\Pi_{1/2}(02^20)$" $\leftarrow \tilde{\mathrm{X}}^2\Sigma^+(12^20)$ transition.

this range again, but this time with another laser always addressing the lower frequency peak. Then we did not see any increase above what the lower frequency peak had already produced. Therefore, we concluded that these two peaks are signs of repumping the same population.

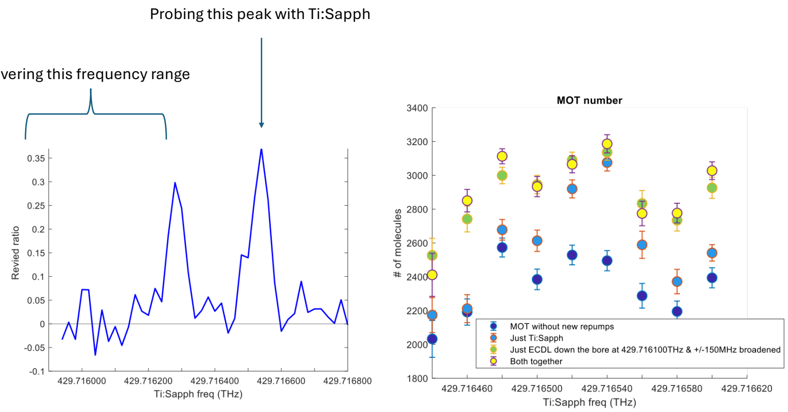

Figure 2.32: Checking if the two transitions contribute additively in the ”A(02^20)” $\leftarrow \tilde{X}^2\Sigma^+(12^20)$ transition.

Next, we confirmed the origin of this double peak: is it in the ground state or the excited state? We first checked the ”$\tilde{A}^2\Pi_{1/2}(02^20)$” $\leftarrow \tilde{X}^2\Sigma^+(02^20)$ transition. This transition was already driven to pump the molecules into the $\tilde{X}^2\Sigma^+(12^20)$ state. However, since we already knew the energies of the excited and ground states of this transition before having driven it for the first time, we did not perform an extensive frequency scan. As shown in Fig. 2.33, we found another depletion feature $\sim$ 250 MHz below the originally observed line.

This already strongly suggested that the doubling was in the ”$\tilde{A}^2\Pi_{1/2}(02^20)$” state. We further confirmed that this $\sim$ 250 MHz doublet structure does not originate from the $\tilde{X}^2\Sigma^+(02^20)$ state. As shown in Fig. 2.34, we scanned our usual repump laser for $\tilde{X}^2\Sigma^+(02^20)$ over a range of ± 300 MHz and did not see any additional repump features.

Therefore, we concluded the following: The $\sim$ 250 MHz doublet structure lies in the $\tilde{A}^2\Pi_{3/2}(02^20)$ state. Since it can only be accessed by ground states that have unresolvable, fully mixed parity doublets, it suggests that this splitting is a parity splitting. Other transitions, such as from the $\tilde{X}^2\Sigma^+(000)$, can-

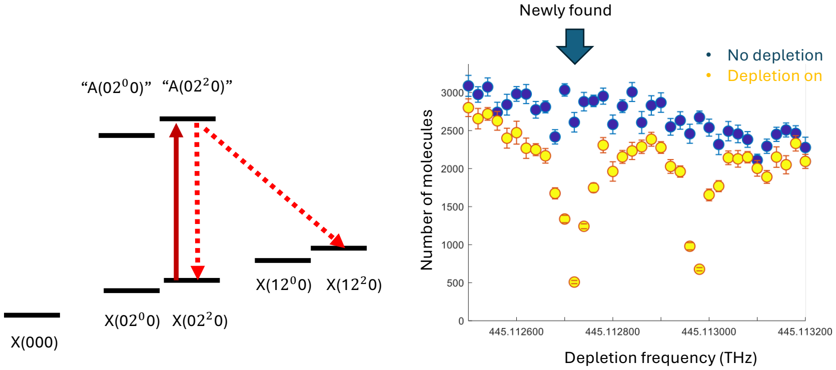

Figure 2.33: Checking if the doublet structure exists in the ”$\tilde{A}^2\Pi_{1/2}(02^20)$” $\leftarrow \tilde{X}^2\Sigma^+(02^20)$ transition.

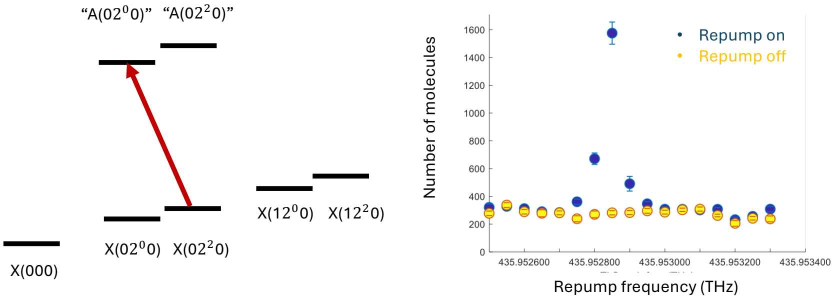

Figure 2.34: Confirming that the doublet structure does not exist in the ”$\tilde{A}^2\Pi_{3/2}(02^00)$” $\leftarrow \tilde{X}^2\Sigma^+(02^20)$ transition.

not access this doublet since only the negative parity state is populated in the laser cooling cycle (See Fig. 2.27). The conclusion is also illustrated in Fig. 2.35.

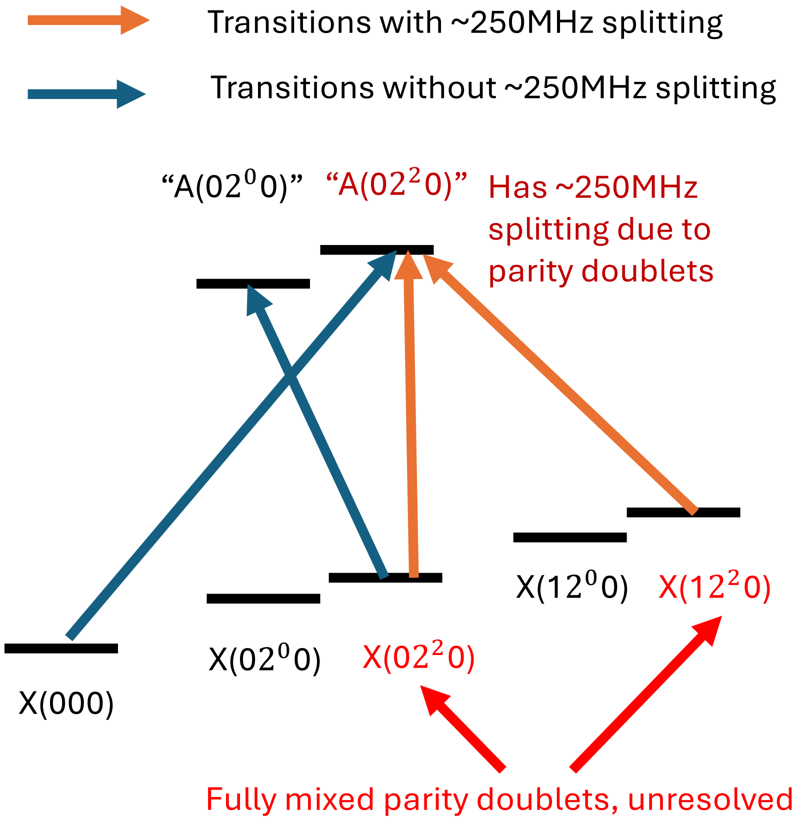

Figure 2.35: Overview of the $\tilde{\mathrm{A}}^2\Pi(02^20)$ parity doublet tests

Here is a first-order argument of why the parity doublet splitting is on the order of 100 MHz instead of a few MHz for a typical bending mode in the $\tilde{\mathrm{X}}^2\Sigma^+$manifold. For $\ell = 0$ states in the $\tilde{\mathrm{A}}^2\Pi$manifold, the parity splitting due to Λ-type doubling is on the order of a few GHz. The ”(02^20) state” actually has $\sim 10\%$ of (02^00) character mixed in by Renner-Teller coupling. Thus, by first-order perturbation theory, the parity doubling also gets added by $\sim$ 10%, resulting in the order of 100 MHz. Detailed calculations of this parity splitting are underway by Annika Lunstad et al.

2.6 Improved MOT with newly added repumping lasers

By adding the two new repump lasers to the experiment, we saw the MOT number increase by up to a factor of ~ 4, and the MOT lifetime increase by over a factor of 1.5.

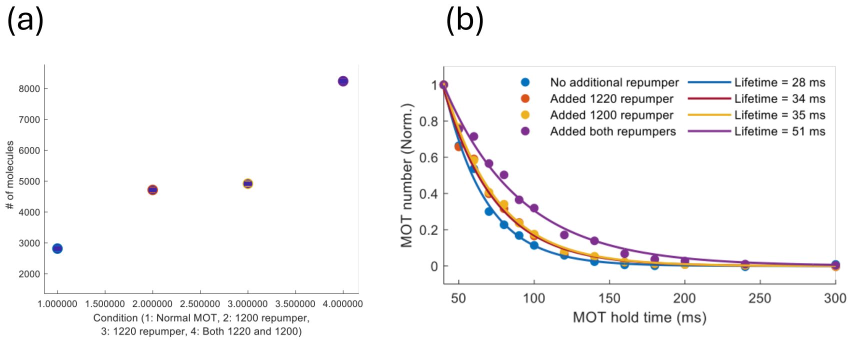

Figure 2.36: Improved (a) MOT number and (b) lifetime of the MOT after adding each new repump.

2.6.1 Calibrating the photon budget

We calibrated the photon budget with the following method. We first captured the MOT for 45 ms as usual. Then we used Λ-enhanced gray molasses, explained in the next chapter, to reduce the temperature of the molecules. This allowed for enough interaction time in the MOT region to optically pump all molecules in the $\tilde{X}^2\Sigma^+(000)$ ground state, without significant loss of molecules flying outside of the MOT region. This ensures that we always compare with the same initial condition in the next step. We then chose a specific number of lasers to turn on while recapturing the MOT.

By changing the number of lasers turned on to recapture the MOT and measuring the corresponding fluorescence until the molecules fall into dark states, we can map the relation between the lasers used and the number of photons cycled. When only the (000), (100), and (200) repumps are turned on (3-laser condition), we know the photon budget well from branching ratio measurements. Then, to first order, by comparing the fluorescence (which is proportional to the photon budget), we can scale the known 3-laser condition photon budget proportionally with the measured fluorescence. A more careful analysis was done by fitting to a model that includes the extra loss to states outside the 12 ground states we are repumping, using measured branching ratios as inputs. Using this analysis, we were able to extract this extra loss branching ratio to unaddressed states to be about 3×10^{-5}. The photon budgets fitted from this model are shown in Table 2.2.

Number of repump lasers	Lasers added	γ
3	(000), (100), (200)	933(35)
5	…, (010;$N = 1, 2$)	1522(82)
7	…, ($02^0 0$), ($02^2 0$)	4603(226)
8	…, (300)	6509(313)
10	…, (110;$N = 1, 2$)	9813(461)
12	…, ($12^0 0$), ($12^2 0$)	14576(669)

Table 2.2: Repump lasers and corresponding photon budgets.

3

Sub-Doppler cooling and optical dipole trapping of SrOH

Since we were able to achieve a MOT of SrOH with a reasonable number and lifetime, we have moved on to cooling the molecules further into a conservative trap, which would be more suitable for performing precision measurements[6]. Similar work on sub-Doppler cooling and optical trapping of polyatomic molecules has been done wth CaOH molecules[34].

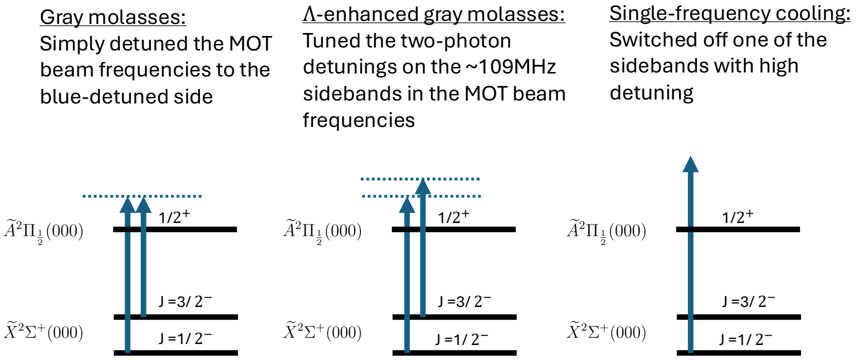

Figure 3.1: Overview of sub-Doppler cooling methods.

3.1 Λ-ENHANCED GRAY MOLASSES

Since we drive type-II transitions for rotational closure for laser cooling, sub-Doppler cooling requires blue-detuned light instead of red-detuned light. See theses of Loïc Anderegg and Nathaniel Vilas for details.

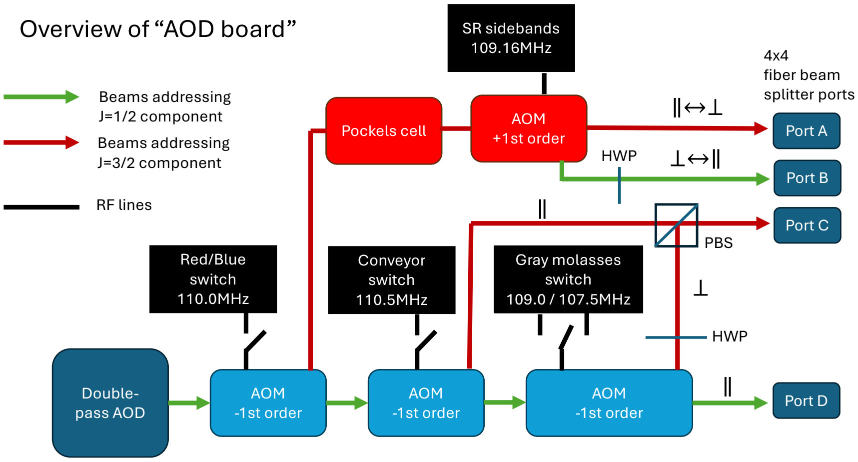

Figure 3.2: Board layout for generating different frequencies for the MOT beams.

We have made large modifications to the AOD board (see Alexander Frenett's thesis for details on the old configuration), so that we can send the correct frequency components with the correct polarizations in all of the red RF MOT, (Λ-enhanced) gray molasses, single frequency cooling, and conveyor belt MOT configurations. The two main considerations when designing this board were the following: First, the beam used for the single frequency (SF) cooling was always sent through the 0 th AOM diffraction order. This was so the power efficiency into the SF path was optimized. Second, only the red MOT beams (the only beams that require fast polarization switching) were sent through the Pockels cell, instead of switching the Pockels cell RF off when the light does not require fast polarization switching. Although we did not directly measure this on our apparatus, we knew from the CaF and CaOH experiments that the Pockels cell can drift the polarization for a few ms right after it is turned off.

We also added a $+5$ V offset to the VCO control voltage through a voltage adder to shift the frequency range of the VCO that is used to drive the double-pass AOD. The analog output channel of the NI control system outputs -10 V to $+10$ V. By adding a $+5$ V offset, we shifted this range to -5 V to $+15$ V. This allowed the VCO to output all frequencies between 70 MHz to 140 MHz, which was the full operating frequency range (single pass) of the AOD.

In addition, we purchased a new 688 nm SFG system (which is technically a backup mainline laser), and we installed it specifically for the MOT beam and separated it from the main line slowing laser. This allowed us to scan up to higher powers than we could have conceivably achieved with the old system, and in some cases, such as single frequency cooling, we potentially needed this high power.

An AOM switch was installed to separate the newly added "blue path" from the old "red path" that was used for the red RF MOT. We call this the "Red/Blue switch." This switch allows for all the sub-Doppler (blue-detuned) laser beams to not go through the Pockels cell. Everything downstream from the Pockels cell was identical to the previous AOD board setup. When jumping from red-detuned frequencies to blue-detuned frequencies, we jumped the double-pass AOD frequency by jumping the

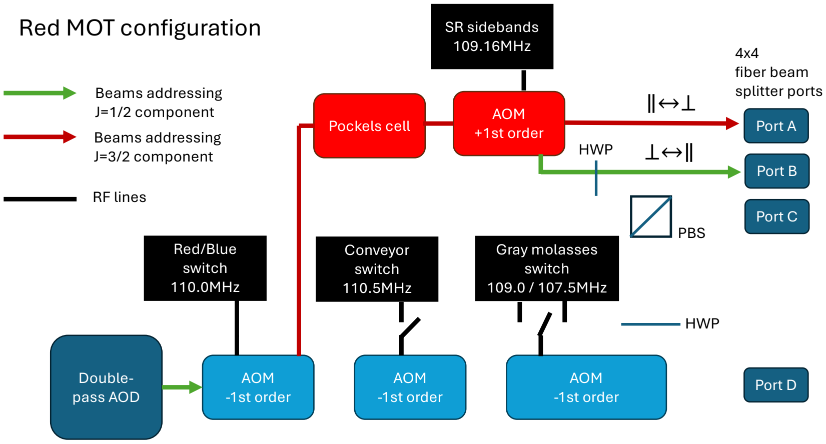

Figure 3.3: When forming the red MOT in this setup, the Red/Blue switch is switched on, sending all the light through the Pockels cell pathway.

VCO control voltage through the Cicero control program. At the same time, the Red/Blue-switch AOM was turned off.

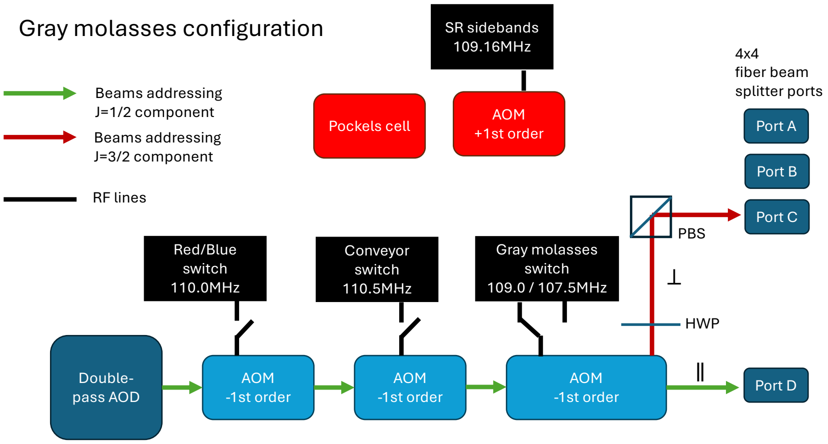

Figure 3.4: For gray molasses cooling, only the "Gray molasses" switch is switched on at 109 MHz (for optimal cooling), splitting off some light into the J=3/2 component.

The blue path was split into three different pathways using AOMs with frequencies tuned around the SR splitting. Two out of the three paths were set to drive from the $J = 3/2$ state, and one of the three paths was set to drive out from the $J = 1/2$ state. The two $J = 3/2$ states have opposite polarizations. Only one of the $J = 3/2$ components was used for the gray molasses cooling, which was the component that has the opposite polarization from the $J = 1/2$ component.

We revived the (100) vertical beam, which is the (100) repumping laser sent in from the z-direction on resonance, combined and co-propagating with the MOT z-beam, and retro-reflected. This was important to center the RF MOT closer to the center of the B-field. We saw the MOT form ~ 1 mm closer to the beam box when the (100) chirped slowing light was used instead of the vertical beam for repumping in the MOT, due to non-negligible radiation pressure from $\sim$ 1 in 20 photon scatters from this laser beam. For every sub-Doppler sequence, we captured the RF MOT for 15 ms with the (100) chirped slowing beam, followed by 10 ms capture with the (100) vertical beam.

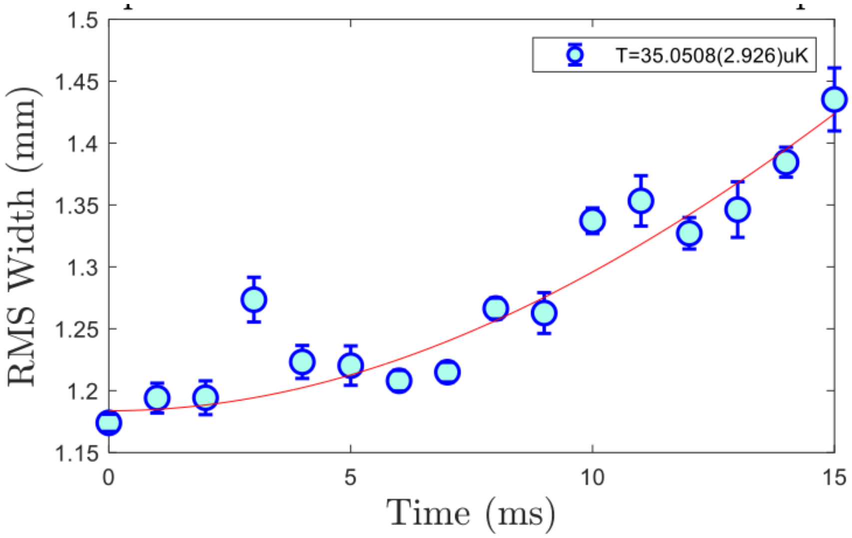

Figure 3.5: Example of gray molasses temperature by time-of-flight measurement.

The temperature of the gray molasses was measured using time-of-flight (ToF) measurements, similarly to how we measured the temperature of the red-detuned RF MOT in the previous chapter. An example ToF measurement is shown in Fig. 3.5. After the gray molasses step, we released the molecules for a certain amount of time and then imaged for 2 ms while jumping the MOT beam frequencies to be on resonance.

We did various scans of the gray molasses parameters, such as the overall detuning Δ, the two-photon detuning δ, and the overall beam intensity. Such scans are shown in Fig. 3.6.

3.2 SINGLE FREQUENCY COOLING

We next demonstrated single frequency cooling, which uses only one of the blue-detuned components at relatively large detuning and intensity. This method is useful for cooling while loading an ODT,

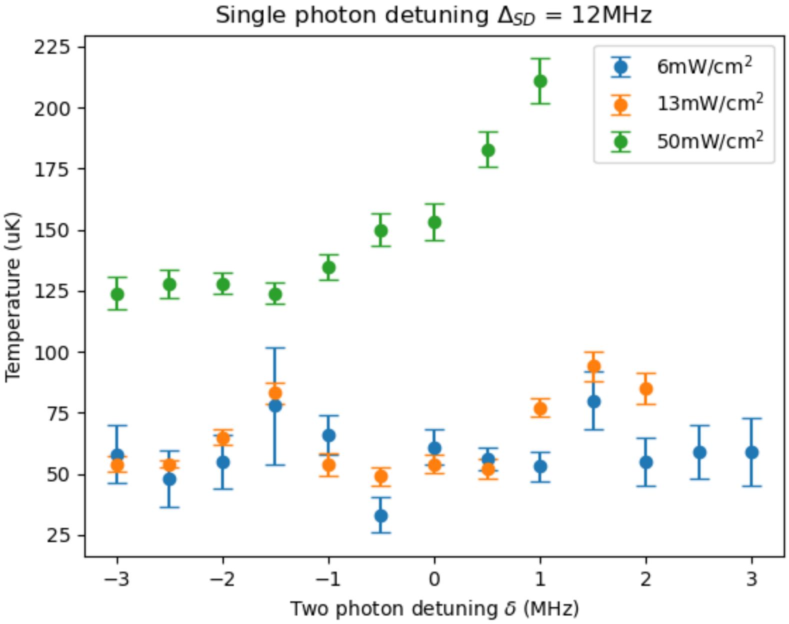

Figure 3.6: Gray molasses cooling two-photon detuning scans for different intensities.

because the large detuning is less affected by the trap shifts caused by the ODT light[34].

We were able to obtain temperatures of 40 μK in the end, by using detunings larger than 60 MHz. Detailed scans are ongoing, to be published.

Cooling Method	Temperature
Gray molasses	53(6) µK
Λ-enhanced gray molasses	35(3) µK
Single-frequency gray molasses	37(2) µK

Table 3.1: Comparison of different cooling methods and their achieved temperatures so far.

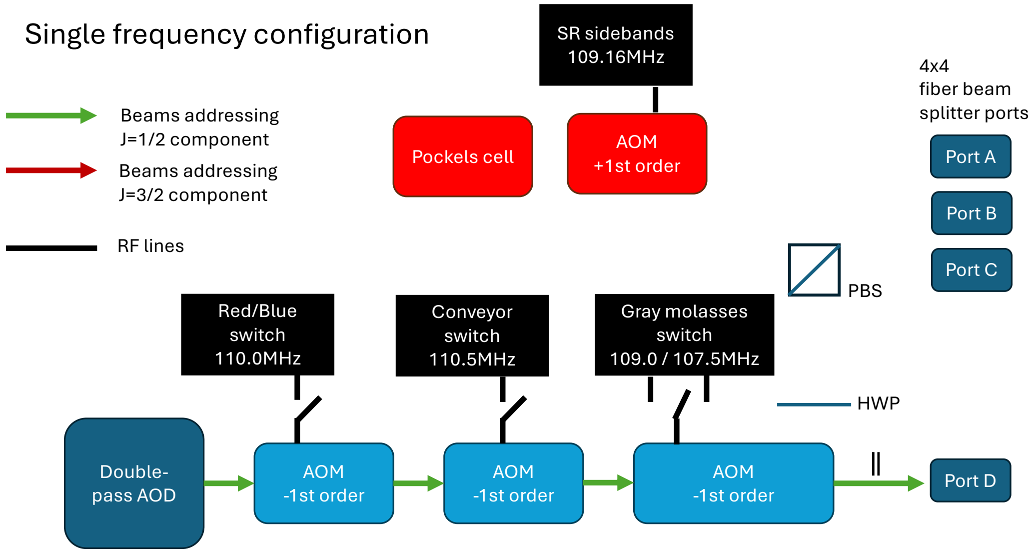

Figure 3.7: For single frequency cooling, all AOMs are switched off, allowing all the power to be sent into one port with minimal power loss.

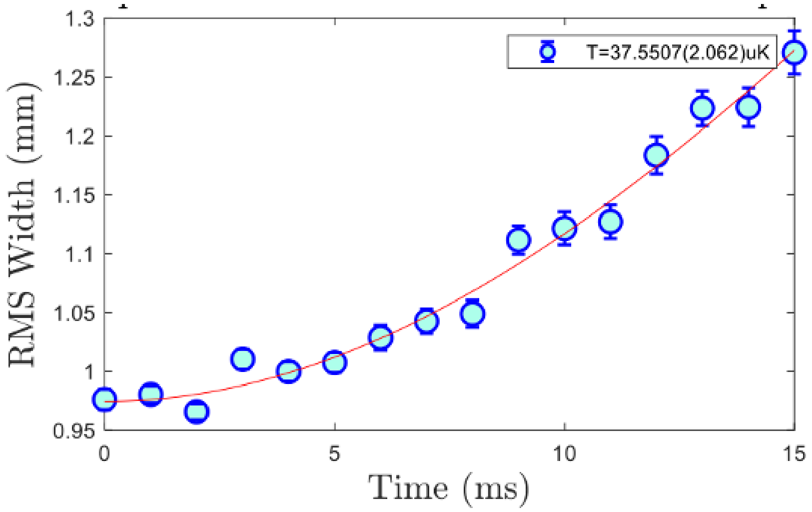

Figure 3.8: SF cooling reaching 40 μK. $+90$ MHz detuning, 40 mW per laser beam (25 mW/cm^2 intensity), 3 ms cooling time.

3.3 CONVEYOR BELT MOT

The next step is further compressing the sub-Doppler cooled cloud by using a blue-detuned DC MOT. Specifically, we demonstrated the "conveyor belt MOT" configuration, previously demonstrated with CaOH[44,33] and CaF[60], which uses closely separated frequencies with opposite circular polarization that form a walking standing wave. The AOD board configuration is illustrated in Fig. 3.9.

We checked the orientation of the B-field and conveyor belt directions (detunings of the $J = 3/2$ components) to make sure we were running in the optimal orientations.

In 10 ms, the DC B-field was ramped linearly up to 80 G/cm. This was done with a high-bandwidth DC power supply Delta Elektronika SM120-50. We made sure to order the high-speed programmable option. We also used a DC voltage-adding circuit shown in Fig. 3.11 to add the voltage onto the coils without disturbing the RF driving circuit. The DC current was added through inductors and also connected through solid-state relays to enable fast (< 1 ms) switch-off of the circuit.

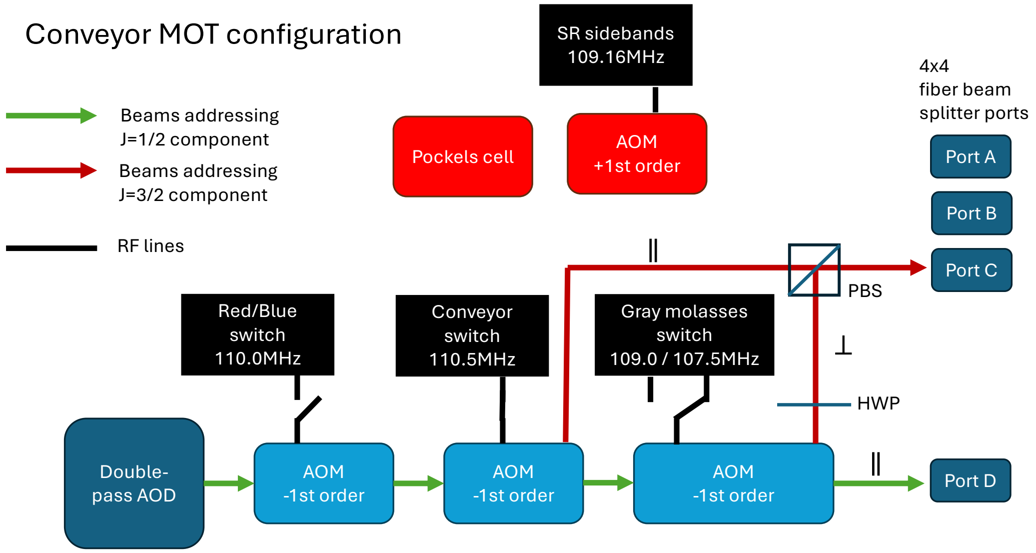

Figure 3.9: When running in the conveyor MOT configuration, both the conveyor switch and the gray molasses switch are turned on. Each of these AOMs turns on a certain polarization component for the J=3/2 conveyor belt light. The gray molasses switch is turned on with a different RF source (107.5 MHz) than when running regular gray molasses, because the optimal frequency for this sideband shifts by a few MHz between these two steps.

Figure 3.10: Checking different orientations of the B-field and detunings (conveyor belt direction).

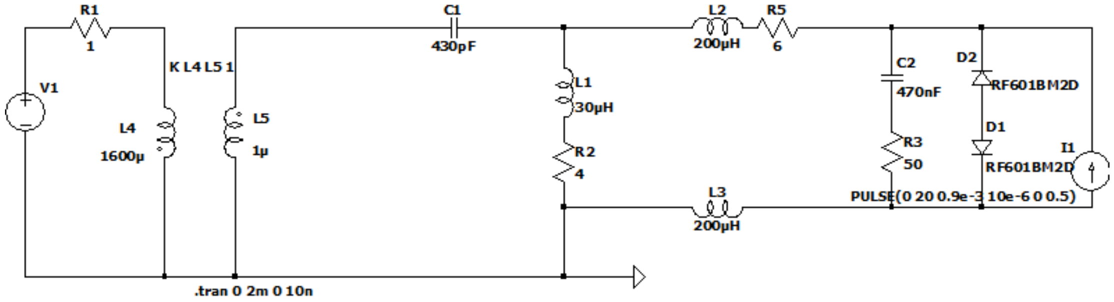

Figure 3.11: Circuit diagram to add the DC current to the existing RF circuit. The circuit for one coil (L1) is shown. The circuit left of L1 is the existing RF circuit, and the right part is the newly added DC circuit.

Figure 3.12: Components inside the DC circuit box.

The ”gray molasses” AOM switch frequency was switched between GM cooling and conveyor MOT to match the optimal frequency guided by simulations.

We were able to compress the molecular cloud near 100 μm using this technique, as shown in Fig. 3.13

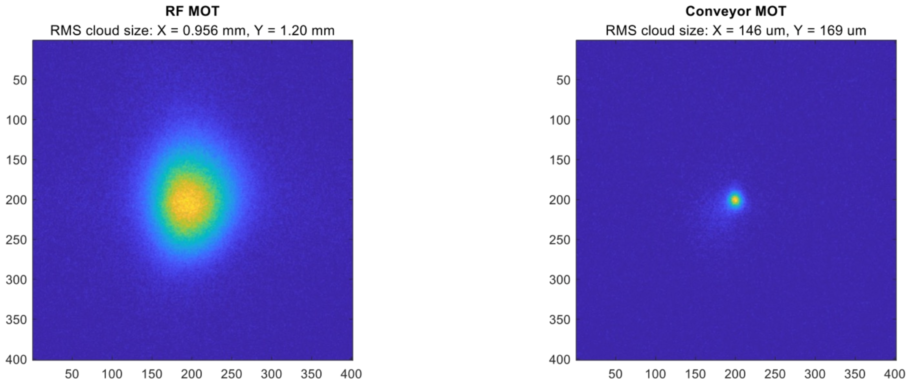

Figure 3.13: Comparison of RF MOT size (left) and conveyor MOT size (right)

3.4 OPTICAL DIPOLE TRAPPING

3.4.1 SETUP

We then demonstrated optical dipole trapping using a high-power ($\sim$ 13 W) laser at 1064 nm. The setup is shown in Fig. 3.14. We focused this beam down to a diameter of $\sim$ 60 μm, resulting in a trap depth of $\sim$ 900 μK. The parts list is shown in Table 3.3.

No.	Component Description
1	PDA 20CS2 IR photodetector for intensity servo
2	Isolator IO-5-1064-HP
3	SRS PID lock box or Moku Go

No.	Component Description
4	FGS900 colored glass
5	Pickoff, PBS
6	PBSW-1064
7	Polarizer - Thorlabs
8	IR mirrors
9	D-shape 1064 mirror BB1E03
10	1064 waveplates from Foctek - optical contact ones WPO225H-1064nm
11	High power beam dumps (Kentek)
12	High power AOM Gooch and Housego AOM 3080-1913
13	RF amp for AOM ZHL-03-5WF+
14	Expander lens
15	Translation stage
16	1064 HR mirror (and dichroic for backup) - DMSP900
17	C-coated aspheric lens

Table 3.3: List of optical and electronic components used in the setup.

3.4.2 LOADING THE ODT

Using this setup, we first tried loading the ODT after the conveyor MOT. However, even after overlapping the ODT laser light well onto the conveyor MOT, we were not able to confirm loading into the ODT. The ODT was designed to have a diameter of 30 μm, and we confirmed it by imaging on the camera.

Therefore, we took a step back and first loaded after the gray molasses.

We were able to demonstrate trapping $\sim$ 80 molecules (initial, with ongoing work to optimize the

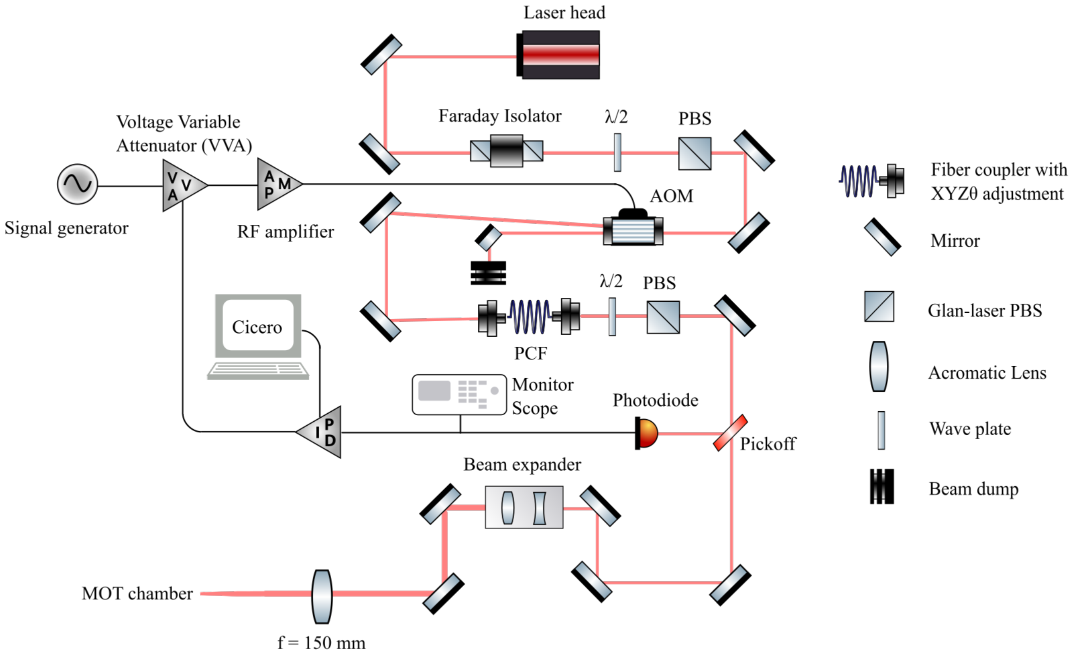

Figure 3.14: ODT laser setup. Image credit to Mingda Li.

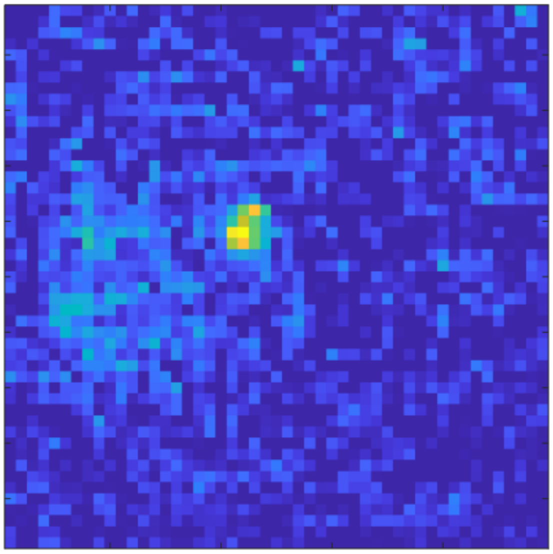

Figure 3.15: Image of ODT after 30 ms of holding. Left of the image is the physical down direction. The untrapped cloud of molecules is falling toward the physical down direction. The imaging area is 5 mm × 5 mm.

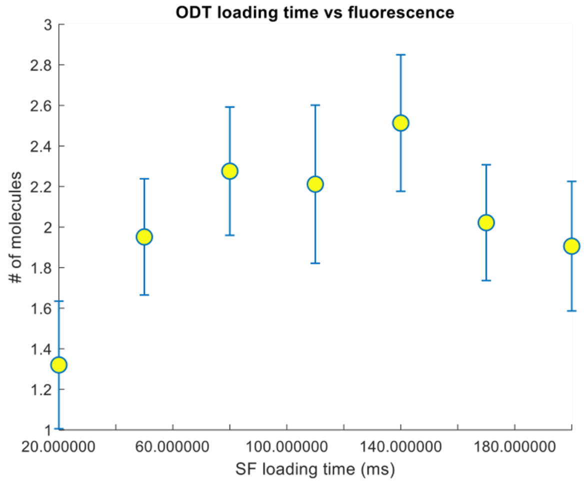

Figure 3.16: ODT fluorescence vs. loading time.

number of trapped molecules) in the ODT and measured a lifetime of 1.2(1) s. The number of molecules was measured by holding the ODT for 200 ms, allowing molecules that were not trapped to fall out of the MOT region, and then re-capturing the red RF MOT.

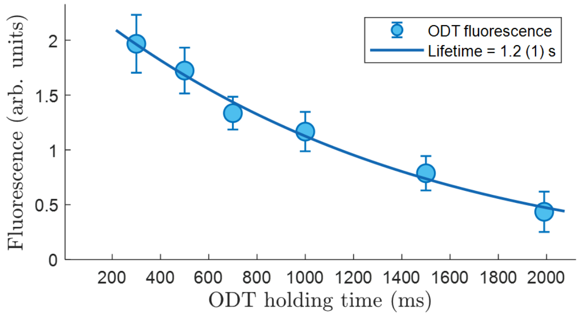

Figure 3.17: Lifetime measurement of the ODT.

Once the focus was close enough, we were able to load after the conveyor MOT. By adding a second gray-molasses cooling stage after the conveyor MOT, we were able to double the loading efficiency. After careful focus and alignment scans, we improved the loading efficiency up to about 4%. Again, number measurements were done by re-capturing the RF MOT after holding the ODT for 200 ms, as explained above.

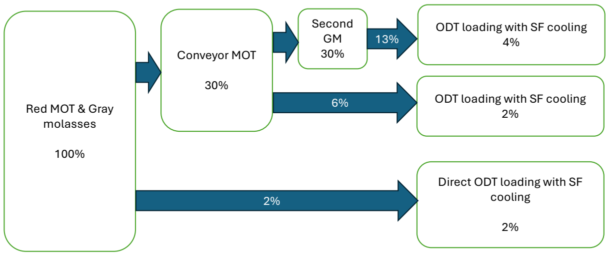

Figure 3.18: Best loading efficiencies so far. Work is ongoing to improve this.

4

Zeeman-Sisyphus deceleration

4.1 PRINCIPLES

We implemented the Zeeman-Sisyphus (ZS) deceleration method for slowing YbOH. The ZS method was first demonstrated on CaOH [1], decelerating the molecules to MOT-capturable velocities. We have extended this method to decelerating YbOH, overcoming the subtleties associated with its complex energy structure [51].

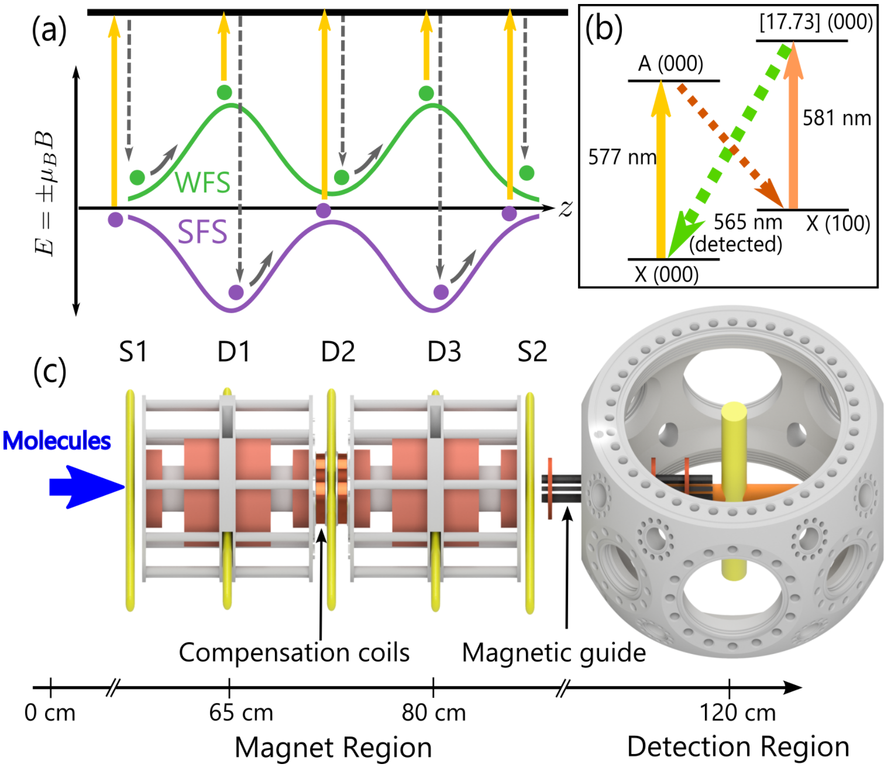

Figure 4.1: (a) Drawing of the ZS deceleration principles. (b) Energy level diagram for YbOH. 577 nm laser light is used for spin flips, and an additional 588 nm laser beam is used for detection. (c) Schematics of the entire ZS setup. Retrieved from Ref. [51].

The ZS deceleration method combines high magnetic fields and optical pumping with few photons. In our setup, we generated magnetic fields with superconducting solenoid coils. The maximum field at the center was 2.5 T. We initially prepare the molecules in the weak field seeking (WFS) ground state as they enter the solenoid. As they travel through the bore of the solenoid, they experience a decelerating force as the potential energy gets higher towards the center of the solenoid. At the center of the solenoid, we perform optical pumping through the excited state to pump the molecules into the strong field seeking (SFS) ground state. The molecules continue traveling through the solenoid bore, again experiencing a decelerating force as the field gets weaker towards the exit of the solenoid. In our apparatus we placed two superconducting solenoids one after another, allowing us to double the amount of energy removal. This aggregates to 8 K of energy removal for the whole ZS decelerator.

4.2 DECELERATION OF YBOH

Two major challenges had to be overcome to make this ZS deceleration work for YbOH. First, the Zeeman shifts in the excited states of YbOH are an order of magnitude larger compared to that of CaOH. Furthermore, the large Λ-type doubling in the excited states puts levels with different spin-orbit coupling close together, within $\sim$ 3 GHz. These two features lead to significant mixing of rotational levels at high fields, reducing the efficiency of the optical spin flip that is done at the peak field in the ZS decelerator. We extensively studied the Zeeman structure of the YbOH excited state and identified optical pumping pathways that would minimize the population loss in the optical pumping process, which is described in detail in[51].

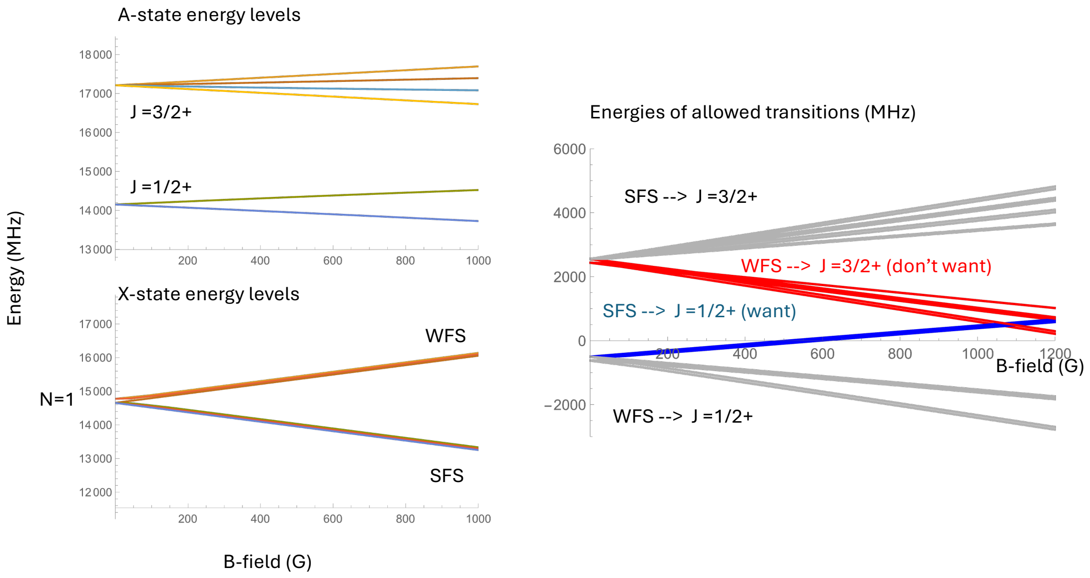

Figure 4.2: Accidental resonance in PR2.

Second, even at low fields where the rotational mixing is not significant, the complex excited state structure itself leads to accidental resonances to transitions that lose the molecules to dark rotation states. In particular, the magnetic field strength between the two solenoids that was used for decelerating CaOH made the optical pumping frequency also in resonance with such an unwanted transition. In particular, we saw complete loss of molecules in PR2. The depletion happened because the ground state Zeeman shift in PR2 was $\sim$ 3 GHz, and that was approximately the splitting between the $J = 1/2^+$ and $J = 3/2^+$ states in the excited state. This is illustrated in Fig. 4.2. As we tried to drive the desired spin-flip transition of ground SFS to excited, $J = 1/2^+$, we were also depleting the WFS population through the rotationally lossy $J = 3/2^+$ excited state.

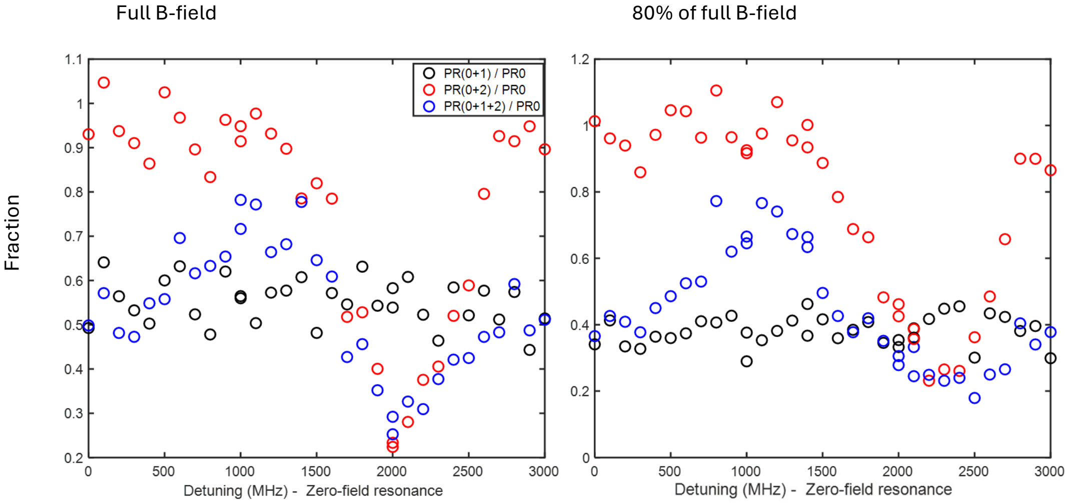

Figure 4.3: Scanning the PR2 laser frequency at full field (left) and 80% of the full field value.

We further confirmed this theory by scanning the detuning of the PR2 spin-flip laser. As shown in Fig. 4.3, first we just had PR0 and PR1 lasers on, as a baseline for the remaining WFS population that was not pumped by PR1 in the PR2 region (black dots). Next, we just had PR0 and PR2 on. PR0 prepared the population in the WFS state, and when PR2 was on resonance, it drove the rotationally lossy transition, depleting all the WFS population. Finally, we had all of PR0, PR1, and PR2 on, which showed the desired spin-flip behavior below the depletion frequency, and showed depletion when the frequency became higher and the lossy transition came into resonance. When we operated at 80% of the full field value, we saw the spin-flip transition and the depletion transition separated out better.

Thus, we built extra compensation superconducting coils to allow tuning of the magnetic field in between the two solenoids to a value where such accidental resonances do not occur. Construction of such compensation coils is covered in detail in Alexander Frenett's thesis.

4.2.1 How and how-not-to include depletion beams

Since we wanted to get rid of background signal in detection, we implemented a velocity-sensitive depletion laser down the bore to selectively deplete a certain range of velocity classes. In particular, the depletion laser was broadened to deplete all the molecules above 40 m/s at zero field. However, we saw depletion over a much wider range than the EOM sidebands should cover, including the slow molecules of interest.

We then realized this method did not work because we were detecting the WFS molecules. Since the WFS molecules shift up in energy as they approach the ZS decelerator, the detuning from the depletion laser gets smaller. Therefore, molecules with smaller Doppler shifts came into resonance with the (supposedly "velocity selective") depletion beam.

One way to save this is to just use the SFS molecules for velocity-sensitive depletion and spin-flip them right before the first magnet, but at the cost of taking a hit in the overall signal (because of the efficiency of spin flip).

Instead, we simply decided to transversely deplete any signal at the end of the ZS decelerator. This transverse depletion did not have any natural velocity selectivity. We turned off the depletion laser early enough so that they were off by the time the relatively late-arriving slow molecules passed the depletion region.

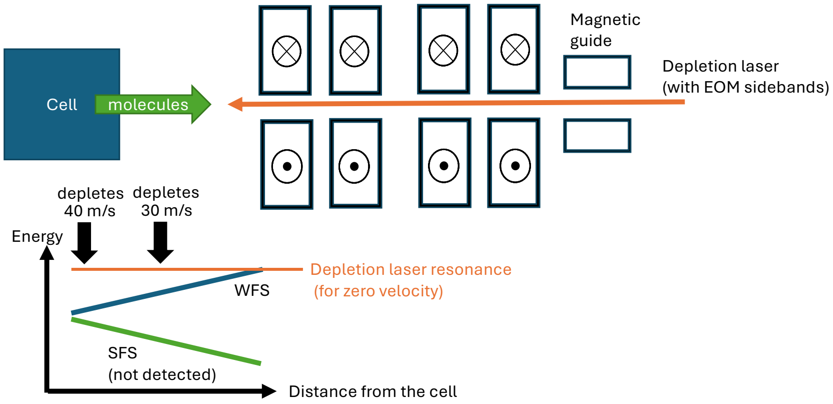

Figure 4.4: Schematics of depletion of fast molecules using a depletion beam down the bore, and why it did not work.

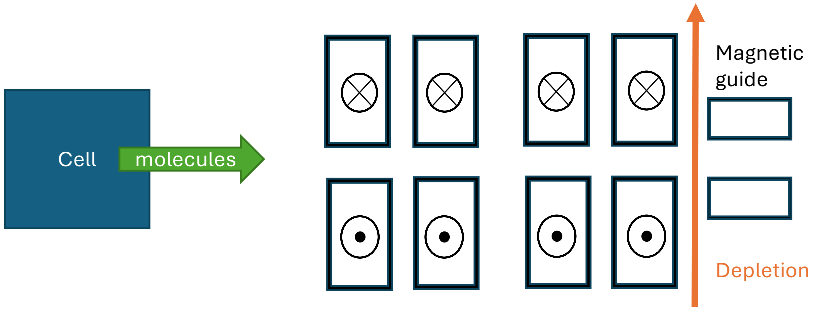

Figure 4.5: We ended up depleting transversely at the end of the ZS decelerator. We relied on the temporal resolution to cut out the early-arriving fast molecules.

4.2.2 INITIAL SIGNAL AND FAST-SWITCHING DETECTION

In the Doppler-sensitive configuration, we implemented chopping of the 581 nm (100) repump detection beam at 500 Hz and sequential comparison of time bins with the laser on and off. This fast-switching method can reduce the (relatively slow) noise associated with scattered light from the 577 nm main line laser beam, which is the dominant source of noise.

Using this method, we first looked at the 30 m/s velocity class, which has relatively good signal. In the unslowed beam, there are still some molecules in this velocity class that can be detected. We compared

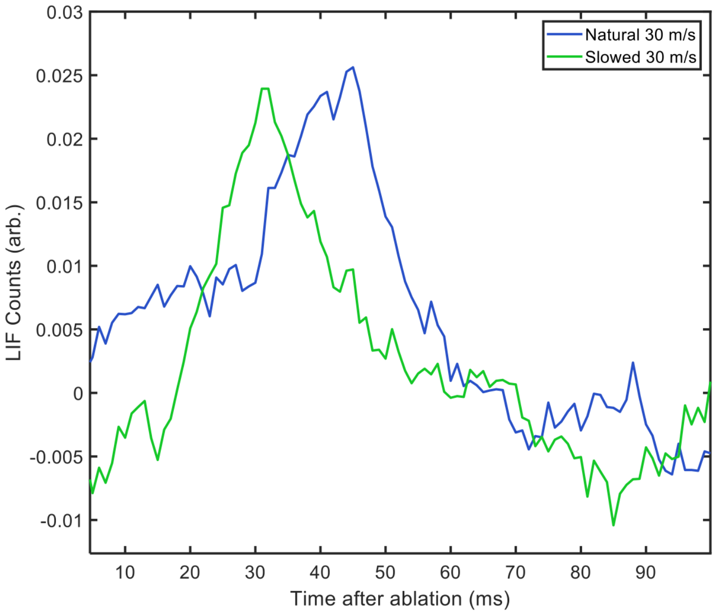

Figure 4.6: Initial sign of ZS slowing on YbOH. We collected fluorescence from the 30 m/s velocity class. The slowed signal shows up at an earlier time, consistent with it being slowed from a faster initial velocity.

this signal to the same velocity class signal when the ZS decelerator was on. We saw that the ZS slowed molecules arrived earlier than the natural 30 m/s signal, which meant that these molecules were slowed from a faster initial velocity.

4.2.3 Final result and outlooks

After resolving the subtleties that occurred in YbOH, we were able to demonstrate deceleration of YbOH molecules to 18 m/s. This deceleration method only used 10 photons, which would save the limited number of photons that can be cycled on YbOH for later processes. Although this beam would require further deceleration to serve as a source for loading a MOT, we have identified main sources of loss in this method, so fixing them would allow us to add more deceleration stages to further decelerate the molecules. Such improvements include replacing high-field optical pumping with

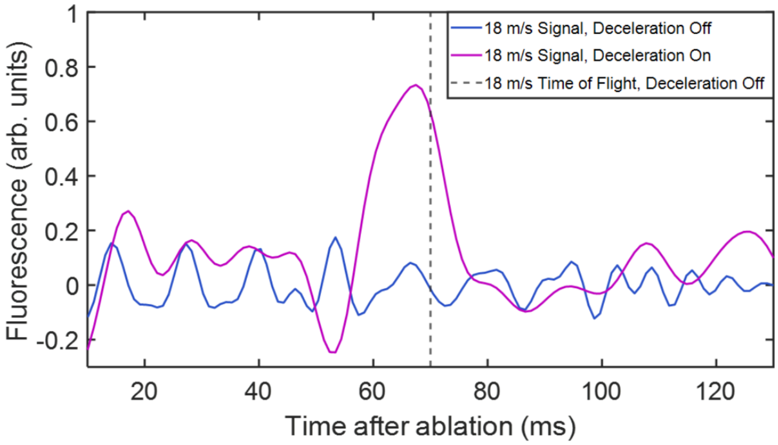

Figure 4.7: ZS slowing of YbOH to 18 m/s.

microwave transitions.

5

Conclusion and Outlook

In conclusion, we have demonstrated the first magneto-optical trapping of SrOH and achieved deep sub-Doppler cooling and optical trapping, reaching lifetimes exceeding one second. These capabilities mark a crucial step toward using SrOH for precision measurement of time-variation in fundamental constants and symmetry-violating physics.

For the MOT section, this thesis focused on perspectives that have not been covered in previous theses, from introducing a method to calculate good initial laser frequencies for slowing to MOT capture velocities, to understanding the loading rate of the MOT in the presence of late-arriving molecules from the cryogenic buffer gas beam. We also discussed how we added two more repump lasers on top of the initial ten repumps, and the corresponding improvements. In the sub-Doppler cooling and ODT sections, we covered the latest results that are still under improvement.

For YbOH, we introduced and implemented a novel Zeeman-Sisyphus deceleration technique, successfully reducing the molecular beam velocity below 20 m/s with minimal photon scattering. These results establish the foundation for future MOT loading of heavier polyatomic species. In this thesis, we specifically covered perspectives not discussed in previous theses, such as details of the accidental resonances and how we debugged them. We also covered in detail how we implemented a depletion beam for removing relatively fast molecules contributing to background signal.

Together, these advances significantly broaden the toolbox for producing ultracold polyatomic molecules and open new directions in precision measurement and fundamental physics.

A

Construction of the SrOH Cryogenic Buffer Gas Beam Source

We describe the construction of the SrOH beam box, including radiation shields, charcoal sorb plates, gas fill lines, and the buffer gas cell. Most picture credits in this appendix go to Takashi Sakamoto.

A.1 Construction of the Blackbody Radiation Shields

To operate the cell at 2 K, we need to isolate the 2 K components from sources of heat, including blackbody radiation (BBR). A good round number for BBR at room temperature is approximately 50 mW/cm^2, which is significant for systems with only $\sim$W of cooling power at 2 K. Therefore, we construct BBR shields thermally anchored to the 40 K stage of the pulse tube, which provides approximately 40 W of cooling power. The BBR from the 40 K stage is much weaker than that from room temperature due to the Stefan–Boltzmann law.

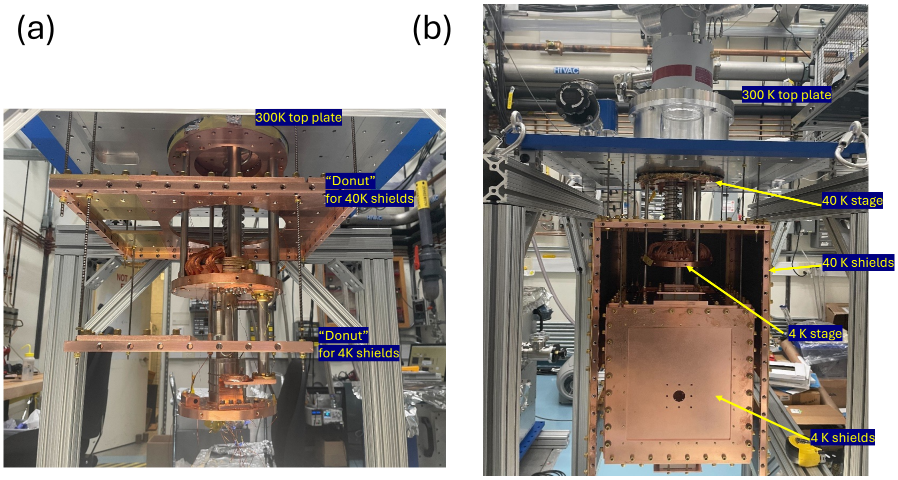

Figure A.1: (a) Construction of the top "donut" plates, where the side and bottom shields hang from. The top plates are removable from the "donut" frames. (b) Construction of the rest of the 40K and 4K shields.

In our construction, we hang the 40 K and 4 K shields from a donut frame, using bars with tapped holes between each panel to bolt them together. The shields are made of Copper 101 for good thermal conduction at cryogenic temperatures. Each cryogenic component was sanded up to 600-grit sandpaper (starting from lower grits), and then cleaned with Citranox, acetone, and isopropanol. The 40 K shields were gold-plated (shipped to CIL) to reduce the emissivity of their surfaces and thereby lower the heat load from room-temperature BBR. The inside gold plating was sanded off and instead blackened with swab-on copper blackener to increase emissivity. This ensures that BBR reflected from the 4 K shields is primarily absorbed by the 40 K shields, rather than bouncing between the 4 K and 40 K shields until eventually being absorbed on either side.

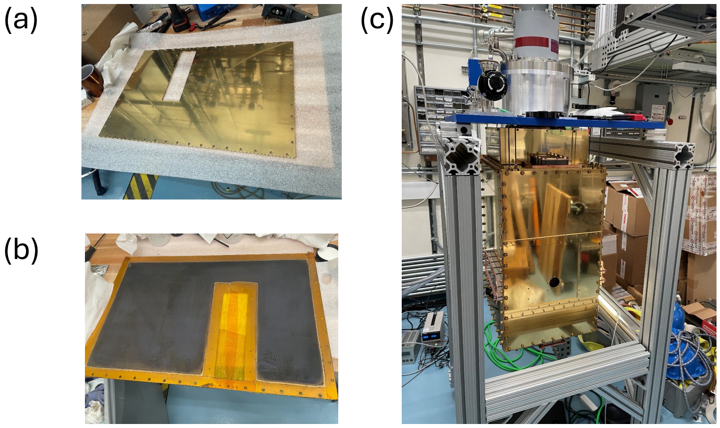

Figure A.2: Gold plating.

The 4 K and 40 K shields were assembled hanging from the top panel of the room-temperature ("300 K") vacuum dewar. We also mounted the pulse tube onto the 300 K top panel. The thermal links between the radiation shields and the 4 K and 40 K stages of the pulse tube were made using flexible Copper 101 braids. The entire assembly was then lifted into the rest of the 300 K vacuum dewar.

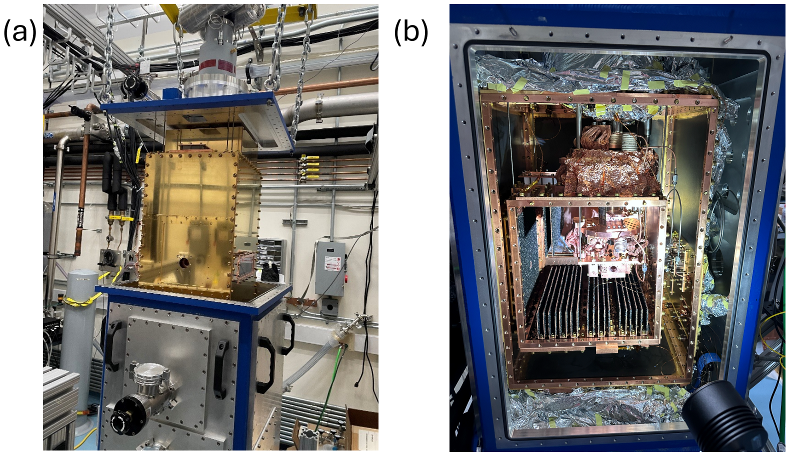

Figure A.3: (a) Lifting the radiation shields into the room temperature vacuum-sealed dewar. (b) Opening one side of the shields after assembly

A.2 MODIFICATIONS TO THE PULSE TUBE

In the new version of the Cryomech PT420 pulse tube, a passive thermal switch is installed between the 4 K and 2 K stages. This allows the 2 K stage to cool down together with the 4 K stage until it reaches approximately 10 K, at which point the switch thermally detaches, allowing the 2 K stage to cool independently. The switch works by sealing helium gas inside a hollow stainless steel cylinder (which has low thermal conductivity), along with charcoal placed on the 2 K side. The helium gas conducts heat when it fills the cylinder. As the 2 K stage cools and approaches $\sim$ 10 K, the helium is absorbed into the charcoal, stopping heat conduction.

However, Cryomech installed the heat switch upside down, resulting in it switching off too early. With the charcoal on the 4 K side, the thermal switch stopped conducting heat when the 4 K stage reached ~ 10 K. Since the 4 K stage cools faster than the 2 K stage, this caused the switch to deactivate before the 2 K stage had even reached ~ 50 K.

To resolve this, we machined custom mounts to flip the orientation of the thermal switch.

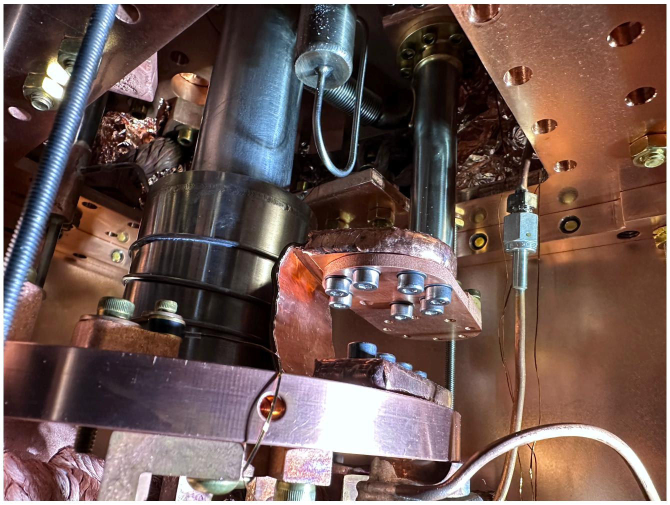

Figure A.4: Themal switch that needed to be flipped upside down because Cryomech installed it in the wrong direction.

We also covered holes on the pulse tube stages with copper foil in places where it was difficult to install solid copper shielding. In particular, on the 40 K stage, which sits inside the collar and is hard to access after assembly, we gold-plated the copper foil in-house and used it to cover the top side.

A.3 WINDOWS

We used BK-7 glass as the material for the windows because it is effective at blocking wavelengths prominent in the room-temperature BBR spectrum. We cut the glass to our desired sizes using a water jet, and then sanded the corners with low-grit sandpaper. When mounting the windows, we applied Kapton tape to the window mounts to avoid hard contact, leaving the corners tape-free so that the

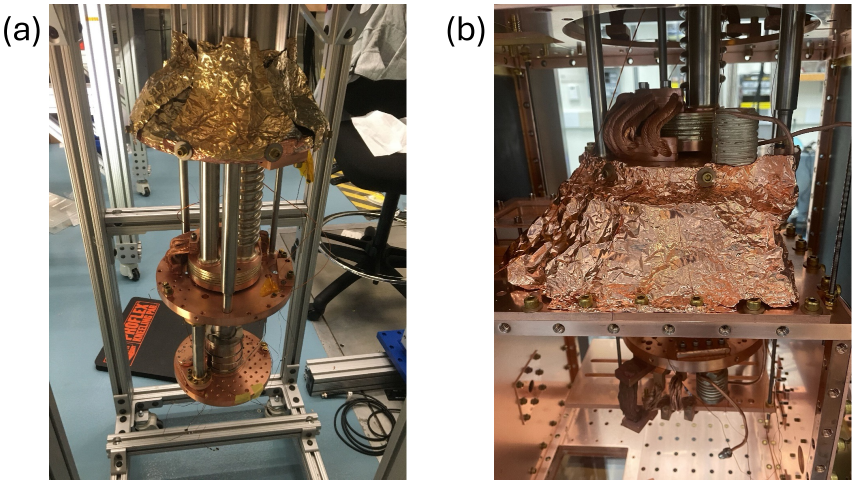

Figure A.5: (a) Gold-plated copper foil around the pulse tube that gets hidden in the collar after assembly. The gold plating was done in-house. (b) Copper foil around the copper braid thermal links on the 4 K shield to cover the gaps.

clamping force would be lower at the corners—where the glass is most likely to crack.

One thing to note is that BK-7 is a good absorber of room-temperature BBR, so it's important to minimize the window area to reduce thermal loads on the 40 K shields. We ended up covering some of the window area with superinsulation to reduce the heat load on the 40 K stage.

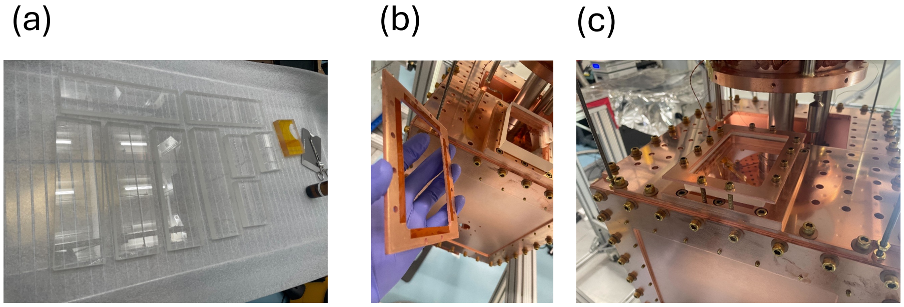

Figure A.6: (a) Glass windows cut on the water jet. (b) Kapton tape patterns avoiding the corners. (c) Window mounted with titanium screws.

A.4 SORBS

To pump out helium buffer gas effectively, we used charcoal sorbs in the 4 K section. We made charcoal sorb fins by Stycasting coconut charcoal (8–30 mesh) onto Copper 101 plates that had been roughened with 200-grit sandpaper (sanded to improve adhesion of the Stycast). The 8–30 mesh charcoal—meaning particles between 8 and 30 mesh in size—had enough variation in grain size to effectively cover the surface when sprinkled onto the Stycast-coated copper plates.

A.5 HEAT SINKING THERMOMETER WIRES

Another source of heat leaking into the 4 K and 2 K sections is conductive heat through the thermometer wires. To mitigate this, we heat-sunk the thermometer wires to the 40 K stage before they

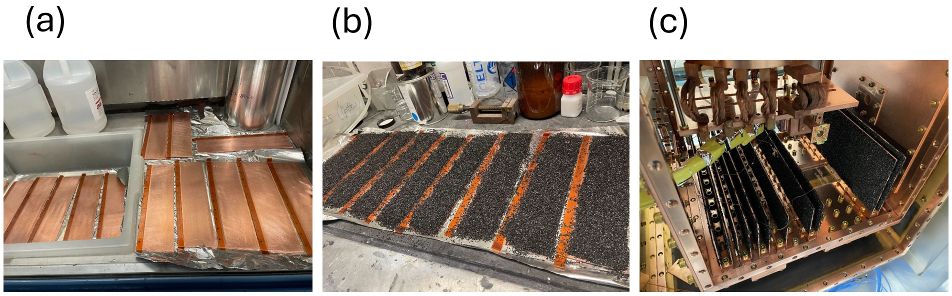

Figure A.7: (a) Copper 101 plates sanded with 200-grit sandpaper where the charcoal attaches. (b) Charcoal attached to the copper plates with Stycast. (c) Sorb plates mounted inside the 4 K shields.

were connected to the colder parts of the beam box. We used copper barrels approximately 0.5" in diameter and 1" in height. The thermometer wires were wrapped around each barrel about 10 times and secured with Stycast. The barrels were bolted onto the 40 K shields using 1/4-20 brass screws.

A.6 GAS FILL LINES AND GAS HANDLING

In the SrOH experiment, we use two types of gases in the beam box: helium for buffer-gas cooling, and water for producing SrOH molecules through chemical reactions.

For the helium gas, it must thermalize with the cell walls at 2 K. We heat-sink the helium fill line at the 40 K and 4K stages before it enters the cell. The heat sinking is done using copper barrels, around which the fill lines are wrapped and brazed, as shown in Fig.A.9. The Copper 101 tubes have an outer diameter (OD) of 1/8" and an inner diameter (ID) of 1/16". Each tube has VCR connectors brazed onto the ends to interface with other tubing.

On the other hand, water vapor needs to enter the buffer gas cell at around room temperature. Therefore, we use a heated fill line, where chip resistors are Stycasted approximately 1" apart onto a copper tube with an outer diameter (OD) of 1/16" and an inner diameter (ID) of 1/32", as shown in Fig. A.10. Note that in this case, the purity of the copper is less critical, since the line operates at room

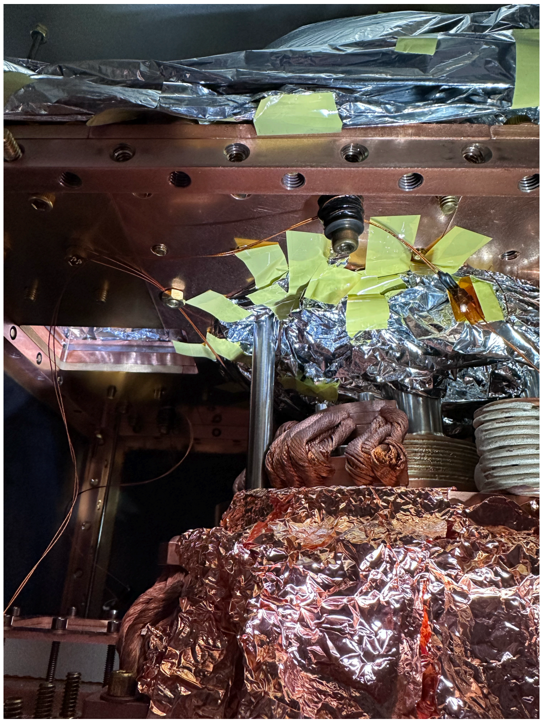

Figure A.8: Copper barrel used for heat sinking thermometer wires to the 40K shield. The wire is wrapped around and then covered with Stycast.

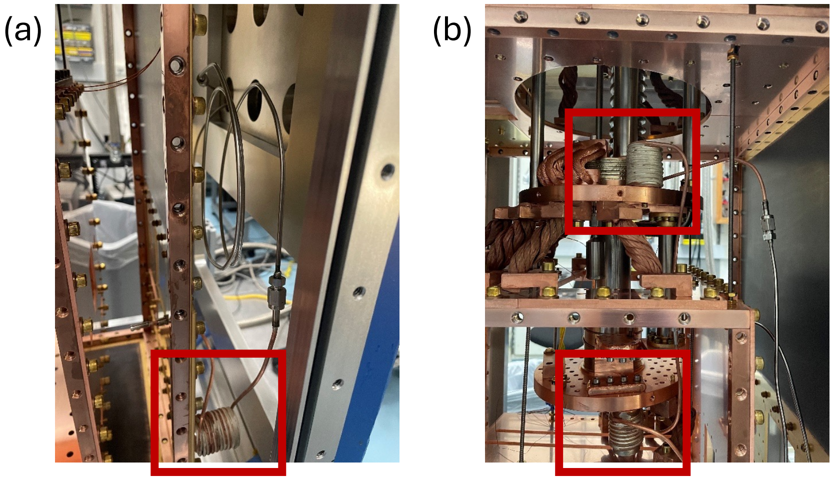

Figure A.9: Helium fill lines (a) in between room temperature and 40 K shields (b) inside 40 K shields. The heat sink "barrels" are highlighted with red boxes.

temperature. Finally, the tip of the fill line is connected to the cell's heated fill line segment (explained later) using a Teflon tube adapter. The Teflon ensures that the connection remains leak-tight at low temperatures.

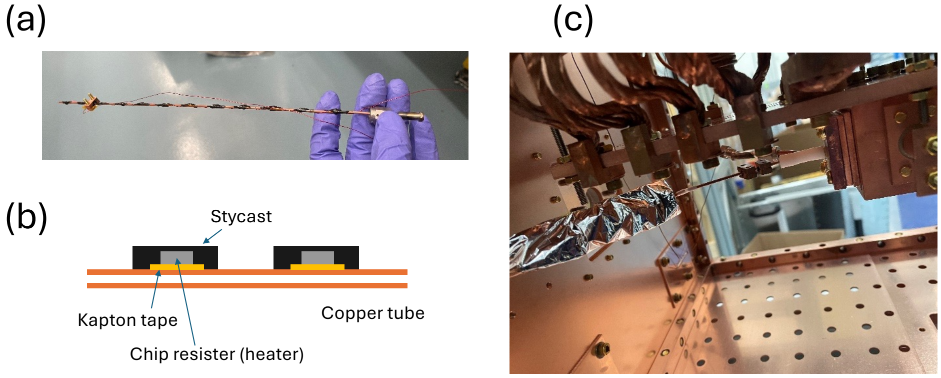

Figure A.10: (a) Picture of heated fill line. (b) Schematic drawing. (c) Heated fill line (covered in superinsulation) attached to the end piece on the cell.

The gas handling manifold was constructed as shown in Fig. A.11, using VCR connections. Each gas flows through an MKS flow controller with a metal seal (model GM50A013101RMM020). We typically flow approximately 4–5 sccm of helium and about 0.2 sccm of water during normal operation. We also have valves to bypass the flow controller and to pump out each manifold. The helium source is a regular compressed gas bottle, and the water source is vapor from distilled water contained in a CF nipple.

A.7 Cell construction

We designed and machined a cell as shown in Fig. A.12, from a block of Copper 101. The inner cell diameter is 1.7” with a front aperture of 7 mm. The second stage is 1” thick with an aperture of 9 mm. The helium fill line attaches to the back of the first-stage cell, and the water fill line attaches diagonally at 30 degrees, pointing toward the Sr metal target. We attach a separate heated fill line tip directly on

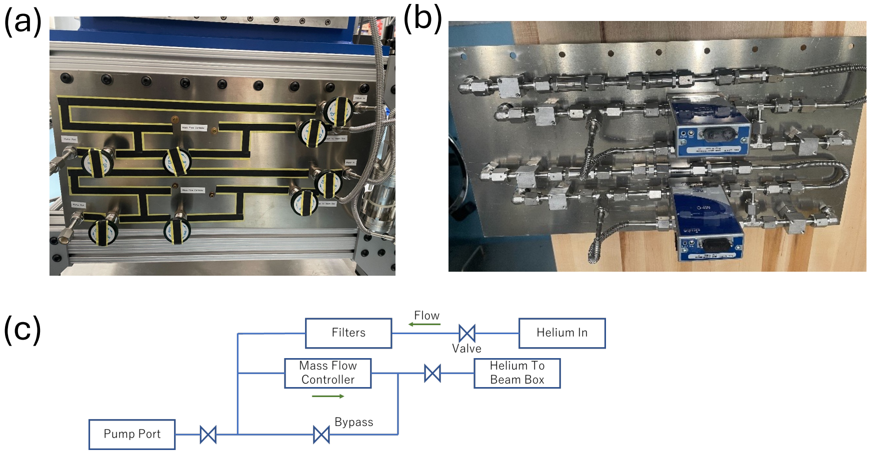

Figure A.11: (a) Front side of the gas-handling manifold. (b) Back side. (c) Schematic drawing (only the Helium manifold is shown).

the cell and connect it to the rest of the heated water fill line using a Teflon piece. The heated fill line extends into the cell, with the tip almost flush with the cell wall inside. The connection to the cell is made through thin Teflon tubing and an Ultem (yellow in the picture) grabber. To mechanically stabilize the heated fill line piece on the cell, we used a G-10 holder of 1/8" thickness, 0.5" width, and 3.25" length. Then, we used two stainless steel rods and small G-10 pieces to secure the other end of the heated fill line.

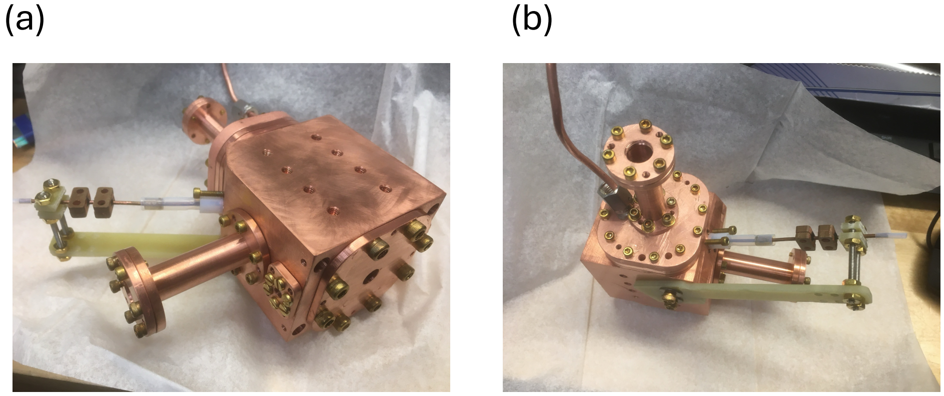

Figure A.12: Different views of the cell with the heated fill line end. (a) From the YAG window side. (b) From the rear window side.

References

[4] ACME Collaboration (2018). Improved limit on the electric dipole moment of the electron. *Nature*, 562, 355–360.

[5] Anderegg, L., Augenbraun, B. L., Chae, E., Hemmerling, B., Hutzler, N. R., Ravi, A., Collopy, A., Ye, J., Ketterle, W., & Doyle, J. M. (2017). Radio frequency magneto-optical trapping of caf with high density. *Physical Review Letters*, 119(10), 103201.

[6] Anderegg, L., Vilas, N. B., Hallas, C., Robichaud, P., Jadbabaie, A., Doyle, J. M., & Hutzler, N. R. (2023). Quantum control of trapped polyatomic molecules for eedm searches. *Science*, 382(6671), 665–668.

[7] Arvanitaki, A., Huang, J., & Tilburg, K. V. (2015). Searching for dilaton dark matter with atomic clocks. *Physical Review D*, 91(1), 015015.

[8] Balázs, C., Carena, M., Menon, A., Morrissey, D. E., & Wagner, C. E. M. (2005). Supersymmetric origin of matter. *Phys. Rev. D*, 71, 075002.

[9] Banerjee, A., Kim, H., & Perez, G. (2019). Coherent relaxion dark matter. *Physical Review D*, 100(11), 115026.

[10] Baron, J., Campbell, W. C., DeMille, D., Doyle, J. M., Gabrielse, G., Gurevich, Y. V., Hess, P. W., Hutzler, N. R., Kirilov, E., Kozyryev, I., O'Leary, B. R., Panda, C. D., Parsons, M. F., Petrik, E. S., Spaun, B., Vutha, A. C., & West, A. D. (2014). Order of magnitude smaller limit on the electric dipole moment of the electron. *Science*, 343(6168), 269–272.

[11] Barry, J. F., McCarron, D. J., Norrgard, E. B., Steinecker, M. H., & DeMille, D. (2014). Magneto-optical trapping of a diatomic molecule. *Nature*, 512, 286–289.

[12] Bernreuther, W. & Suzuki, M. (1991). The electric dipole moment of the electron. *Rev. Mod. Phys.*, 63, 313–340.

[13] Bian, L., Liu, T., & Shu, J. (2015). Cancellations between two-loop contributions to the electron electric dipole moment with a *cp*-violating higgs sector. *Phys. Rev. Lett.*, 115, 021801.

[14] Born, M. & Oppenheimer, J. R. (1927). Zur quantentheorie der molekeln. *Annalen der Physik*, 389(20), 457–484.

[15] Bransden, B. H. & Joachain, C. J. (2003). *Physics of Atoms and Molecules*. Pearson Education, 2nd edition.

[16] Brazier, C. R. & Bernath, P. F. (1985). Laser and fourier transform spectroscopy of the a$^2\pi$–x$^2\sigma^+$ transition of sroh. *Journal of Molecular Spectroscopy*, 114(1), 163–173.

[17] Brdar, V., Kopp, J., Liu, J., Prass, P., & Wang, X.-P. (2018). Fuzzy dark matter and nonstandard neutrino interactions. *Physical Review D*, 97(4), 043001.

[18] Brown, J. M. (2003). The rotational dependence of the renner–teller interaction: a new term in the effective hamiltonian for linear triatomic molecules in π electronic states. *Molecular Physics*, 101(21), 3419–3426.

[19] Brown, J. M., Hougen, J. T., Huber, K.-P., Johns, J. W. C., Kopp, I., Lefebvre-Brion, H., Merer, A. J., Ramsay, D. A., Rostas, J., & Zare, R. N. (1975). The labeling of parity doublet levels in linear molecules. *Journal of Molecular Spectroscopy*, 55(3), 500–503.

[20] Brzeminski, D., Chacko, Z., Dev, A., & Hook, A. (2021). Time-varying fine structure constant from naturally ultralight dark matter. *Physical Review D*, 104(7), 075019.

[21] Cairncross, W. B., Gresh, D. N., Grau, M., Cossel, K. C., Roussy, T. S., Ni, Y., Zhou, Y., Ye, J., & Cornell, E. A. (2017). Precision measurement of the electron's electric dipole moment using trapped molecular ions. *Phys. Rev. Lett.*, 119, 153001.

[22] Canetti, L., Drewes, M., & Shaposhnikov, M. (2012). Matter and antimatter in the universe. *New Journal of Physics*, 14(9), 095012.

[23] Collopy, A. L., Ding, S., Wu, Y., Finneran, I. A., Anderegg, L., Augenbraun, B. L., Doyle, J. M., & Ye, J. (2018). 3d magneto-optical trap of yttrium monoxide. *Physical Review Letters*, 121(21), 213201.

[24] Cosme, C., Rosa, J. G., & Bertolami, O. (2018). Scale-invariant scalar field dark matter through the higgs portal. *Journal of High Energy Physics*, 2018(5), 129.

[25] Denis, M., Haase, P. A. B., Timmermans, R. G. E., Eliav, E., Hutzler, N. R., & Borschevsky, A. (2019). Enhancement factor for the electric dipole moment of the electron in the baoh and yboh molecules. *Phys. Rev. A*, 99, 042512.

[26] Engel, J., Ramsey-Musolf, M. J., & van Kolck, U. (2013). Electric dipole moments of nucleons, nuclei, and atoms: The standard model and beyond. *Progress in Particle and Nuclear Physics*, 71, 21–74. Fundamental Symmetries in the Era of the LHC.

[27] Farrar, G. R. & Shaposhnikov, M. E. (1994). Baryon asymmetry of the universe in the standard model. *Phys. Rev. D*, 50, 774–818.

[28] Feng, J. L. (2013). Naturalness and the status of supersymmetry. *Annual Review of Nuclear and Particle Science*, 63, 351–382.

[29] Frenett, A., Lasner, Z., Cheng, L., & Doyle, J. M. (2024). Vibrational branching fractions for laser cooling of nonlinear strontium-containing molecules. *Phys. Rev. A*, 110(2), 022811.

[30] Gaul, K. & Berger, R. (2020). Ab initio study of parity and time-reversal violation in laser-coolable triatomic molecules. *Phys. Rev. A*, 101, 012508.

[31] Ginges, J. & Flambaum, V. (2004). Violations of fundamental symmetries in atoms and tests of unification theories of elementary particles. *Physics Reports*, 397(2), 63–154.

[32] Graham, P. W. & Rajendran, S. (2013). New observables for direct detection of axion dark matter. *Physical Review D*, 88(3), 035023.

[33] Hallas, C., Li, G. K., Vilas, N. B., Robichaud, P., Anderegg, L., & Doyle, J. M. (2024). High compression blue-detuned magneto-optical trap of polyatomic molecules. *arXiv preprint*.

[34] Hallas, C., Vilas, N. B., Anderegg, L., Robichaud, P., Winnicki, A., Zhang, C., Cheng, L., & Doyle, J. M. (2023). Optical trapping of a polyatomic molecule in an ℓ-type parity doublet state. *Physical Review Letters*, 130(15), 153202.

[35] Herzberg, G. (1950). *Molecular Spectra and Molecular Structure: Vol. I – Spectra of Diatomic Molecules*. Van Nostrand Reinhold, 2nd edition.

[36] Jadbabaie, A., Pilgram, N. H., Kłos, J., Kotochigova, S., & Hutzler, N. R. (2020). Enhanced molecular yield from a cryogenic buffer gas beam source via excited state chemistry. *New Journal of Physics*, 22(2), 022002.

[37] Kawasaki, A. (2024). Nuclear and particle physics through quantum sensing using cold atoms and molecules. *arXiv preprint arXiv:2411.19424*.

[38] Khriplovich, I. & Pospelov, M. (1994). Magnetic quadrupole moment of w-boson in kobayashi-maskawa model. *Nuclear Physics B*, 420(3), 505–514.

[39] Khriplovich, I. B. & Lamoreaux, S. K. (1997). *CP Violation Without Strangeness: Electric Dipole Moments of Particles, Atoms, and Molecules*. Theoretical and Mathematical Physics. Springer.

[40] Kozyryev, I. & Hutzler, N. R. (2017). Precision measurement of time-reversal symmetry violation with laser-cooled polyatomic molecules. *Phys. Rev. Lett.*, 119, 133002.

[41] Kozyryev, I., Lasner, Z., & Doyle, J. M. (2021). Enhanced sensitivity to ultralight bosonic dark matter in the spectra of the linear radical sroh. *Phys. Rev. A*, 103, 043313.

[42] Lasner, Z., Lunstad, A., Zhang, C., Cheng, L., & Doyle, J. M. (2022). Vibronic branching ratios for nearly closed rapid photon cycling of sroh. *Phys. Rev. A*, 106, L020801.

[43] Lasner, Z. D., Frenett, A., Sawaoka, H., Anderegg, L., Augenbraun, B., Lampson, H., Li, M., Lunstad, A., Mango, J., Nasir, A., Ono, T., Sakamoto, T., & Doyle, J. M. (2025). Magneto-optical trapping of a heavy polyatomic molecule for precision measurement. *Physical Review Letters*, 134, 083401.

[44] Li, G. K., Hallas, C., & Doyle, J. M. (2025). Conveyor-belt magneto-optical trapping of molecules. *New Journal of Physics*, 27(4), 043002.

[45] Li, Y., Profumo, S., & Ramsey-Musolf, M. (2009). Bino-driven electroweak baryogenesis with highly suppressed electric dipole moments. *Physics Letters B*, 673(1), 95–100.

[46] Ng, K. B., Zhou, Y., Cheng, L., Schlossberger, N., Park, S. Y., Roussy, T. S., Caldwell, L., Shagam, Y., Vigil, A. J., Cornell, E. A., & Ye, J. (2022). Spectroscopy on the electron-electric-dipole-moment–sensitive states of thf$^+$. *Physical Review A*, 105(2), 022823.

[47] Pospelov, M. & Ritz, A. (2005). Electric dipole moments as probes of new physics. *Annals of Physics*, 318(1), 119–169. Special Issue.

[48] Prasannaa, V. S., Shitara, N., Sakurai, A., Abe, M., & Das, B. P. (2019). Enhanced sensitivity of the electron electric dipole moment from yboh: The role of theory. *Phys. Rev. A*, 99, 062502.

[49] Quapp, W. & Winnewisser, B. P. (1993). What you thought you already knew about the bending motion of triatomic molecules. *Journal of Mathematical Chemistry*, 14, 259–285.

[50] Roussy, T. S., Caldwell, L., Wright, T., Cairncross, W. B., Shagam, Y., Ng, K. B., Schlossberger, N., Park, S. Y., Wang, A., Ye, J., & Cornell, E. A. (2023). An improved bound on the electron's electric dipole moment. *Science*, 381(6653), 46–50.

[51] Sawaoka, H., Frenett, A., Nasir, A., Ono, T., Augenbraun, B. L., Steimle, T. C., & Doyle, J. M. (2023). Zeeman-sisyphus deceleration for heavy molecules with perturbed excited-state structure. *Physical Review A*, 107, 022810.

[52] Shaposhnikov, M. (1987). Baryon asymmetry of the universe in standard electroweak theory. *Nuclear Physics B*, 287, 757–775.

[53] Stadnik, Y. V. & Flambaum, V. V. (2015). Can dark matter induce cosmological evolution of the fundamental constants of nature? *Physical Review Letters*, 115(20), 201301.

[54] Stadnik, Y. V. & Flambaum, V. V. (2016). Improved limits on interactions of low-mass spin-0 dark matter from atomic clock spectroscopy. *Physical Review A*, 94(2), 022111.

[55] Stuhl, B. K., Sawyer, B. C., Wang, D., & Ye, J. (2008). Magneto-optical trap for polar molecules. *Phys. Rev. Lett.*, 101, 243002.

[56] Vilas, N. B., Hallas, C., Anderegg, L., Robichaud, P., Winnicki, A., Mitra, D., & Doyle, J. M. (2022). Magneto-optical trapping and sub-doppler cooling of a polyatomic molecule. *Nature*, 606, 70–74.

[57] Vilas, N. B., Hallas, C., Anderegg, L., Robichaud, P., Zhang, C., Dawley, S., Cheng, L., & Doyle, J. M. (2023). Blackbody thermalization and vibrational lifetimes of trapped polyatomic molecules. *Phys. Rev. A*, 107, 062802.

[58] Vutha, A. C., Campbell, W. C., Gurevich, Y. V., Hutzler, N. R., Parsons, M., Patterson, D., Petrik, E., Spaun, B., Doyle, J. M., Gabrielse, G., & DeMille, D. (2010). Search for the electric dipole moment of the electron with thorium monoxide. *Journal of Physics B: Atomic, Molecular and Optical Physics*, 43(7), 074007.

[59] Williams, H. J., Truppe, S., Hambach, M., Caldwell, L., Fitch, N. J., Hinds, E. A., Sauer, B. E., & Tarbutt, M. R. (2017). Molecules cooled below the doppler limit. *New Journal of Physics*, 19(11), 113035.

[60] Yu, S. S., You, J., Bao, Y., Anderegg, L., Hallas, C., Li, G. K., Lim, D., Chae, E., Ketterle, W., Ni, K.-K., & Doyle, J. M. (2024). A conveyor-belt magneto-optical trap of caf. *arXiv preprint*.

[61] Zeng, Z., Deng, S., Yang, S., & Yan, B. (2024). Three-dimensional magneto-optical trapping of barium monofluoride. *Phys. Rev. Lett.*, 133, 143404.

[62] Zhang, C., Yu, P., Conn, C. J., Hutzler, N. R., & Cheng, L. (2023). Relativistic coupled-cluster calculations of raoh pertinent to laser cooling and fundamental physics. *Phys. Chem. Chem. Phys.*, 25, 32613–32621.